

CHEMICAL AND ELECTRICAL PROPERTIES OF GRAIN
BOUNDARIES IN POLYCRYSTALLINE SILICON

BY
PHILLIP EUGENE RUSSELL

A DISSERTATION PRESENTED TO THE GRADUATE COUNCIL OF
THE UNIVERSITY OF FLORIDA
IN PARTIAL FULFILLMENT OF THE REQUIREMENTS FOR THE
DEGREE OF DOCTOR OF PHILOSOPHY

UNIVERSITY OF FLORIDA

1982

UNIVERSITY OF FLORIDA



3 1262 08552 4865

TO MY DAUGHTER, SAYWARD ELIZABETH, WHOSE BIRTH
MOTIVATED THE COMPLETION OF THIS WORK

ACKNOWLEDGEMENTS

The author sincerely thanks the chairman of his supervisory committee, Dr. Paul Holloway, for his help and guidance during the course of the research presented in this dissertation. The author also thanks the other members of his supervisory committee, Dr. John J. Hren, Dr. Rolf Hummel and Dr. Fredrik A. Lindholm for the friendly assistance; as well as faculty members Dr. Stan Bates and Dr. Dortha Burk for technical assistance.

Appreciation is extended to the author's colleagues and friends for stimulating discussions and technical assistance: Dr. L.L. Kazmerski, P.J. Ireland, Rik Matson, Charles Herrington, Kim Jones and Jeffrey A. Mazer. Appreciation is also extended to Pat Newman for assistance in preparing this dissertation.

The author gratefully acknowledges the financial support and technical assistance of the U.S. Department of Energy and the Solar Energy Research Institute during the course of this research.

Last, but not least, the author thanks his wife and parents for their frequent support and encouragement throughout his graduate school career.

TABLE OF CONTENTS

		PAGE
	ACKNOWLEDGEMENTS.....	iii
	ABSTRACT.....	vi
CHAPTER		.
ONE	INTRODUCTION.....	1
TWO	REVIEW OF GRAIN BOUNDARY PROPERTIES IN POLYSILICON.....	3
	Introduction.....	3
	Applications.....	4
	Electrical Properties and Models.....	7
	Electrical Properties-Case of a Solar Cell.....	13
THREE	THE ELECTRON BEAM INDUCED CURRENT TECHNIQUE AND THEORY.....	15
FOUR	EXPERIMENTAL DETAILS.....	34
	Material.....	34
	Electron Beam Induced Current.....	35
	Transmission Electron Microscopy.....	38
	Ion Microscopy and Secondary Ion Mass Spectroscopy...	38
	Auger Electron Spectroscopy.....	42
FIVE	DEVELOPMENT OF AUTOMATED EBIC SYSTEM.....	43
	Introduction.....	43
	Procedure Required for Manual Measurements.....	44
	Advantages of Automation.....	49
	Specifics of the System.....	50
	Software.....	53
	Extention of EBIC on MBX.....	60
	Modifications of EBIC for JEOL JSM 35C SEM.....	64
	Advantagas of an EPMA Over an SEM for EBIC.....	64
	Applications.....	66
SIX	EXPERIMENTAL IMPORTANCE OF EBIC PARAMETERS.....	68
	Introduction.....	68
	Reproducibility.....	69
	Useful Range of Beam Current and Voltage.....	71
	Discussion.....	79

	PAGE
SEVEN	GRAIN STRUCTURE AND GRAIN BOUNDARY EFFECTS.....82
	Introduction.....82
	Grain Structure.....82
	Uniformity of Grain Boundary Response.....93
	P-N Junction Structure at Grain Boundaries.....95
	Discussion.....102
EIGHT	THE EFFECT OF HEAT TREATMENT ON GRAIN BOUNDARY PROPERTIES IN CAST POLYCRYSTALLINE SILICON.....105
	Introduction.....105
	Experimental.....107
	Results.....110
	Physical Measurements.....125
	Discussion.....131
	Conclusions.....136
NINE	DISCUSSION AND CONCLUSIONS.....138
	Discussion.....138
	Conclusions.....144
	REFERENCES.....146
APPENDIX	
I	TERMS AND DEFINITIONS USED IN EBIC SOFTWARE SYSTEM.....153
II	EBIC COMMANDS.....156
III	FUNCTIONS OF PROGRAM BLOCKS (EBIC).....172
IV	MIS DEVICE FABRICATION DETAILS.....178
V	STANDARD WAFER CLEANING AND POLISHING PROCEDURES....179
	BIOGRAPHICAL SKETCH.....180

Abstract of Dissertaion Presented to the Graduate Council
of the University of Florida in Partial Fulfillment of
the Requirements for the Degree of Doctor of Philosophy

CHEMICAL AND ELECTRICAL PROPERTIES OF
GRAIN BOUNDARIES IN POLYCRYSTALLINE SILICON

By

Phillip Eugene Russell

December 1982

Chairman: Dr. Paul Holloway
Major Department: Materials Science and Engineering

Experimental techniques for the investigation of the electrical and chemical properties of grain boundaries are developed and utilized for the study of cast polycrystalline silicon. Totally automated electron beam induced current (EBIC) techniques are developed, including hardware and software development, and are used for the study of recombination properties of silicon grain boundaries. Automation was used to maximize the precision and accuracy of the EBIC data and to allow large numbers of measurements to be performed to determine the effects of experimental parameters on reproducibility and beam damage. EBIC, secondary electron and optical microscopy techniques are used to characterize the grain size and structure in Wacker Silso cast polycrystalline silicon. The grain size is found to be 1.63 ± 0.43 millimeters. Grain structure was found to be controlled by the casting process used to form the material. Twin boundaries are found to be electrically inactive. Preferential grain boundary diffusion of phosphorus in silicon grain boundaries is measured using both bevel and stain, and bevel/EBIC techniques. The effects of heat treatments at 600, 750 and 900°C are investigated extensively. An MIS device structure which does not

require high temperature processing ($>200^{\circ}\text{C}$) for fabrication is developed and utilized for these studies. EBIC analysis results show that grain boundary recombination velocity is substantially increased by heating cast polysilicon to temperatures as low as 600°C , whereas no effects were seen at 400°C . Heat treatments up to 900°C are investigated. Use of complementary surface analysis techniques are developed which show that these heat treatments result in oxygen segregation to grain boundaries. In-situ fracturing techniques for Auger electron spectroscopy and secondary ion mass spectroscopy analysis of grain boundaries are developed. Ion microscopy techniques are developed and used to complement the fracture studies. Local oxygen concentrations of 0.1 atomic % were measured. Based on the time and temperature dependence of the activation of grain boundary recombination, it is concluded that oxygen segregation is responsible for the activation.

CHAPTER ONE

INTRODUCTION

In this dissertation studies of grain boundary properties in cast polycrystalline silicon are presented. The basis of the studies was the desire to understand how grain boundaries affect the properties of solar cells fabricated on polycrystalline silicon. While it was desired to understand grain boundary properties in as general a sense as possible, only cast, large grain polysilicon was studied in this work. This was largely due to the availability of the material and the wide range of studies conducted by other researchers on similar material.

In Chapter Two, a review of grain boundary properties in polycrystalline silicon is given. Here the motivations for using polycrystalline silicon (as opposed to single crystal) are reviewed and explained, as are the types of polycrystalline silicon currently available. Then, existing experimental data on polysilicon grain boundaries and the various theoretical models of a silicon grain boundary are reviewed.

A major portion of this work has dealt with the development and application of electron beam induced current (EBIC) techniques for the study of silicon grain boundaries. Thus, a complete review of the EBIC technique is given in Chapter Three. Included in Chapter Three are reviews of theories developed to derive quantitative information about device or materials properties from the EBIC technique; and a brief history of the technique, theory and applications. Chapter Four

describes the experimental details including a description of the polycrystalline silicon used for all studies reported and a description of the major analytical equipment utilized.

To effectively utilize the EBIC technique for the study of silicon grain boundaries, a totally automated EBIC system was developed. The details of this system are described in Chapter Five. Here the motivation and need for such a system are described with respect to the present work. Then details of both the hardware and software developed for automating EBIC techniques are described. Studies into the experimental importance of EBIC parameters, for which the automated EBIC system was developed, are described in Chapter Six.

Chapter Seven describes studies, using EBIC and other microscopy techniques, of the grain size and grain structure of cast polycrystalline silicon. Also included are studies of the effects of grain boundaries on diffused p-n junction structures, including grain boundary diffusion effects.

The major experimental portions of this work are described in Chapter Eight. Here a study of the effects of heat treatment, to temperatures appropriate for solar cell fabrication, on grain boundary properties in polycrystalline silicon is described. Electrical effects are studied with the EBIC techniques described in Chapters Three, Six and Seven. A special low temperature device structure was designed and utilized in these studies. Complementary studies of changes in grain boundary chemistry due to heat treatment are described in detail. The relationship of the chemical and electrical effects observed are discussed.

CHAPTER TWO

REVIEW OF GRAIN BOUNDARY PROPERTIES IN POLYSILICON

Introduction

Silicon is the most widely used, and hence the most widely studied and understood, electronic material. Single crystal, ultra high purity forms of silicon are the more desired for fabrication of electronic devices due to well controlled and extremely homogeneous properties. There are several major limitations to the universal use of single crystal, ultra high purity (i.e., electronic grade) silicon. Purification processes and crystal growth are very costly and energy intensive. Also, single crystal boules of silicon must go through costly sawing and polishing procedures before actual use in electronic device fabrication. The electrical resistivity of single crystal silicon is controlled by dopants and very high values of resistivity are not readily obtained.

Many of the above mentioned problems can be avoided with the use of polycrystalline silicon. The elimination of single crystal growth techniques represent an obvious cost savings. Similarly elimination of final stages of purification also reduces costs. Thin or thick films of polycrystalline silicon can potentially be produced by relatively inexpensive processes such as chemical vapor deposition (CVD) or vacuum evaporation. Since the active volume of a typical device using silicon wafer technology represents only a small fraction of the total silicon in the wafer, a thin or thick film deposition process can potentially significantly reduce the amount of high purity silicon required for device fabrication. Also, the ability to grow layers, after processing

of base layers, adds the possibility of a third dimension for very large scale integrated circuit (VLSI) fabrication. Silicon becomes more versatile in polycrystalline form because the electrical resistivity is strongly influenced by the presence of grain boundaries, as will be discussed below. This allows the use of silicon in a semi-insulating form.

Applications

One of the major areas where polycrystalline silicon shows potential advantages over single crystal silicon is in large scale photovoltaic systems for terrestrial applications. In order for solar cells (i.e., photovoltaics) to become an important energy source on a national or international scale, many square miles of devices will be required. Silicon is an excellent candidate material for such an application for many reasons, the more important of which are abundance of the raw material and an extensive bank of knowledge on the properties of silicon and on the purifying and processing of silicon into active electronic devices. These advantages in many ways outweigh the disadvantages of non-optimum band gap and low optical absorption coefficient in the solar spectral range.^{1,2} For photovoltaic applications, the preference for polycrystalline over single crystal silicon is simply a matter of economics. Solar cells fabricated on single crystal silicon currently have higher collection efficiencies³ than that achieved or predicted for polycrystalline cells.⁴ However, single crystal cells are not cost competitive as an alternate energy source and current trends do not indicate that they ever will be.⁵ Cells fabricated on some form of lower cost polycrystalline silicon, however, do show promise of cost

competitiveness.⁶ Stages of purification can be eliminated or reduced without serious loss of device performance. The presence of grain boundaries significantly reduces the collection efficiency of current device structures. However, it is hoped that through the detailed understanding of the properties of grain boundaries and the mechanisms by which they limit present device performance, the deteriorating effects of grain boundaries can be eliminated or substantially reduced. Also, there is no fundamental reason that grain boundaries cannot be utilized in some way to enhance solar cell device performance to equal or even exceed that of single crystal cells.⁷ Growth techniques designed specifically for the production of sheet or film polycrystalline silicon for solar cell fabrication will be discussed below. A review of the basic properties of silicon grain boundaries will now be given, with emphasis on those properties which potentially affect the electrical performance of polysilicon solar cell devices.

Polysilicon can be prepared by any of a wide variety of techniques.³ The method of preparation strongly influences the grain size, type and distribution of grain boundaries and the chemical and electrical properties of grain boundaries.^{3,9} Methods of polysilicon preparation include directional solidification such as Czochralski pulling and casting, ribbon growth, chemical and physical vapor deposition (CVD and PVD) on a substrate and others such as electrodeposition and recrystallization techniques. Details of the various preparation techniques can be found in the literature.^{9,10}

In techniques such as CVD or PVD the substrate often determines the resulting grain size of polysilicon. Typical grain sizes are of the order of ten microns or smaller for these techniques. Grain sizes as large as several millimeters or even centimeters have been achieved by crystal pulling, ribbon and casting techniques.^{9,10} The grain structure, as well as the grain size, plays a dominant role in determining the electrical properties of polysilicon. Grain boundaries which lie perpendicular to the direction of current flow act as potential barriers for majority carriers.¹¹ Grain boundaries parallel to the direction of current flow do not tend to inhibit current flow, but can act as a short between the emitter and the base in the case of a diode or solar cell.¹¹ In the case of polysilicon fabricated into a solar cell, a grain structure with all grain boundary planes perpendicular to the device junction is commonly called columnar grain structure. This grain structure is the most commonly used model in theoretical treatments of the electrical properties of polycrystalline silicon solar cells.

The electrical properties of a grain boundary are related to the exact chemical and physical nature of the grain boundary.¹² It is of course the crystallography of two differently oriented grains joining at a two dimensional interface that gives rise to the notion of a grain boundary. A grain boundary is thus a special case of the more general description of crystalline interfaces. The discontinuity of the crystal lattice at a grain boundary invalidates the general solid state theory of solids which depends strongly on the periodicity of the crystal lattice. The discontinuity of the crystal lattice is known to affect parameters such as lattice strain, local atomic bonding, segregation

coefficients and diffusion coefficients.¹³⁻¹⁶ Although the actual extent of the crystallographic nature of a grain boundary as observed by transmission electron microscopy (TEM) is only a few tens of angstroms, the extent of electrical influence can be of the order of microns.¹⁷⁻²¹ Due to the crystallographic discontinuity of a grain boundary, local chemistry at a grain boundary can differ drastically from bulk chemistry nearby.^{13,14} The chemical differences, then, can have large effects on electrical properties.^{12,21-23} Thus both structure and/or chemistry of grain boundaries can influence electrical properties of grain boundaries. Clearly, however, grain boundary chemistry is a result of grain boundary structure and thus grain boundary structure, or crystallography, is the fundamental determining factor of grain boundary properties. The actual structure, chemistry and electrical properties of a grain boundary are the result of a complex set of interactions which include the effects of thermodynamics of the growth process and interactions of impurities, dopants, and substrate or container materials.

Electrical Properties and Models

Some of the terms used to describe the electrical activity of grain boundaries will now be defined. The use of some terms inherently infers the use of a particular model or theory to describe grain boundaries. For example, most analysis and modeling techniques treating the electrical transport properties of polycrystalline materials are based on the consideration that a space charge region due to the interface itself is inherent at grain boundaries.²⁴ This is based on an assumed analogy of a grain boundary and a surface. This space charge region may result in

the formation of a potential barrier to charge transport. Such a model was developed in 1956 by Petritz²⁵ to describe the conductivity of polycrystalline films with potential barriers between grains. The resulting energy band diagram is shown in Fig. 2.1.

The band diagram of Fig. 2.1 is inherently based on the assumption of accumulation or depletion of charge carriers at the grain boundary. In this work, we are considering only grain boundaries in elemental semiconductors, more specifically silicon. Whereas for compound semiconductors, grain boundary effects can be related to compositional or stoichiometric effects, in elemental semiconductors it is the incorporation of impurity atoms that controls electrical characteristics. Two basic models²⁶⁻³⁰ have been developed and used to interpret the observed electrical properties of elemental polycrystalline materials. In the segregation model, impurity atoms are assumed to segregate to grain boundaries where they become electrically inactive.^{26,27} This model has failed to represent the observed temperature dependence of the resistivity, and in fact, predicts a negative temperature coefficient of resistance which has not been observed experimentally.

The grain boundary trapping model²⁸⁻³⁰ is based on the existence of a large concentration of active trapping sites at the grain boundary which serve to capture free carriers. The charge states created at the grain boundaries in turn give rise to the type of grain boundary potential barrier illustrated in Fig. 2.1. Such grain boundary barriers are formed, in general, when a lower electrochemical potential for minority carriers exists in the boundary region than in the grains. This provides for the inflow of minority carriers to the region which

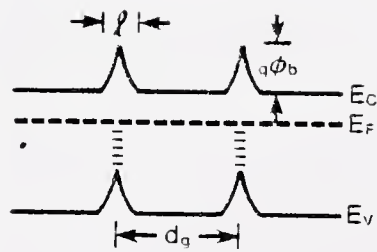


Figure 2.1 Energy band diagram representation of an n-type polycrystalline semiconductor with grain size d_g , grain boundary width l and grain boundary potential barrier height $q\phi_b$.

creates a space charge layer that inhibits further flow of carriers. In the case of silicon, barriers are formed in both n-type and p-type material, thus indicating that the Fermi level is located somewhere near the center of the band gap.^{27,28} In the case of germanium, however, grain boundary potential barriers are observed only in n-type material, thus indicating that the Fermi level is not near midgap.³¹⁻³³

The comprehensive development of a grain boundary trapping model, such as that of Seto,³⁰ introduces several more terms used to describe properties of polycrystalline materials and grain boundaries. The grain size is recognized as an important parameter, and is usually reduced to a two-dimensional idea as the average distance between grain boundaries, d_g , as illustrated in Fig. 2.1. The need for more accurate descriptions of grain size, such as ASTM grain size, has not developed and thus the very simple idea of average distance between grain boundaries is most commonly used in describing polycrystalline silicon.

The grain boundary width, ℓ in Fig. 2.1, remains a somewhat ambiguous term. In terms of Fig. 2.1, ℓ is often defined as the width at which the conduction and valence bands return to their mid-grain values. This should more properly be called an effective grain boundary width ℓ_{eff} , since the actual grain boundary may be narrower than this, but the electrical effects of the grain boundary extend to this effective width. The physical width of a grain boundary can be defined in terms of the actual width of the region of crystallographic change from one grain to another. This width is thought to be only a few atomic distances.^{17-20,34} Another effective grain boundary width often used is related to the minority carrier diffusion length, L , in the bulk and the

fact that free carriers within a few diffusion lengths of the grain boundary can be affected by its presence. One must therefore be very careful with the use of the term grain boundary width and carefully define the exact meaning for a particular case.

Of course bulk properties or intragrain properties have an important bearing on the overall properties of polycrystalline materials. Mentioned above is the minority carrier diffusion length L , which is defined as the average distance a free charge carrier can diffuse in one lifetime period in a semi-infinite material and given mathematically by $L = \sqrt{D\tau}$. Here D is the diffusion coefficient of the minority carriers in the material and τ is lifetime of the carriers. The density of acceptors in the bulk is given by N_a and similarly N_d is the donor density.

In describing the actual charge carrier trapping at grain boundaries, terminology related to semiconductor surfaces is heavily drawn upon. The number of grain boundary traps N_t ($\frac{eV}{cm^2}$) are often described by the trap density Q_t (cm^{-2}). The energy of the traps is given as E_t , measured with respect to the intrinsic Fermi level energy, E_i . In the Seto model,³⁵ the grain boundary traps are assumed to be of fixed energy. However, the analogy with silicon surface states³⁶ suggests that the grain boundary trapping states may be distributed over some energy range. The trap states may also be filled or unfilled. Seager and Castner³⁷ have found that an exponential density of states model best describes the experimental data on polycrystalline silicon. Their results indicate that the largest grain boundary state densities consist of about $6 \times 10^{11}/cm^2$ available electron states located within 0.2 eV of

midgap. The work of Seager and Castner also demonstrates the effects of doping concentration on the grain boundary barrier height, $q\phi_b$. Three regions of properties exist: (1) $N_d < 10^{14}/\text{cm}^3$ where the majority of the grain boundary barriers are at $q\phi_b = 0.55$ eV (i.e., near midgap) and the resistivity is dominated by this activation energy; (2) $10^{14} < N_d < 2 \times 10^{15}/\text{cm}^3$ where a substantial number of barrier heights are less than 0.55 eV, but the resistivity versus temperature behavior is still dominated by the 0.55 eV $q\phi_b$; and (3) $N_d > 2 \times 10^{15}/\text{cm}^3$ where a range of barrier heights exists and the magnitude of the resistivity activation energy varies widely.

A double-depletion-layer thermal emission model has been developed and shown to be effective by Seager and co-workers.³⁷⁻⁴² A major point made from their work is that the barrier height is temperature dependent. The work also showed the importance of changing the interface state density by diffusion of atomic hydrogen down grain boundaries; thus initiating the work of grain boundary passivation by hydrogen.^{13,23,38} Current versus voltage (I-V) measurements across individual grain boundaries indicate that the boundary response can be divided into three voltage-dependent regions: ohmic, saturation and varistor. The ohmic region, essentially a straight-line dependence of I upon V, is observed for $V < 0.3$ volts. The saturation region is evident until the current rises steeply with increasing voltage, indicating the onset of the varistor region.

Electrical Properties - Case of a Solar Cell

In the case of a solar cell, several additional terms are needed to describe the electrical properties of a polycrystalline device or a grain boundary in such a device. A solar cell is based on the existence of the photovoltaic effect, in which light-generated electrons and holes are separated by an internal field created by some inhomogeneity in the device. This inhomogeneity can be due to a metal-semiconductor contact (Schottky barrier), a metal-insulator-semiconductor (MIS) structure, or a junction between two regions of a semiconductor having different types of conductivity, i.e., a p-n junction. The p-n junction can be either a homojunction in which the same semiconductor exists on both sides of the junction, or a heterojunction composed of two different semiconductors. In the case of polycrystalline silicon, junctions of all types are applicable. In this work, homojunctions of a n^+p structure (n^+ represents a heavily doped n-type layer) and MIS structures of aluminum SiO_x - silicon are the primary structures utilized.

The process of carrier generation for all forms of ionizing radiation is analogous, and hence the use of electron beams for carrier generation is utilized extensively in this work. When a form of ionizing radiation falls on a material, electrons and holes are generated as the radiation is absorbed. The minimum energy required to create an electron-hole pair is the band gap energy, E_g , which is 1.17 eV for silicon. In the process of carrier generation, an electron is excited from the valence band to the conduction band, leaving behind a hole in the valence band. After generation, the electrons and holes would simply recombine in the absence of a junction which serves to separate

them and allows the minority carriers to reach a region where they are in the majority. They then can be collected in an external circuit and hence create an induced current.

The number of majority carriers which reach the junction is influenced by the material properties of the semiconductor. The number reaching the junction is directly proportional to the diffusion length of minority carriers in the appropriate region of the device. As defined earlier, the diffusion length increases as the square root of the product of the diffusion coefficient and the lifetime. The diffusion coefficient increases with the carrier mobility, μ , which is a basic material parameter. The lifetime is dependent on the density of recombination sites and on their cross-section for carrier capture. In a real device, surfaces or interfaces exist which act as a plane of recombination sites. These surfaces are described in terms of a surface recombination velocity S , so-named because of its units (cm/sec). The term originated as a boundary condition at a surface for current continuity equations. When considering a grain boundary as an analog to a surface, the term grain boundary effective surface recombination velocity ($S_{\text{eff}}^{\text{gb}}$) is used.

CHAPTER THREE

THE ELECTRON BEAM INDUCED CURRENT TECHNIQUE AND THEORY

The modern scanning electron microscope (SEM) provides a readily available means of obtaining an electron beam, with control of beam voltage and beam current, finely focused onto a sample surface. The beam can be in a point, line scan or continuous raster mode. A conventional SEM image is obtained by collecting the secondary electrons emitted from the sample and displaying their intensity as a function of primary electron beam position.⁴³ Other signals are produced from the sample such as backscattered electrons, x-rays, Auger electrons, cathodoluminescence, and absorbed current which can also be used for imaging. If the sample is non-metallic and thus capable of supporting an internal electric field, the impinging electron beam will create electron-hole pairs which can move in response to an electric field. The electron-hole pairs, or mobile charge carriers, are produced by collisions of the primary electrons (of high energy) with valence electrons in the material. In the absence of an electric field, the carriers will diffuse randomly and recombine with one another until all excess carriers are eliminated. Although the minimum energy required to produce an electron-hole pair is that of the band gap, most carriers are produced with excess energy. This energy is dissipated as heat. Klein⁴⁴ has shown that roughly one-third of the energy of the incident electron beam produces electron-hole pairs and the remaining two-thirds is dissipated as heat. In silicon the average energy required to create an electron-hole pair is thus about three times the band-gap of 1.1 eV or 3.3 eV.

If an electric field is present within the semiconductor sample, directed motion of the mobile carriers will result. Separation of charge carriers in a semiconductor will create a measurable current if an appropriate external circuit is provided. This type of phenomena was called the barrier electron voltage effect by early researchers⁴⁵ and is very analogous to the familiar barrier photovoltaic effect. An electric field suitable for producing a measurable electric current as a result of electron beam bombardment can be supplied by any of the usual methods of forming a solar cell or photovoltaic device. Most commonly a p-n junction within the sample or some form of induced junction provides the electric field. When an electron beam is used to produce the measurable current, that current is referred to as electron beam induced current or EBIC.

Obtaining an EBIC signal in a conventional SEM requires minor hardware modifications. In the following, let us consider our sample to be a planar diffused p-n junction diode or solar cell with metal ohmic contacts available on both the emitter and base regions. In order to obtain a measurable current, the sample must be placed on an electrically isolated stage and contacts to the emitter and base must be separately available. These contacts are connected via lead wires through an ammeter which completes the circuit. The ammeter can be used to produce an analog voltage output, proportional to the EBIC signal, which is compatible with the video input signal of the SEM and thus an EBIC image can be produced. A schematic drawing of such a system is shown in Fig. 3.1.

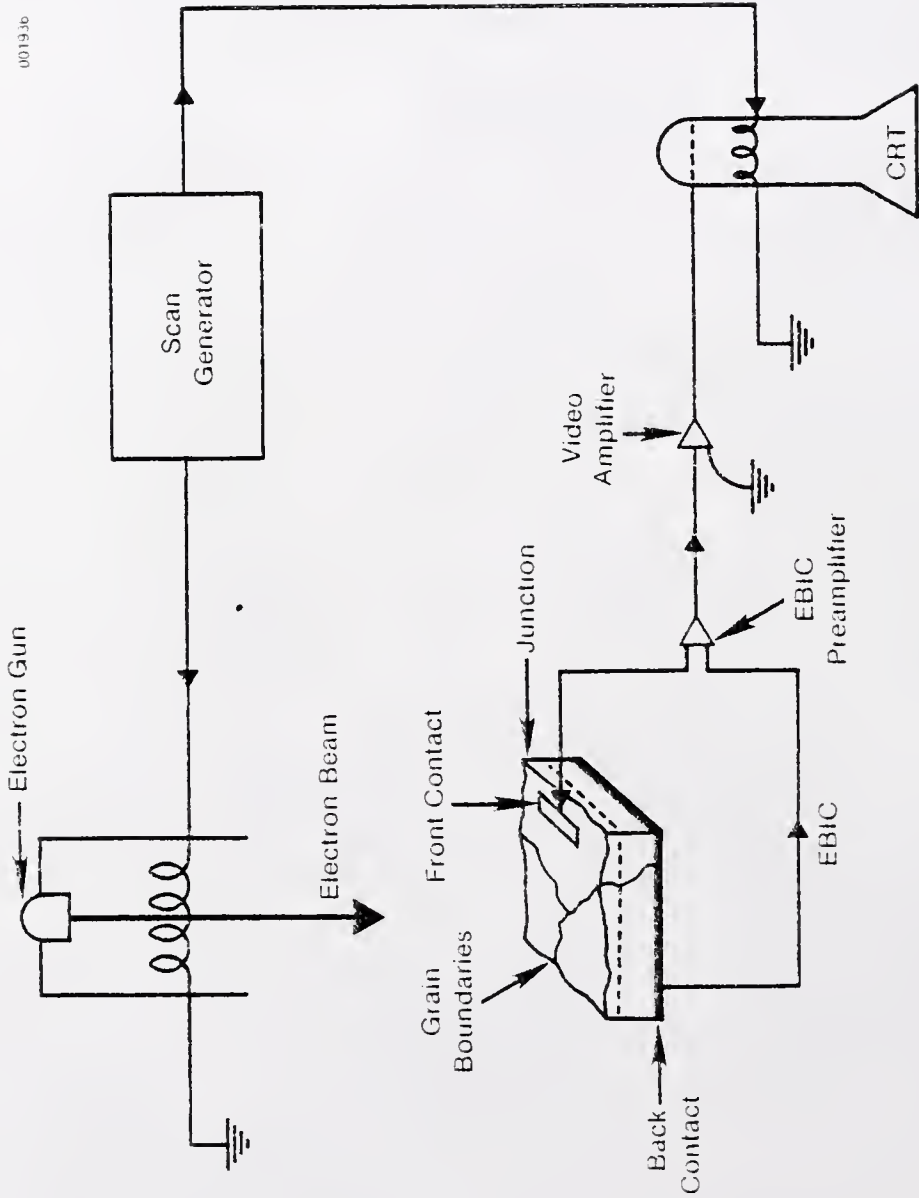


Figure 3.1 Schematic drawing of an SEM configured for obtaining EBIC Images.

This measurement provides information on the amount of current induced in a sample by an electron beam and on the spatial variation of this current. Since the SEM can produce a finely focused electron beam and accurately control its position on a sample, very good spatial resolution is obtainable. In fact, as will be discussed later, the spatial resolution is usually not limited by the size of the primary beam but by properties of the sample itself.

In EBIC measurements, the sample is a radiation detector for a well controlled and well defined electron beam. The properties of the sample determine the efficiency with which it can serve as a detector and thus measurements of collection efficiency contain information on the properties of the sample. It is this property of the EBIC technique that makes it valuable in the study of semiconductor materials. Early uses of EBIC were based on the collection of EBIC images which are basically point by point maps of EBIC collection efficiency displayed as brightness on a micrograph. EBIC images of crystal defects were obtained as early as 1963.⁴⁶ The potential of the technique for device studies and for local carrier diffusion measurements was discussed as early as 1964⁴⁷. Interest in the technique has increased over the years and now the technique is in routine use for semiconductor device and materials studies, and theoretical work aimed at obtaining quantitative information has progressed steadily. Over the years the EBIC technique has been referred to by several different names such as charge collection SEM, conduction mode SEM and similar terms. A thorough discussion of the nomenclature in this field was given by Holt in 1974,⁴⁸ which also is an excellent review of the field up to that date.

To properly understand and interpret EBIC data, one must understand the physics of electron beam-solid interactions as related to carrier generation and the device physics which determine the efficiency with which the sample separates carriers to produce EBIC signals. A complete review of these details has been given by Leamy.⁴⁹ In the following, the details will be reviewed as they apply to the study of polycrystalline silicon material and solar cells.

Typically, electron beams with energies from one to fifty keV are available with conventional SEMs. Beams of this energy range do not produce structural damage in silicon;⁴⁹ however in some device structures the beam can damage oxide layers or interface regions and when such devices are examined this problem must be minimized.^{50,51} In the following, structural damage is assumed to be insignificant.

While a number of loss mechanisms are operating, a primary electron loses energy in a sample predominantly by electron-electron collisions which raise electrons from a filled state in the valence band to an empty state in the conduction band, as illustrated in Fig. 3.2. In the process an extra electron is created in the conduction band and a hole is created in the valence band. The excess carriers will exist for a time called the minority carrier lifetime, τ , after which they recombine. The increase in the number of each type of charge carrier per unit volume is given by:

$$\Delta n = \frac{GI_b \tau}{qV}$$

where G is the number generated per incident electron (i.e. the generation factor), I_b is the beam current, q is the charge of an electron and

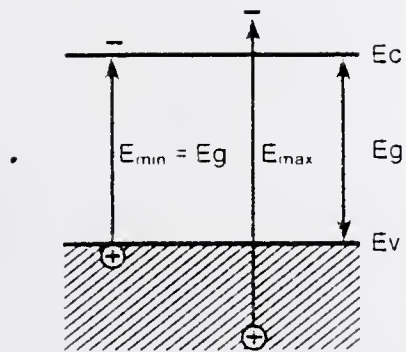


Figure 3.2 Band diagram illustration of the process of forming electron-hole pairs by electron beam bombardment.

V is the volume in which the carriers exist. The generation factor is a function of the beam energy and the material under bombardment. The volume V is determined by the volume in which the energy of the beam is dissipated in the sample (dependent on beam voltage and sample density) and the spreading of carriers into a further volume determined by the carrier diffusion length L. Thus the volume in which carriers exist is actually larger than the volume in which they are generated. This has important implications as to the spatial resolution of the technique. The volume in which carriers are generated is approximately a tear-drop shape and is therefore difficult to describe analytically. A useful approximation of the volume is that of a sphere tangent to the surface,⁵² with the radius of the sphere taken as half the depth of penetration, R, of electrons, in the material. An empirical expression for R has been given as:

$$R = \left(\frac{4.28 \times 10^{-6}}{\rho} \right) E^{1.75},$$

where ρ is the sample density ($\frac{\text{gm}}{\text{cm}^3}$) and E is the beam energy in keV.⁵³ With this simplification the radius of the volume containing the carriers is $\frac{R}{2} + L$. As an example, a 10 keV, 10^{-9} ampere beam will generate a local carrier density of about 10^{15} electron-hole pairs per cm^3 (with $\tau = 1 \times 10^{-5}$ sec, $L = 50$ micrometers, and $G = 2.8 \times 10^3$ electron-hole pairs per electron). This is of the order of typical equilibrium carrier densities in semiconductors, and thus the local carrier generation is large enough to expect large EBIC signals. Also, there is a great deal of freedom in controlling the local carrier generation

density by changing primary beam current and voltage as desired. The processes by which carriers are separated and collected which are described below are valid when the local carrier generation density does not exceed the equilibrium carrier density, which is referred to as low injection conditions. High injection conditions, where the local carrier generation density equals or exceeds the equilibrium carrier density, changes the physics of carrier collection and should be avoided in EBIC work in general. As seen in the above example, this is easily accomplished in silicon by using electron beams of nanoampere or lower beam currents (these are typical beam currents used in SEM work).⁴³ To exceed typical carrier densities of silicon solar cells⁵⁴ ($\geq 10^{18} \text{ cm}^{-3}$) beam currents of microamperes or larger would be required and thus high carrier injection conditions are not common.

The separation and collection of the electron beam induced carriers are identical to the separation and collection of photon induced carriers in the case of a solar cell.⁵⁴ In the case of a p-n junction, the requirement of constant Fermi level, E_F , at equilibrium and the constraint of E_F being near the conduction band, E_C , in n-type material but near the valance band, E_V , in p-type material require that the bands bend near the junction. This is illustrated in Fig. 3.3 which schematically shows the band structure of a p-n junction and the space charge layers on either side of the junction. The junction thus produces an electric field which separates electrons and holes which are generated in or within a few diffusion lengths of the space charge region. The separated carriers essentially never flow back across the junction since the potential barrier opposes this flow. If the n and p regions are

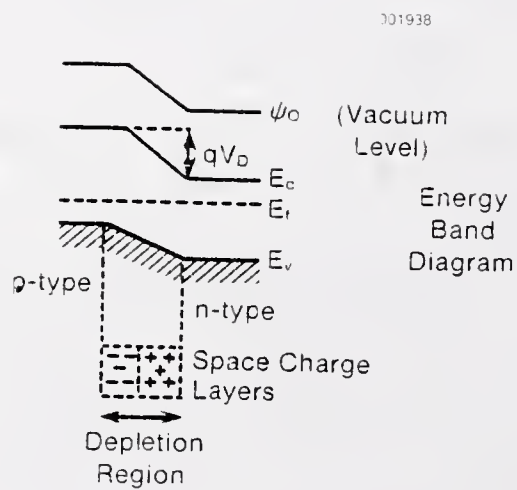


Figure 3.3 Schematic band structure of a p-n junction showing space charge regions.

shorted through an external circuit, the carriers will flow through the circuit to recombine, thus creating a current. This is called the short circuit current, I_{sc} , and no externally detectable voltage is produced. It is this mode of measurement that is described and utilized in this work. It is possible, however, to place a resistance in the external circuit and thus produce power (both a voltage and a current where $I < I_{sc}$). An infinite resistance can be used allowing no current to flow ($I = 0$) during measurement of the maximum or open circuit voltage, V_{oc} . These effects are completely analogous to the corresponding solar-cell effects. When V_{oc} is the measured parameter, the technique is referred to as electron beam induced voltage, or EBIV. A recent application of EBIV demonstrated the use of that technique for the measurement of Schottky barrier height.⁵⁵

The carrier collection efficiency of a junction is given by

$$\eta_{cc} = \frac{I_{actual}}{I_{max}}$$

where I_{actual} is the actual current produced and I_{max} is the current that would be produced if all carriers were separated and collected. The competing process for carrier collection is carrier recombination. In this process, an electron recombines with a hole to neutralize each other. Recombination generally occurs via an intermediate stage in which one of the carriers becomes trapped at a specific point in the crystal. The distance traveled by an average carrier before trapping occurs is expressed as $\frac{1}{\sigma N_T}$, where N_T is the trap density and σ is the trap cross section. Thus, carriers moving with thermal velocities, V_{th} ,

travel freely for a time τ before trapping where $\tau = \frac{1}{jN_T V_{th}}$. The lifetime of a carrier pair is determined by the lifetime of the minority carrier since many majority carriers are available to recombine with the trapped minority carrier. In an n-type material the recombination rate, R , is given by the excess hole density, Δp , divided by the hole lifetime, $\frac{\Delta p}{\tau}$ when Δp is small. However if Δp is not small, degenerate conditions exist ($\Delta p \sim \Delta n$) and recombination rates are not controlled by minority carrier lifetime.

Under steady state conditions, as carriers are generated in a given region equal numbers are lost either through motion out of the region or by recombination. The recombination rate will be proportional to the local carrier density as mentioned above. Carrier motion out of a given region is determined by diffusion and/or drift fields. The conditions of steady state result in the continuity equations for electron and holes:

$$g - \frac{1}{q} \nabla J_e - \frac{\Delta n}{\tau_p} = \frac{d}{dt} \Delta n = 0 \text{ for electrons}$$

and

$$g - \frac{1}{q} \nabla J_h - \frac{\Delta p}{\tau_h} = \frac{d\Delta p}{dt} = 0 \text{ for holes,}$$

where g is the carrier generation rate and J_e and J_h are the electron and hole fluxes respectively with units of $(\text{cm}^{-2} \text{ sec}^{-1})$.⁵⁶ These equations are valid for semi-infinite materials that contain a homogeneous distribution of carrier traps and where recombination occurs at a rate

proportional to the local carrier density. When the flux is determined by diffusion $J_h = -qD_p \frac{\partial \Delta p}{\partial x}$ where D_p is the diffusion coefficient for holes in cm^2/sec . The appropriate solution of the continuity equation in this case is of the form $\Delta p = \text{constant } e^{-x/L_h}$ for $g = 0$, where $L_h = \sqrt{D_h \tau_h}$ is the minority carrier diffusion length. Thus L is an extremely important parameter and is best visualized as a description of the average distance between the point of creation and the point of annihilation of a minority carrier. Since L depends on the trap density N_t , it is subject to change during processing of semiconducting materials into devices. Thus the measurement of L provides a relative figure of merit of the material quality which allows simple comparisons for material at various stages of processing or of different sources, purity, etc.

A simple EBIC technique for determining L was first pointed out by Miyazaki and Miyaji⁵⁷ by analogy with scanning light spot techniques. They solved the continuity equation by applying the boundary condition $\Delta p = 0$ at the depletion region edge, i.e., that no free carriers can exist at the depletion region edge. This, along with the above solution (which assumes diffusion controlled fluxes) and ignoring of the presence of the sample surface yields $I_{CC}(x) = I_{\text{max}} e^{-x/L}$ where I_{max} is the maximum EBIC current and $I_{CC}(x)$ is the EBIC current collected at any distance x from the depletion region edge. This derivation also assumes point source carrier generation, which can only be considered as accurate for distances larger than the electron range. To make use of this expression for the determination of L , an experimental arrangement is needed where I_{CC} can be measured as a function of distance between the

incident electron beam and the depletion region edge. Such an experimental arrangement is illustrated in Fig. 3.4 wherein a perpendicular p-n junction geometry is utilized. The EBIC signal is plotted on a logarithmic scale as a function of beam position, x , and the resulting slope is the inverse of L . There are two serious limitations for this technique: (1) the assumption of point source generation, and (2) neglect of the sample surface where recombination can occur. The point source generation assumption is valid when low beam voltages are used and hence the generation volume becomes small compared to L . However, at low beam voltages the neglect of surface recombination becomes less valid since more carriers are generated, and hence recombined, near the sample surface. However, in spite of these limitations, this technique has been the basis for many useful studies and is quite adequate when qualitative comparisons between different regions of a sample or different samples are desired and will only be used for qualitative comparisons in this work.

As mentioned above, the presence of a semiconductor surface influences the carrier recombination. To analytically treat surfaces or planar boundaries, appropriate boundary conditions must be specified for the solution of the continuity equations. By analogy with the case for bulk material, the recombination rate at a surface is assumed to be proportional to the product of trap density per unit area, capture cross section per trap and the thermal velocity. This quantity has dimensions of cm/sec and is consequently known as the surface recombination velocity, S . Likewise for a grain boundary S_{gb} is defined as the grain boundary recombination velocity. The minority carrier flux that is

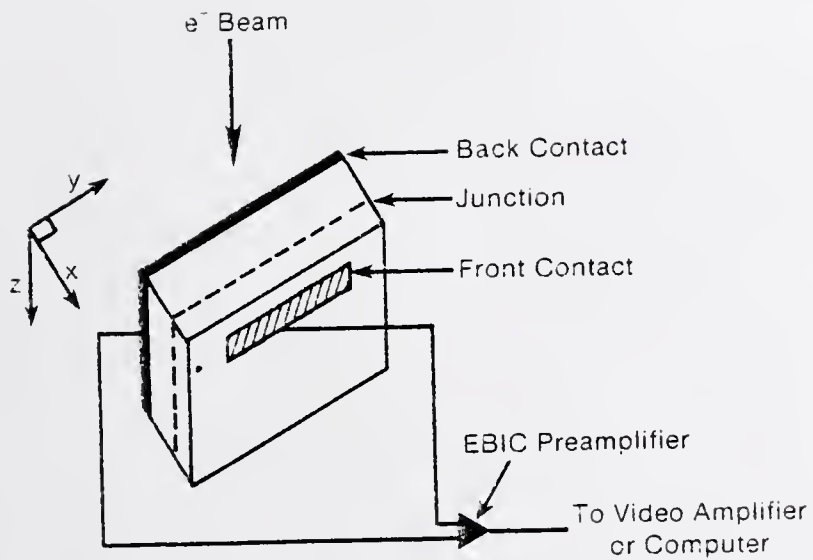


Figure 3.4 Schematic illustration of EBIC specimen geometry utilizing a perpendicular p-n junction to allow collection of I_{CC} as a function of distance to the depletion region edge.

absorbed at a surface of recombination velocity S is therefore $S\Delta p$ and the boundary condition for diffusion to the surface is:

$$S\Delta p = D_n \left. \frac{\partial \Delta p}{\partial z} \right|_{z=0}$$

where z is the surface (or plane) normal. Since surface properties are very important to device performance and processing steps can easily alter S , a convenient method to determine S is valuable.

Watanabe et al.⁵⁸ developed and illustrated a relatively simple EBIC technique for determining S . They made use of the idea proposed by van Oopdorp⁵⁹ that carrier removal at the surface results in an effective weakening of the source strength. Using this idea, Hackett⁶⁰ solved for Δp and reports:

$$\Delta p = g\tau \left[1 - \frac{s}{1+s} \exp\left(-\frac{\xi}{L_b}\right) \right]$$

where ξ is the electron range. This may be rewritten in terms of an effective source strength, g_{eff} , such that

$$\Delta p = g_{\text{eff}} \tau$$

where

$$g_{\text{eff}} = g \left[1 - \frac{s}{1+s} \exp\left(-\frac{\xi}{L_b}\right) \right].$$

Here $s = \frac{S\tau}{L_b}$ is the reduced surface recombination velocity which is a dimensionless quantity. Using these concepts it may easily be shown that⁵⁸

$$\frac{\partial}{\partial \xi} \ln g_{\text{eff}} \Big|_{\xi=0} = \frac{S}{D} .$$

This says that the derivative of the natural logarithm of the effective source strength evaluated at the surface (i.e., when the electron range goes to zero) is equal to the surface recombination velocity of that surface divided by the carrier diffusivity.

To make use of the above relationship in EBIC work, the fact that the EBIC current is proportional to the excitation strength is utilized. The constant of proportionality between the EBIC current and the effective generation strength will depend on the geometry of the junction and the surface and can be expressed as

$$I_{\text{EBIC}} = k g_{\text{eff}}$$

where k is the constant of proportionality. Thus substituting into the previous equation one gets

$$\frac{\partial}{\partial \xi} \ln I_{\text{EBIC}} \Big|_{\xi=0} = \frac{S}{D} .$$

This relationship thus provides a method for determination of the surface recombination velocity by simply measuring I_{EBIC} as a function of the distance of excitation from the depletion region. This may be accomplished by varying the primary electron beam and hence the electron range as has been demonstrated by Watanabe et al.⁶¹ An extension of this analysis technique to the study of grain boundary recombination

velocity has been used in this work. Here, the electron range ξ is replaced by the distance of the electron beam from the grain boundary of interest and the EBIC signal is obtained as a function of that distance. An alternate method for determination of grain boundary recombination velocity has been developed by Zook.⁶² Zook's approach, based on the light beam induced current (LBIC) technique,⁶³ utilizes computer assisted curve fitting of LBIC or EBIC data along with a knowledge of the absorption coefficient of the light or electrons utilized, to determine S_{gb} . Seager⁵⁴ compared Zook's analysis with that described above (and used in this work) and concluded that recombination velocities determined as in this work may be a factor of 2 to 10 too low due to the size of the excitation volume. This is due to the fact that the finite size of the carrier generation volume allows for carriers to be generated at the grain boundary when the point generation model assumes generation only at a finite distance away from the boundary. While Zook's analysis makes a more realistic assumption on localized carrier generation, it requires curve fitting to deduce S_{gb} and has not been shown to produce values of S_{gb} more accurately than the approach used in this work.

In this work, interest in the EBIC technique stemmed from a desire to study the electrical effect of grain boundaries in polycrystalline silicon solar cells. It had been shown that the photovoltaic response of a polycrystalline silicon solar cell changes dramatically in the immediate vicinity of a grain boundary.⁶⁵ The EBIC technique was first developed in this work as a means of obtaining a short-circuit current map of a fabricated polycrystalline silicon device. This allowed investigation of the spatial uniformity of device response, the extent of

grain boundary influence on intergrain response and the differences in response of various grain boundaries and twin boundaries.

While the development of qualitative EBIC imaging techniques was relatively straightforward, the attempt to obtain quantitative information from EBIC revealed major deficiencies in existing or commercially available EBIC systems. These deficiencies include lack of beam current control and regulation, lack of accurate beam positioning capabilities, inaccuracies in EBIC measurement circuits and no method for automated acquisition, storage, display and manipulation of data. Furthermore, no available sample stage was suitable for rapid sample insertion through a vacuum interlock which allowed for EBIC connections. It was also desired to tilt the stage through 90 degrees to allow for EBIC measurements with the electron beam either parallel or perpendicular to the device junction without remounting the sample. Also, the reproducibility and accuracy of EBIC measurements were not known and neither were the effects of the electron beam on the device properties. In Chapter Five of this thesis, the development of an automated EBIC system is described in detail. This system has provided the solution to the problems mentioned above by incorporating many control options for data acquisition, storage, display and manipulation. Also, suitable EBIC sample stages were developed as part of this system. In Chapter Six the problems of EBIC reproducibility and accuracy, and beam damage effects were investigated.

With the EBIC system well developed the EBIC technique was then used to study polycrystalline silicon solar cells. Chapter Seven describes a series of EBIC studies on active grain size, activity of

grain boundaries versus twin boundaries, percentage of active grain boundaries and the spatial extent of grain boundary electrical influence. Also, p-n junctions at and near grain boundaries were investigated with cleaved and/or beveled samples. These studies were complemented by standard optical microscopy measurements of grain size, grain structure, and stained junctions.

Finally in Chapter Eight a more quantitative application of EBIC to the study of polycrystalline silicon solar cells is described. This study focused on the effects of heating (at temperatures appropriate for solar cell device fabrication) on the electrical properties of silicon grain boundaries. This work was complemented by extensive chemical and structural analysis of the same grain boundaries by surface analysis techniques and electron microscopy.

CHAPTER FOUR
EXPERIMENTAL DETAILS

Material

The basic material used in this work was cast polycrystalline silicon manufactured by Wacker-Chemitronic of Germany.⁶⁶ The starting material for the casting process is high purity semiconductor grade silicon. The silicon is first melted in a quartz crucible and then poured through a quartz funnel into a preheated graphite mold.⁶⁷ The mold is of square cross section of $106 \times 106 \text{ mm}^2$ or $162 \times 162 \text{ mm}^2$. The mold is rotated during the pouring to ensure an even heat distribution and to develop a homogeneous chill-layer of solid silicon before the silicon melt can react with the mold walls to form silicon carbide. The funnel used is thermally stabilized with graphite supports to help balance inhomogeneities in the silicon melt. A heated mold is used to avoid cracking problems commonly encountered with cold mold casting.

During the solidification process, a water cooled rotating shaft is used to adjust the vertical controlled temperature gradient. Heat removal rates are controlled with an intermediate thermal insulation layer between the water cooled shaft and the mold. It is found that sufficient heat loss from the free surface of the melt occurs for a solid layer to form on top. Thus, the last region to solidify is the interior of the casting. Since silicon expands during freezing, the melt surface must be kept open until the end of the solidification process to avoid cracking of the ingot or the development of highly stressed zones.

The base dopant is incorporated in the melt; boron doping at levels of approximately 10^{16} atoms/cc is utilized for p-type material. Phosphorus doping at approximately 10^{15} atoms/cc is utilized for n-type material. The ingots are cut into wafers approximately 17.7 mils thick and were received for this work in this form.

Impurities identified by other investigators in Wacker polysilicon include C, O, Mg, Al, Ni, Fe, Co, Ti, Cr, Ca, Mg and K.⁶⁸ Strong segregation to incoherent grain boundaries has been demonstrated for the impurity elements Fe, Co, Te, Cr, Ca and Mg. Macrosegregation in the direction of solidification for the slow-diffusing dopants As, Sb, B and the light elements C and O has been reported.⁶⁹ Silicon carbide precipitates have also been observed. Details on the grain structure of this material and further details on grain boundary chemistry are presented in this work.

Electron Beam Induced Current

Electron beam induced current (EBIC) measurements were made on three different instruments. The Japanese Electron Optics Laboratory (JEOL) JSM 35C scanning electron microscope (SEM) in the Department of Materials Science and Engineering at the University of Florida was used for all early work. This system is equipped with a GW Electronics Model 103 absorbed current monitor. Diodes were normally contacted typically by bonding a wire with silver paste to the emitter and connecting to ground of the microscope. The base contact was made via silver paste to the isolated sample stage, and taken to the preamplifier of the absorbed current monitor by a standard BNC cable. This system was used mainly

for qualitative work (e.g. EBIC micrographs) and for initial semi-quantitative measurements of diffusion length and surface recombination velocity. The vacuum in this system was created by a standard oil diffusion pump system with a liquid nitrogen cold trap. Typical operating pressures were in the 10^{-5} Torr range.

A second JEOL JSM 35C system located at the Solar Energy Research Institute was also used. This system is similar to the one at the University of Florida with the addition of a remote controlled Faraday cup for beam current measurements, a beam current stabilizer system, beam voltage up to 49keV and a turbomolecular vacuum pumping system. Typical operating pressures for this system were in the low 10^{-6} to high 10^{-7} Torr range. This system was modified for automated EBIC measurements for this work as described in a later chapter.

The majority of the quantitative EBIC data was taken on a Cameca MBX electron probe microanalyzer (EPMA) located at the Solar Energy Research Institute. This system is equipped with fast beam blanking capabilities, remote controlled Faraday cup, beam current regulation, motorized stage controls and a Tracor-Northern TN-2000 automation system with TN-1310 controllers. The system is evacuated with a turbomolecular pump and has an anticontamination system consisting of a liquid nitrogen cooled cold plate. Typical operation pressure during analysis was in the low 10^{-7} Torr range. Automation and optimization of this system using a Tracor Northern TN1244 beam current monitor and a Keithly Model 480 picoammeter are described in detail in Chapter Five.

The EBIC stage used on the Cameca MBX is shown in Figure 4-1. It consists of a modified Cameca stage designed for voltage contrast

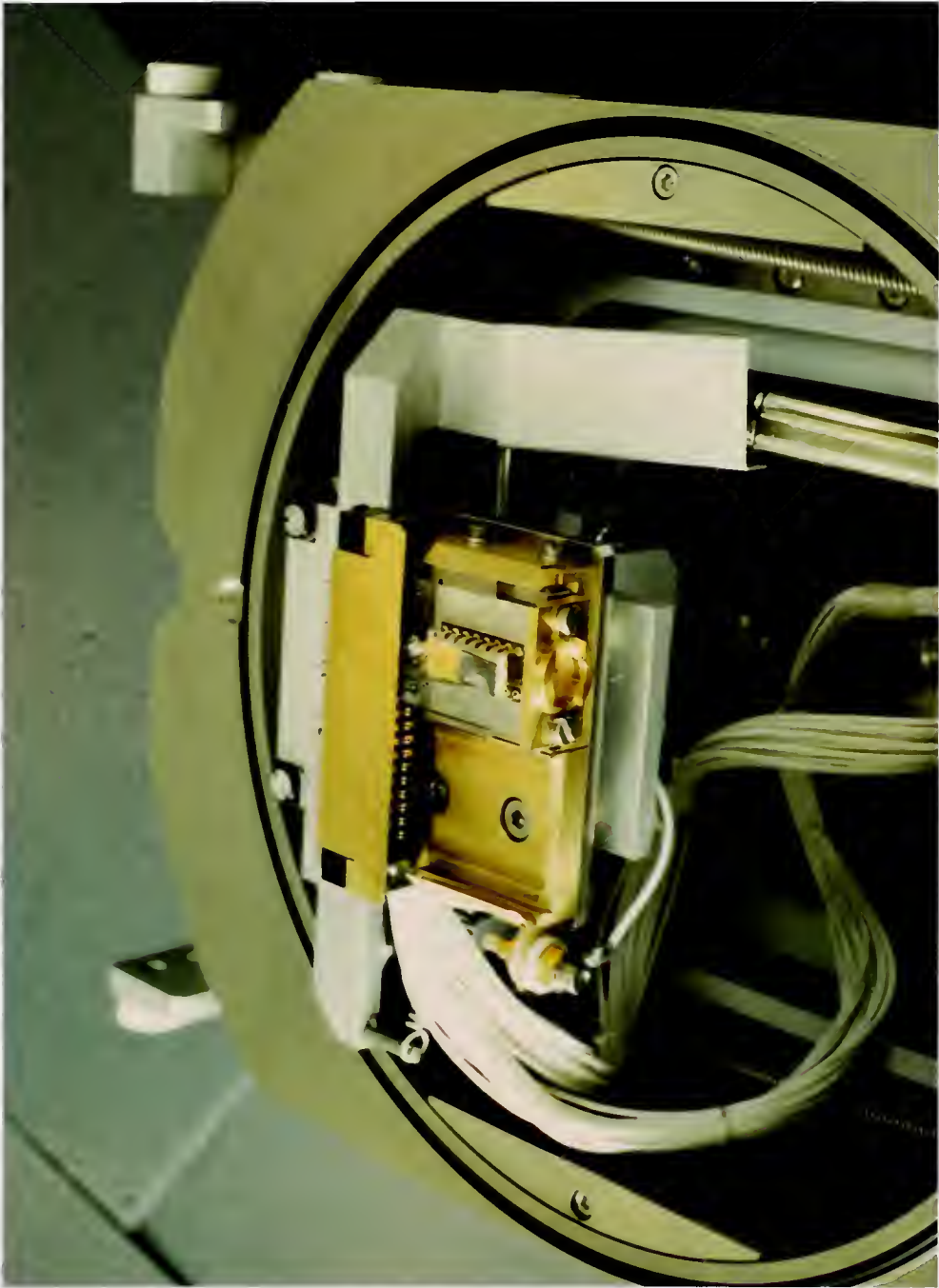


Figure 4.1.1 Photograph of EBIC stage used with the Cameca MBX EPMA system.

microscopy of integrated circuits. A gold-ceramic 16 pin flat pack was converted to a gold base stage (for back contact) and a gold or tungsten probe was added for front contact. A Faraday cup is also incorporated into the stage for precise beam current measurements. An external coding matrix was used to allow external reconfiguring to measure either beam current, absorbed current or induced current with the sample in place.

Transmission Electron Microscopy

Transmission electron microscopy (TEM) was performed on a JEOL 100CX scanning transmission electron microscopy (STEM) located at the Solar Energy Research Institute. Chemical jet techniques were initially tried for sample thinning, but problems of preferential grain boundary etching were always encountered. Therefore all samples were first thinned mechanically and further thinned with a Balzers IEU 100 ion miller. In this apparatus, a focused argon ion beam sputtered the surface atoms and the sample was continuously rotated during the thinning process to minimize surface roughness. The ion miller was evacuated with a turbomolecular pump. Typical pressures during ion milling were in the 10^{-5} Torr range.

Ion Microscopy and Secondary Ion Mass Spectroscopy

A Cameca IMS-3F second generation ion microprobe was used for ion microscopy and secondary ion mass spectroscopy (SIMS) analysis. A

schematic of this system is shown in Fig. 4.2. The major components of this system are (1) ion source, either of cold cathode duoplasmatron type for an oxygen primary beam or a thermal ionization type for a cesium primary beam; (2) a three lens primary beam column for control of ion beam current, size, position and rastering; (3) sample chamber with a rapid sample exchange system; (4) transfer optics which direct the secondary ions into the analyzers while maintaining spatial information; the optics includes variable entrance slit, variable contrast diaphragm, variable field limiting aperture, electrostatic energy analyzer, variable energy slits, image transfer lens to transfer image to mass analyzer, electromagnet for mass analysis, variable exit slit, and electrostatic analyzer to divert the secondary beam to either counting or imaging sections; (5) Faraday cup for high current counting; (6) electron multiplier for high accuracy counting; (7) projection lens for imaging; (8) microchannel-plate for ion multiplication; and (9) fluorescent screen for ion to photon conversion.

In the ion microscope mode, the system is a direct imaging type (i.e., no rastering required). Spatial resolution up to approximately $0.5 \mu\text{m}$ is attainable and magnification is variable from 50X to 1000X. Either a polaroid or 35mm camera (outside the vacuum) is used to record the image from the fluorescent screen. The primary beam size is adjustable from $2 \mu\text{m}$ to $500 \mu\text{m}$, and rastering is fully adjustable from 0 to $500 \mu\text{m}$. Primary ion densities on the sample of greater than 50 mA/cm^2 are easily attained.

The primary beam is accelerated (up to 20keV) and focused onto a sample held at 4500 volts with respect to ground. The primary beam may

001948

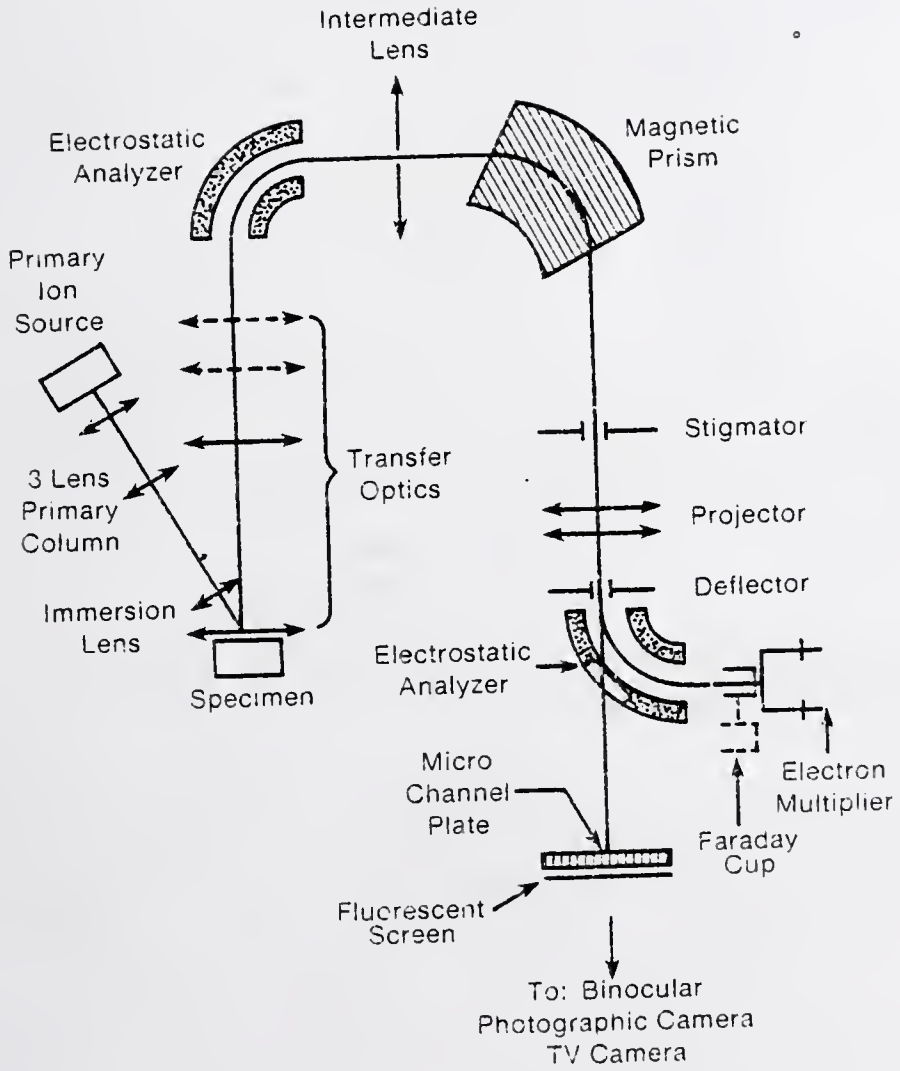


Figure 4.2 Schematic of Cameca IMS-3F ion microprobe used in this work.

be deflected into a Faraday cup to measure primary beam current. Secondary ions are accelerated from the sample by the 4500V, but also have their own energy distribution. These secondary ions are initially collected by an immersion lens, which is physically very close to the sample. The transfer optics then image the secondary ions on the image plane of the first electrostatic analyzer. At crossover, a variable entrance slit is used to minimize aberrations. A contrast diaphragm is selected and centered at crossover to minimize image aberrations while maintaining high transmission. A field limiting aperture may also be selected to allow mechanical gating (i.e., to avoid crater edge effects in depth profiling) if desired. It is centered in the image plane. The electrostatic analyzer provides energy dispersion and an energy slit is used to select the desired energy and energy resolution. A spectrometer lens is then used to transfer the image from the electrostatic analyzer to the focal plane of the magnet for mass analysis. The electromagnet provides mass dispersion and is computer controlled to allow only the ions with the desired charge-to-mass ratio to enter the final portion of the analyzer. A projector lens is used to focus the mass and energy filtered image onto a channel plate image converter or an electrostatic deflector is used to divert the beam to the ion detector for pulse counting. The entire system is controlled via a Hewlett-Packard 9845 desk-top computer.

The instrument is evacuated by three major vacuum sub-systems. The primary column is pumped with a turbomolecular pump with ultimate pressure in the low 10^{-8} Torr range. The primary column pressure is 5×10^{-6} Torr when using the duoplasmatron source or 10^{-7} Torr when using the

cesium thermal ionization source. The sample chamber is cryopumped and the ultimate pressure is 2×10^{-9} Torr. Typical operating pressure is about 10^{-8} Torr with either source operating. A turbomolecular pumped rapid sample introduction chamber is utilized. The analyzer section is pumped with dual ion pumps and can be isolated from the sample chamber and gun regions by a vacuum valve. Vacuum in the analyzer section is maintained in the low 10^{-8} torr range.

Auger Electron Spectroscopy

All Auger electron spectroscopy (AES), scanning Auger Microscopy (SAM) and some of the secondary ion mass spectroscopy (SIMS) measurements were made in a Perkin Elmer (PHI) 590 scanning Auger system. This system was equipped with a differentially pumped Argon ion sputter gun and a PHI quadrupole mass spectrometer based SIMS system. The system is ion pumped with operating pressure in the 10^{-10} Torr range.

The PHI 590 system was used for all in-situ vacuum fracturing studies. The actual fracturing was conducted with a commercially obtained PHI sample fracture attachment. The basic mechanism used in the fracture device was a spring loaded hammer used to impact the edge of a firmly secured sample.

CHAPTER FIVE

DEVELOPMENT OF AUTOMATED EBIC SYSTEM

Introduction

A fully automated system for EBIC measurements has been developed, based on a Tracor Northern TN-2000 X-ray analysis automation system. The system provides for complete control of both the electron beam and the specimen stage, and for automated data gathering. Specific uses include totally automated carrier diffusion length measurements and grain boundary effective surface recombination velocity measurements. The system has been successfully used with both a Cameca EPMA and a JEOL SEM.

The electron beam induced current, or EBIC, technique is a powerful tool for the investigation of semiconductor materials and device properties as discussed in Chapter Three. The major advantage of EBIC over other techniques is the spatial resolution obtainable. Typically, spatial resolution on the order of one micron is easily obtainable and some information on a tenth or hundredth of a micrometer scale can be deduced. For example, Ourmazd et al. has recently reported the obtaining of 3000 Å EBIC spatial resolution in silicon samples.¹⁷

There are two disadvantages to the EBIC technique: one is the complexity of theoretical modelling to accurately deduce quantitation parameters and another is the state-of-the-art of the EBIC measurement system. Most modelling to date has utilized a point source carrier generation assumption, while in reality the carrier generation volume is of the order of a micron.⁴⁹ More exact modelling results in three

dimensional boundary value current flow equations for which analytical solutions cannot be found.

In this chapter significant improvements to the state-of-the-art in EBIC measurement systems are described. The system developed is totally automated and includes such features as computer control of beam current regulation and selection, beam blanking, and digital data recording, displaying and manipulation. The manual system on which the automation is based will first be described. Then a complete description of the automated system including hardware, software and several examples of the use of the system will be detailed. The most commonly desired form of EBIC data is either EBIC or log EBIC versus beam position. Thus, it is this type of output that will be addressed in the following.

Procedure Required for Manual Measurements

The manual technique used to provide an induced current line scan (EBIC versus electron beam position) requires a well controlled electron beam with a linescan mode, a low-noise and low input impedance picoammeter with analog output, and a strip chart recorder with a DC offset. A slow electron beam scan rate is used (approximately 1 millimeter per second) and the scan speed must be accurately measured.

Because the instantaneous induced current is typically 10^{-6} to 10^{-12} amperes, the picoammeter needs to be as close as possible to the SEM sample chamber (ideally inside the sample chamber) to limit current loss in the connecting cables and to limit extraneous electrical noise from entering the circuit. It is important that the two terminals of the photovoltaic device lead directly into the picoammeter remaining

isolated from the system ground to avoid the condition where the magnitude of electrical noise is about equal to the induced current. The analog output of the picoammeter is sent to the video circuitry to obtain an EBIC image or a linescan on the SEM image screen (cathode ray tube or CRT) with normal magnification, brightness and contrast control. This gives a qualitative measure, i.e., a map of the current response of the sample.

To make the technique more quantitative, the picoammeter analog output can be fed into a high resolution strip chart recorder. Appropriate adjustments can then be made on the recorder to obtain a highly detailed and resolvable linescan of I_{EBIC} versus electron beam position. Since the beam scan speed has been accurately measured and the chart speed is known, the beam position can be determined. This procedure will give accurate quantitative results. The quantities of interest (L_{eff} and/or S_{eff}) can be calculated from the curve of $\ln(I_{EBIC})$ versus position.²¹ If a logarithmic amplifier or chart recorder is used, the data reduction is greatly simplified but the accuracy may be less.

In practice, it has been found highly desirable to have two separate EBIC measuring arrangements for measuring I_{EBIC} , one for imaging and a separate one for quantitative data gathering. For imaging, it is desired to continuously measure the EBIC current, amplify it and convert it to a zero to ten volt analog input to the normal SEM display intensity input. Since the output is recorded as an inherently qualitative gray scale on a micrograph, the accurate calibration of this amplifier chain is not crucial. The time response of this imaging circuit must be

fast enough for use with normal SEM imaging speeds, although only the slow scan speeds are applicable. The signal can be processed by all normal image processing modes of SEM including DC suppression, gain, non-linear amplification or gamma, and filtering through a band-pass filter if desired.⁴³

The major problem encountered in EBIC imaging is electrical noise. This occurs as either random noise, especially at very low current levels, or 60 cycle noise usually resulting from ground loop problems or improper shielding. To avoid these problems, a current preamplifier is placed in a double-shielded, isolated case as close as possible to the microscope, thus reducing problems of noise pick-up along the cables. A photograph of this arrangement is shown in Fig. 5.1. Figure 5.2 is an EBIC micrograph with 60 cycle noise showing the dramatic effect it has on the image. This noise is effectively eliminated with the configuration shown in Fig. 5.1.

When quantitative EBIC data are desired, speed is no longer the major concern for the EBIC measurement circuit, while accurate calibration of the current amplifier is crucial. It is desired to measure, as accurately as possible, the EBIC current essentially on a point by point basis for correlation with the position of the electron beam on the sample. This mode does not require a signal that is compatible with the SEM image signal processing; the only requirement is that the current values can be read and recorded. For use in a manual mode, a picoammeter with analog output compatible with the strip chart recorder is adequate. The Keithley 480 digital picoammeter chosen for this setup

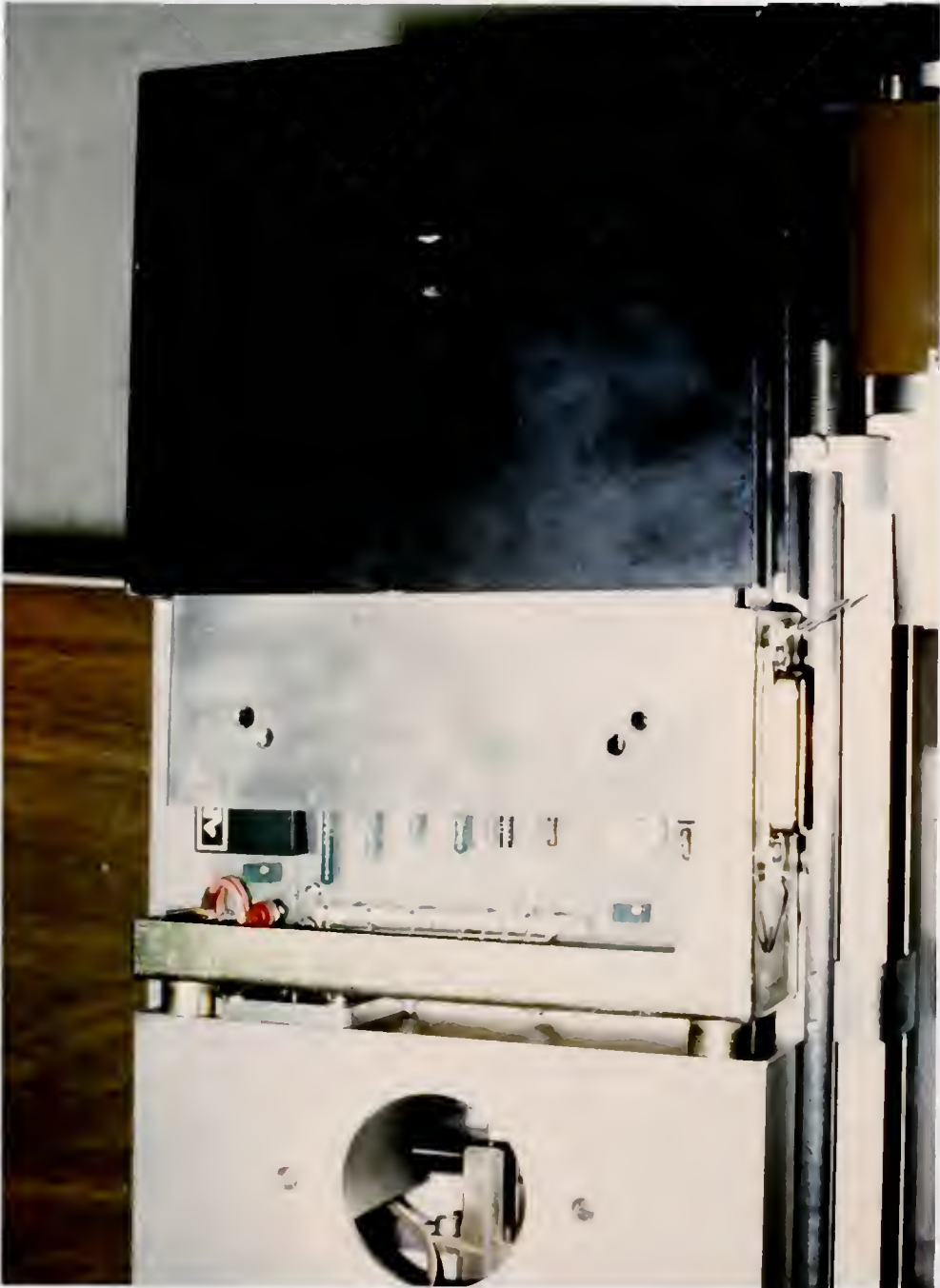


Figure 5.1 Photograph of EBIC preamplifier system used on the Cameca MBX electron microprobe, showing double-shielded, isolated housing which is attached directly to the sample chamber.

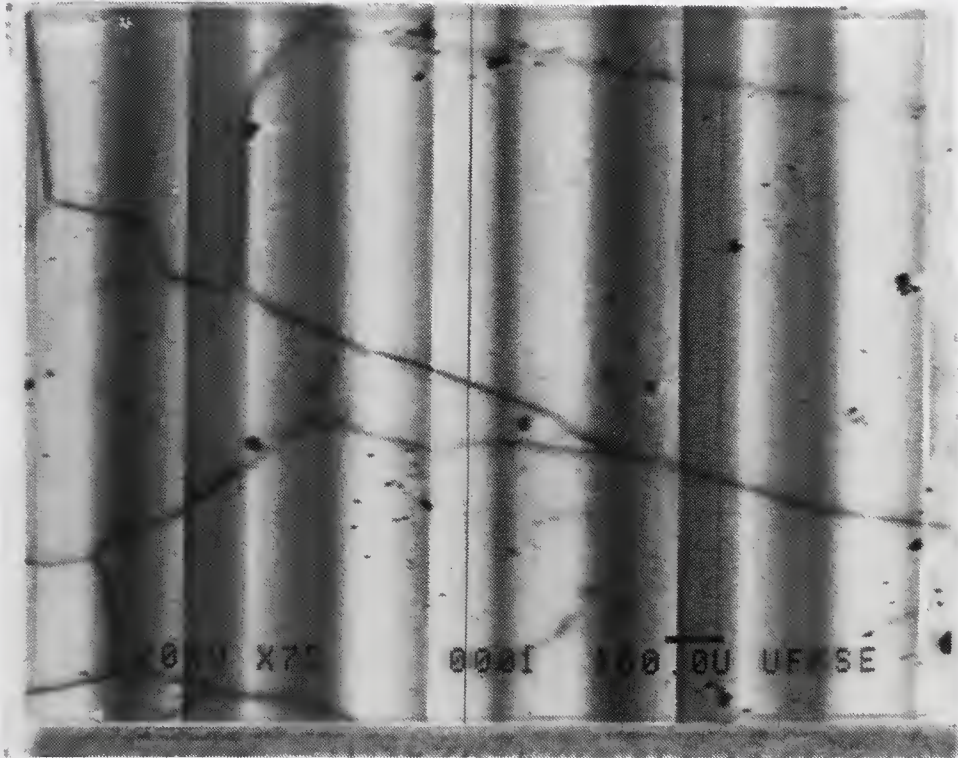


Figure 5.2 EBIC micrograph showing the problems of sixty-cycle noise pickup which can be effectively eliminated using the amplifier system shown in Fig. 5.1.

also provides a digital readout of the current for visual data collection. As discussed in the next section, the measured current can also be easily input into a computer.

The disadvantages of the manual technique include the tedious nature of the process of manually reading off of the chart, time consumption, and increases in the chance for error. The many advantages of automating this technique are discussed next.

Advantages of Automation

With the use of an SEM computer control system, the manual linescan technique described above can be completely automated. The advantages of this arrangement are significant. The computer can read a digital picoammeter easily, accurately and quickly. The values are easily stored in computer memory to be manipulated as desired. For instance, the natural logarithm of the current readings can be derived by one computer program line and then tabulated or plotted on a CRT display or on a digital plotter and stored on floppy disk. This method saves much time and improves accuracy by eliminating human error inherent to the manual method.

Digital beam control is used to accurately position the beam in known discrete steps which allows a much more accurate digitized line scan to be plotted. This is much more accurate than the manual analog technique which incorporates error in the scan speed measurement and additional error in the chart speed (depending on the quality of the recorder). The accuracy of the digital system is limited by the magnification accuracy, the stability of the electron optics and the accuracy

of the current amplifier used for the particular current level. This has been measured as $\leq \pm 2\%$. With the automated approach, the operator can readily specify the distance between data points and the dwell time for each measurement that is appropriate for the particular device under study. This is very important for a system designed to be used on all photovoltaic materials. For example, very different scales are used for direct gap as opposed to indirect gap materials.

Other advantages of an automated measurement are computer controlled electron beam current regulation to within $\pm 0.1\%$ per hour and computer controlled beam blanking to minimize beam damage on the specimen. One also has the option of moving a motorized stage in known increments with respect to a fixed beam, to allow very long linescans without introducing beam divergence problems.

Specifics of the System

The basic EBIC automation system has been designed for a Cameca MBX electron probe microanalyzer (EPMA), equipped with a Tracor-Northern TN-2000 automation package with digital beam control. The normal function of the TN-2000 system is to provide a computer-generated, digital, external input to the scan generator and to control the imaging of an SEM to facilitate x-ray mapping or image analysis. The overall EBIC system has been designed for maximum flexibility and, as will be discussed later, has been used on a JEOL JSM 35C. This extension demonstrates the ease with which the system can be modified for use on an SEM or EPMA from another manufacturer. The approach could likewise be extended for use with other automation systems, as long as a digital

beam control system is available. The software, however, would have to be rewritten in the appropriate language. This extension is currently under investigation for use with an Ortec EDS II system with Image Master option, for which the language ORACL is used.

The TN-2000 system is based on a Digital Equipment Corporation (DEC) PDP 11/23 computer with 64K of core memory. Included are Data Systems DSD 440 dual floppy diskette mass storage system, a DEC LA120 Decwriter III high speed teletype for hardcopy output and a Hewlett Packard 7221B four pen digital plotter for graphics output. Figure 5.3 is a block diagram of the major hardware components in the total system.

The TN-2000 controls the following functions on the EPMA:

- 1) beam scanning coils;
- 2) Faraday cup insertion for beam current measurement or beam blanking;
- 3) fast beam blanking via blanking coils;
- 4) stage motion via stepping motor drives in X, Y and Z directions;
- 5) beam current selection (from a user defined table of 64 currents);
- 6) beam current regulation and measurement; and,
- 7) all X-ray spectrometers and associated hardware.

By monitoring the current from a beam regulation aperture, the computer continuously adjusts the condenser lens current keeping the beam current constant.

Block Diagram of Automated EBIC Linescan Measurement System

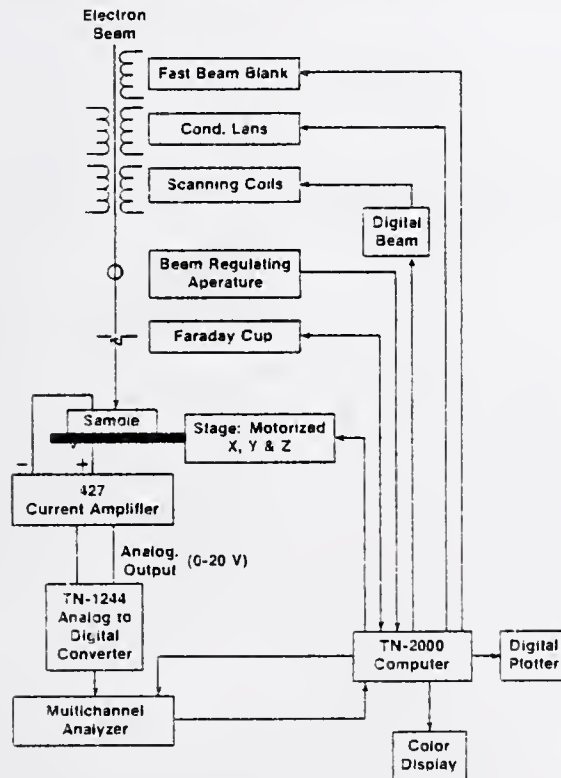


Figure 5.3 Block diagram of the major hardware components of the automated EBIC system on the Cameca MBX electron microprobe.

Using a "CUP" command, the computer will place a movable Faraday cup into the beam path. The Keithley picoammeter measures the cup current directly and an ADC reads the analog output of the picoammeter. A scaler is used to count the pulses for visual readout. The beam current is thus measured and stored into the software for future reference. The Faraday cup also acts as the beam blanking device most effectively since it is physically located below the beam regulation aperture and therefore does not affect the beam regulation when it is positioned and removed repeatably.

It is sometimes desirable to have very fast (<1 microsecond) beam blanking capabilities. This is best accomplished by installing blanking coils to deflect the electron beam just after the anode. Uses for this type of blanking include lifetime studies based on short circuit current decay and the obtaining of very low (i.e., less than one sun equivalent) injection levels. A serious problem is encountered when the beam blanking coils are used in conjunction with the beam current regulation. When the beam is blanked, the regulation system responds to the loss of beam current by opening up the condensor lens all the way. When the blanking coils are turned off, the beam is very intense and the regulation system adjusts the condensor lens current until the present current is measured on the regulation aperture. The problem, however, is that the condensor lens is now on the wrong side of crossover, resulting in an erratic, unfocussed beam. These problems could be overcome by injecting a constant signal to the regulation system during blanking, holding the condensor lens current constant until the beam is

restored and allowed to stabilize. This approach would allow operation in a regulated mode for time resolved EBIC (TREBIC) studies.⁷⁰⁻⁷²

The software has been written to allow the operator to digitally define the beam scan by telling the computer the start point, the end point (within a viewing frame at a given magnification) and the distance to step between each data point depending upon the desired resolution. The computer then steps the beam as defined and counts the current at each data point. A variation of this is to keep the beam stationary and move the stage in given increments in a given direction. In this case, the resolution is limited to one micrometer whereas the resolution for the digital beam case is only limited to whole increments of CRT picture points; there 4095 by 4095 picture points horizontally and vertically across the CRT. It is desirable to use the stage-scan mode in the case of low magnifications in order to keep the solid angle of the electron beam to a minimum.

There are several advantages with this system. The electron beam current is well controlled to prevent fluctuations in I_{EBIC} . Also there is sufficient flexibility in controlling the linescan such that an induced current can be measured specifically for a given time for a digitally known location. This results in greater accuracy than for a continuous linescan since a negligible response time for the specimen (which is not always valid) is necessary for accuracy in a continuous line scan. In a digital mode however, the data is taken in discrete steps, with a dead period provided after each movement of the electron beam to allow the measurement system to settle. Accuracy, repeatability, and throughput are clearly improved significantly.

Software

The software is based on the Tracor Northern system and is written in the Flextron⁷³ computer language. Fig. 5.4 is a flow chart of the EBIC program. Appendix I is a list of terms and definitions.

When EBIC is executed, variable space is allocated, utility libraries⁷³ are loaded, and the program prompts with "EBIC". It then waits for a command entry.

A detailed description of the commands available in the EBIC program is given in Appendix II, including the function, form and an example of each command. The function of each program block is described in Appendix III. The program has been developed to be completely interactive in nature, requiring the operator only to answer questions and follow single instructions (such as checking range setting on current amplifier). The major command in the program is the EBIC command. With this command, the operator controls the data acquisition, including positioning of the beam and reading of the data, data storage and data display or output. Also included in the EBIC command are least squares line fitting routines for data reduction. Other commands in the program are either support functions for the EBIC command, or are commands which allow the execution of a selection portion of the program which is normally a part of the EBIC command. The commands "CALIBRATE," "CLOCK," "DEFINE," "DELETE," "GET," "LIST," "LOAD," AND "SHIFT" are used as preliminary, set-up commands for the "EBIC" command. The commands

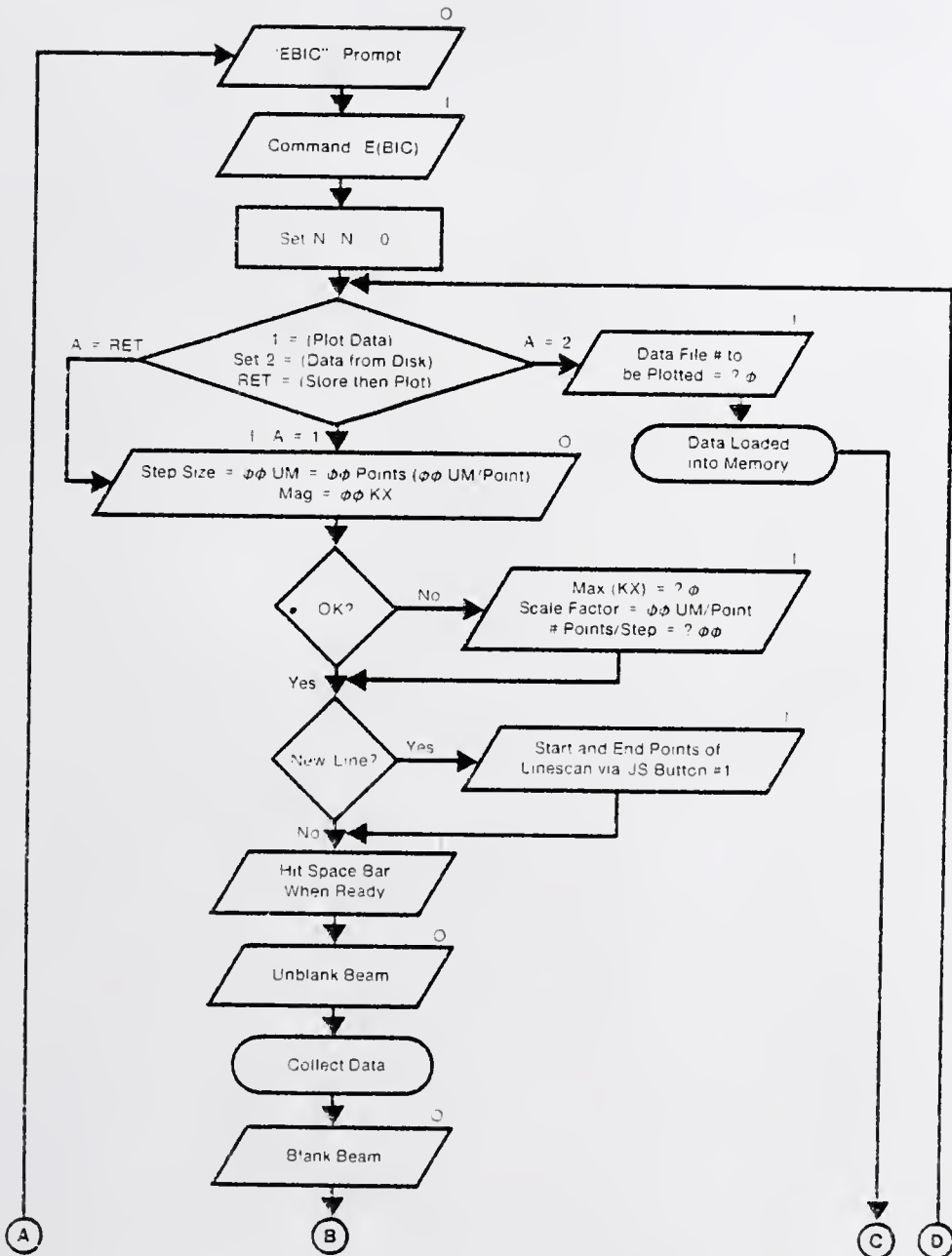


Figure 5.4(a) Simplified flow chart of the Flextran software used for EBIC automation.

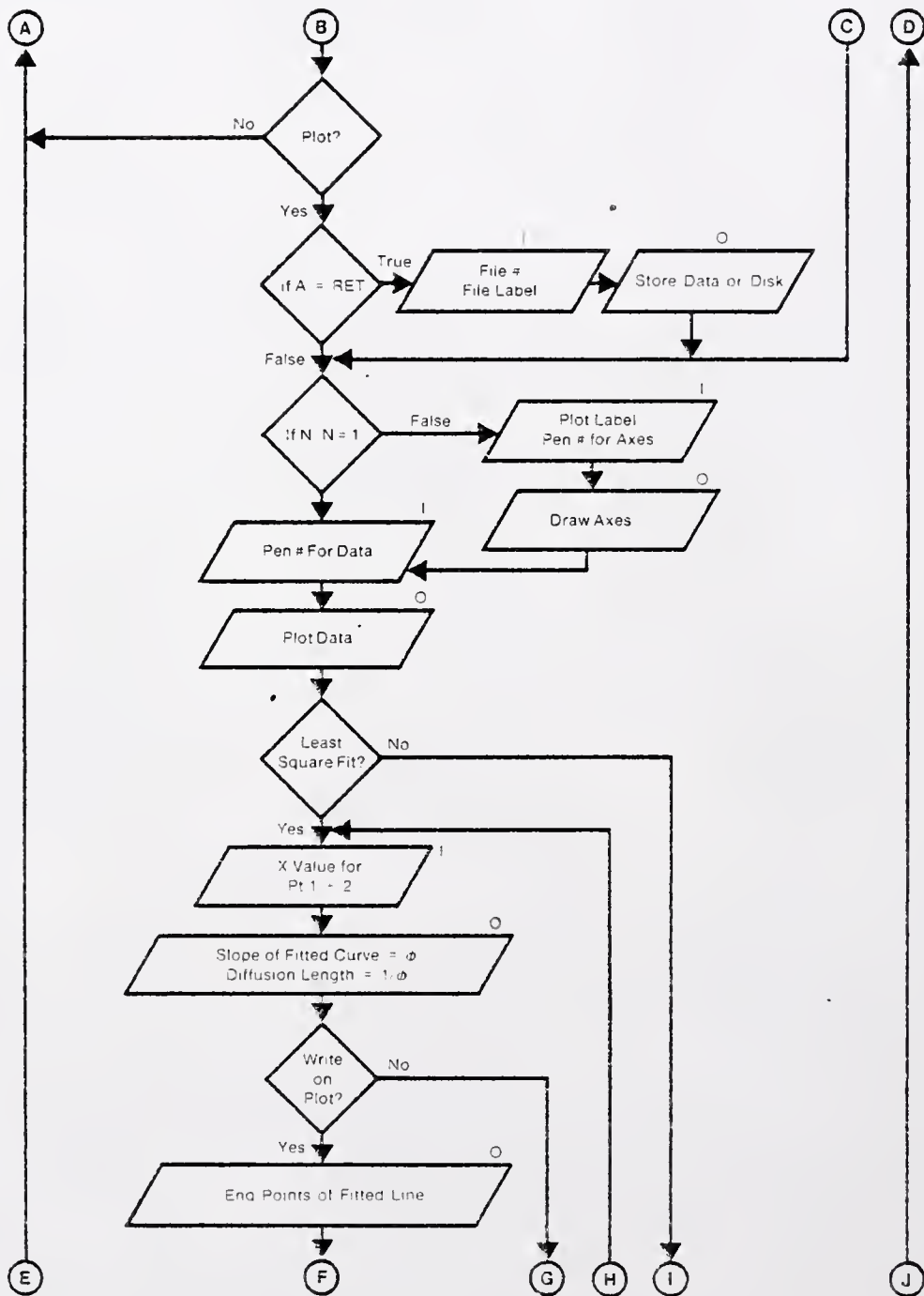


Figure 5.4(b) Continuation of EBIC flow chart.

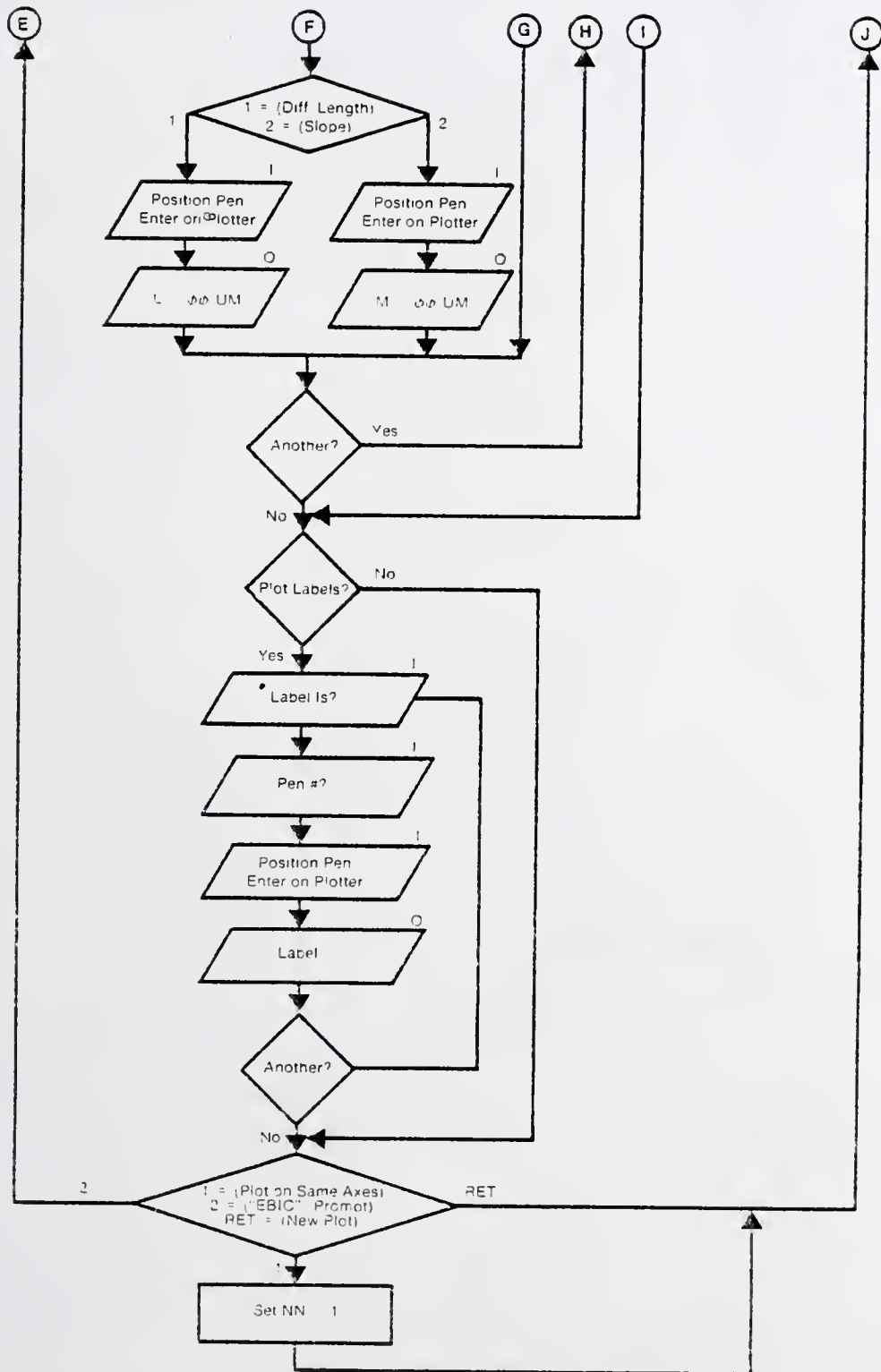


Figure 5.4(c) Continuation of EBIC flow chart.

"BLANK," "CUP," "LABEL," "POSITION," "SET," "TIME" and "UNBLANK" allow execution of a selected routine. A "SAVE" command allows the operator to save or re-save on disk either a table of stage positions or the EBIC program itself. This is very useful when making changes to the EBIC program. A "MANUAL" command is used to release the SEM or EPMA from computer control to allow complete manual operation.

The "EBIC" command initially allows the operator to set up all parameters necessary to acquire data in the form of an EBIC linescan. This format was chosen because of the fact that most quantitative EBIC models are based on the linescan, or EBIC versus beam position, data. The linescan is obtained from a region visible on the SEM screen in the normal SEM mode. Thus, the first input that the operator is asked to make is the working magnification. At a given magnification the program calculates the distance between digital beam coordinate points (of which there are 4096 across the SEM viewing screen) and reports this to the operator as "SCALE FACTOR", in units of microns per point. The operator then inputs the number of digital beam coordinate units to be included as one step in the EBIC linescan to be acquired. Once these parameters are set up, the operator simply defines a starting and stopping point within the field of view, via a joystick control, for the acquisition of the linescan.

The EBIC linescan data is then acquired, stored and plotted on the CRT or the digital plotter as desired. Plots can be requested in either a linear or logarithmic format. Labels can be added to the plot as desired, and least squares fitting routines can be applied to selected regions to deduce parameters of interest. Similarly, if it is desired

to examine, plot or manipulate previously stored on disk, the "EBIC" command can be utilized.

Extention of EBIC on MBX

There are some additions that have been made to the basic EBIC system to extend capabilities and convenience. Hardware and software extensions were needed for the additions.

Stage scan. In some instances it is desirable to maintain a normally incident beam to the sample at all times. This can be done by maintaining the beam in a constant position and scanning the sample stage with respect to the beam. The limitation here is that the stage can only be moved in one micron units and not less than one micron. This option is only applicable to systems for which stepping-motor driven stages are available.

Multiple line scans. It is possible to set up a number of linescans on one or several samples by defining all the stage and beam coordinates for desired linescan positions. EBIC then will consecutively perform the linescans and store the results on disk without human intervention. Upon completion, the tungsten filament would be turned off. The data is plotted later at a convenient time.

Wavelength dispersive x-ray spectroscopy (WDS) or energy dispersive x-ray spectroscopy (EDS) analysis. Acquisition of an EDS spectrum can currently be accomplished from EBIC by calling the appropriate Flex module. The '>' symbol preceeding a command means the command is a Flex module. Therefore, EDS acquisition can be performed from EBIC. This

can be setup in the multiple line scan mode to acquire an EDS during each linescan.

Analysis with WDS is most easily performed from 'TASK', an automated WDS analysis program (See Appendix I). From TASK, EBIC can be loaded into the auxiliary program area of TASK which allows any of the EBIC commands to be performed as well as any of the TASK commands. Care was taken to avoid any problems with conflicting variables when using EBIC as an auxiliary program in TASK.

Digital EBIC maps. With the aid of a computer, it is possible to measure and record the induced current with respect to specific digital beam coordinates over an entire raster scan. Using the Tracor Northern Spectra-Chrome 512 color monitor and Tracor Northern Image Processing Program package, up to eighty colors can be assigned to selected current value ranges for production of color induced current maps. This adds a more quantitative feature to the usual gray scale EBIC image. Either linear or logarithmic scales can be chosen for color display. Shown in Fig. 5.5 is a comparison of a normal black and white EBIC micrograph of a polycrystalline silicon solar cell with the corresponding color enhanced EBIC micrograph. Here red corresponds to the lowest level of EBIC signal, while white corresponds to the highest level. It is apparent that the subtle grey level distinctions of the black and white micrograph can be enhanced by color coding.



Figure 5.5(a) Digitally obtained color coded EBIC micrograph of a highly defected polycrystalline silicon diode. Central region of this micrograph is shown as a conventional black and white EBIC micrograph in Fig. 5.5(b).



Figure 5.5(b) Conventional black and white EBIC micrograph of the same area shown in Fig. 5.5(a).

Modifications of EBIC for JEOL JSM 35C SEM

The automated EBIC system has been modified to be used on a JEOL JSM 35C equipped with an identical Tracor Northern TN-2000 system. The modification mainly involved removing commands from EBIC which did not apply. The following features on the Cameca MBX were not available on the JEOL JSM 35C:

1. Stepping motor drive X, Y & Z stage, and
2. Computer controlled beam current regulation.

Because of these deficiencies, a few EBIC commands are not applicable. These were simply removed from the program for use on the JEOL system. A sample stage very similar to that developed for the Cameca system was developed and is shown in Fig. 5.6. This stage has the added advantage of ninety degree tilt capabilities.

Advantages of an EPMA Over an SEM for EBIC

After developing and using automated EBIC procedures on both a Cameca MBX electron probe and a JEOL JSM 35C SEM, several distinct advantages of the use of an EPMA system for EBIC work were realized. The basic design philosophy used for an EPMA system is centered around quantitative analysis, while for an SEM the design objectives are mainly qualitative except for magnification. Typically, EPMA systems are designed for higher beam current usage than SEMS and for a high degree of beam current stability. Modern EPMA systems, such as the Cameca MBX or the JEOL

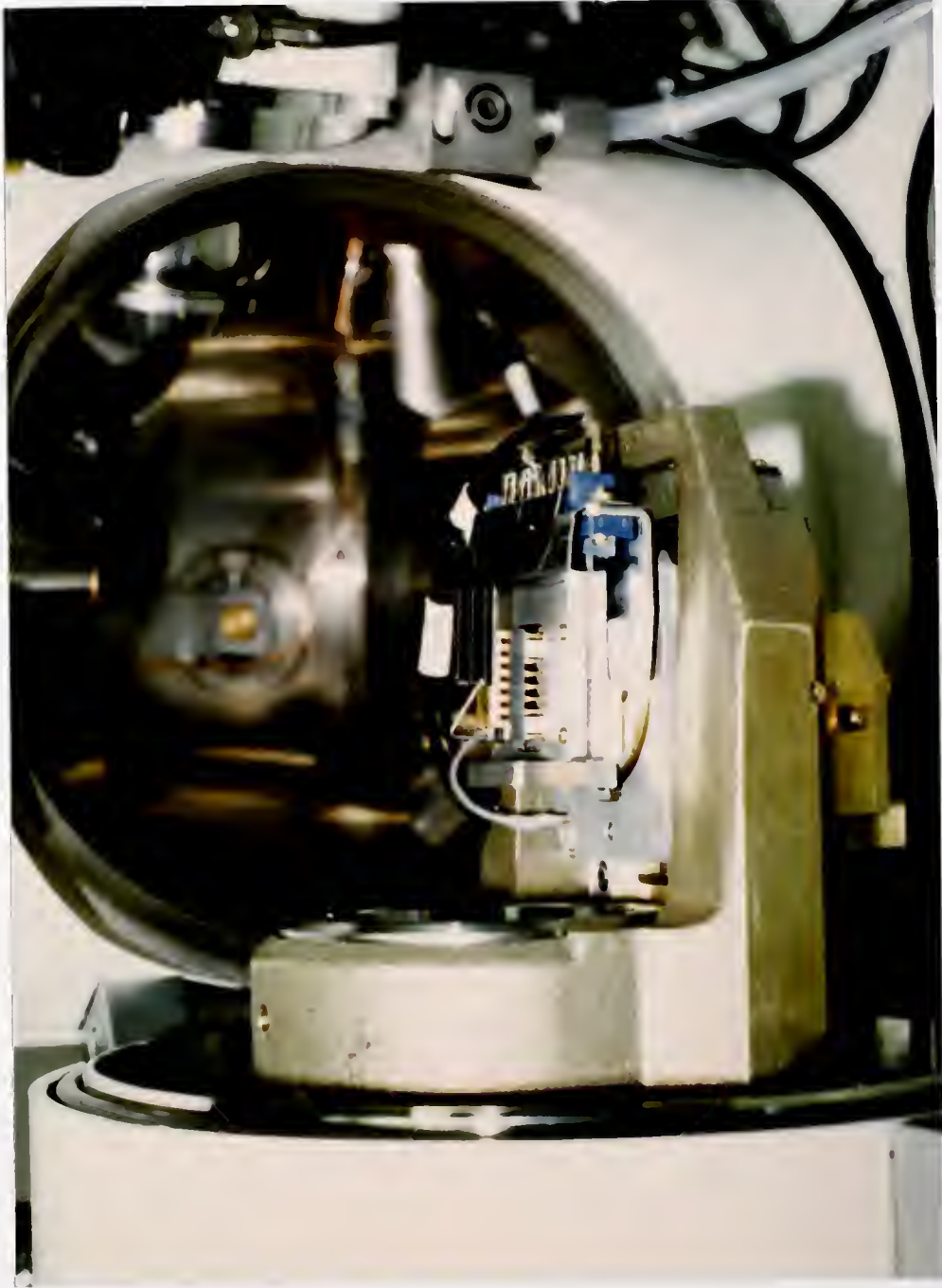


Figure 5.6 EBIC sample stage used in the JEOL JSM 35C scanning electron microscope. This stage allows for ninety degree tilt of the specimen.

733, are designed to serve as both an electron microprobe and a high resolution SEM. Thus essentially all features available on an SEM that are useful for EBIC work are also available on an EPMA; while in addition the EPMA offers other advantages.

The electron optics in an EPMA system are typically superior to those of an SEM. The lens power supplies are better regulated, the lenses are designed for a wider range of beam voltages and beam currents and beam current regulation and measurements systems are included as an integral part of the EPMA. The specimen stage of an EPMA is typically large and equipped with stepping motors for X, Y and Z motion. An automation system designed for automated x-ray analysis normally controls the beam current and stage motion, which are useful for EBIC work. Thus, many of the modifications needed to fully automate an SEM for EBIC work are included in an EPMA system and this warrants the preference of an EPMA as the starting system for EBIC work. The only real disadvantage of an EPMA is the higher cost of the system; however, this may be offset by the many modifications necessary to make an SEM quantitative and automated.

Applications

The system described is currently in routine use on both the Cameca MBX and JEOL JSM 35C systems at the Solar Energy Research Institute. The system has been used extensively for measurement of the electrical properties, especially grain boundary effective surface recombination velocity, of grain boundaries in polycrystalline silicon.^{12,21} Another common use involves fracturing finished devices and taking EBIC data on

the cross section. This has been applied, for example, to the study of the CuInSe_2 thin film solar cell,⁷⁴ the GaAs/indium-tin oxide (ITO) solar cell,⁷⁵ the InP/ITO solar cell,⁷⁶ and screen printed Si solar cells.⁷⁷ In general, the automated EBIC system is very versatile and aids in the measurement of many localized electrical effects in electronic devices and materials.

CHAPTER SIX

EXPERIMENTAL IMPORTANCE OF EBIC PARAMETERS

Introduction

Several parameters can easily be varied in a typical EBIC experiment. These include beam voltage, beam current and beam size. Also, data can be taken in either an analog or a digital mode. In the analog mode, the EBIC current is continuously monitored and the rate at which the electron beam is moved across the sample is an important parameter. In the digital mode, EBIC current is measured in discrete time units with the beam fixed. Thus, the spacing between data points and the time for each measurement are parameters of importance in the digital case. The vacuum system in which the EBIC measurements are taken introduces the parameters of type of pumping and pressure of vacuum. Sample temperature can also be an important parameter,⁷⁸ but will not be considered in this work since measurements could only be obtained with the sample at room temperature with the equipment utilized.

In this chapter, studies of the effect upon EBIC of each experimentally variable parameter are reported. Of particular concern are the effects on specific parameters such as effective diffusion length and grain boundary recombination velocity. Also to be considered are the possibilities of beam damage to the bulk or surface of the semiconductor and the build-up of contamination as a result of electron beam exposure in a non-ideal vacuum.

Reproducibility

A series of reproducibility tests were designed and conducted to test the effect of many of the parameters mentioned above. In the tests an EBIC linescan was recorded and the asymptotic slope of the dip at a grain boundary was calculated from these data. This is the measurement used to derive the grain boundary recombination velocity values reported in Chapter Eight. The objective was to determine the precision with which the slope could be obtained and then to determine the range of the various parameters over which the precision could be maintained.

Shown in Fig. 6.1 are four digitally acquired EBIC linescans across a grain boundary of a polycrystalline silicon MIS device (device structure will be described in detail in Chapter Eight). Each linescan was taken approximately one minute after the preceding linescan on the identical area, and with identical conditions. The linescans were plotted with a small offset added to aid in visually resolving the separate lines. For each case, the slope of the dip was measured over the same region and as shown identical values, measured to two significant digits, were obtained. Similar tests were repeated for various values of beam current (10-500pA) and voltage (10-45keV) using either a Keithley 480 picoammeter or a GW Electronics Type 103 absorbed current amplifier, and all tests yielded similar results. It was thus concluded that this measurement could readily be performed with a precision of one percent or less, based on results of these similar tests where three or more significant digits were recorded.

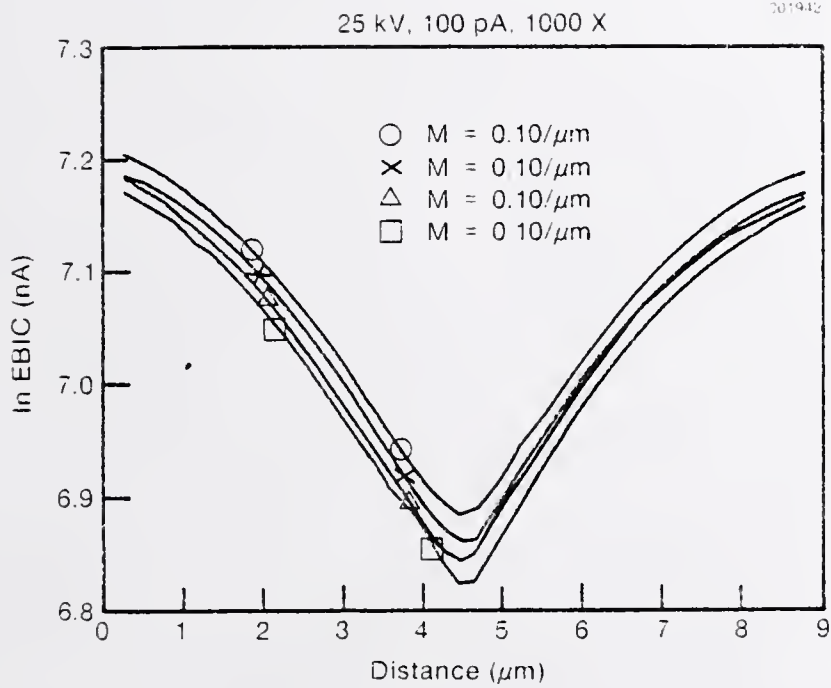


Figure 6.1 Four digitally acquired EBIC linescans across a single silicon grain boundary. Linescans were acquired sequentially, one minute apart. Values indicated are slopes of each linescan as the minimum is approached.

Useful Range of Beam Current and Voltage

Having established the fact that EBIC linescans can be obtained with reproducibility and precision of about one percent at typical beam current and voltage conditions (e.g. 50pA, 25keV) it was next desired to determine the upper limits of beam current and voltage for which such reproducibility could be maintained. Also the rate at which a beam could be scanned, or the amount of time a beam could be left in a fixed position, before beam damage occurred was investigated.

Tests such as that shown in Fig. 6.1 were repeated for incrementally higher values of beam current and beam voltage (separately). The onset of beam damage was defined as the point at which the reproducibility of four consecutive linescans became worse than two percent, as determined from the slope measurement. Fig. 6.2 shows a series of EBIC linescans, similar to those of Fig. 6.1 except taken with five times the beam current, where reproducibility is not maintained. An EBIC micrograph showing the damage in the form of distorted contrast at the grain boundary is shown in Fig. 6.3. The onset of damage as determined by viewing the EBIC image or by the linescan reproducibility test was found to be essentially identical. For a 25keV beam, beam currents of 400 picoamperes or less did not produce damage, whereas a 500 picoampere beam did. The damage criterion just described was obtained using a digital beam scan, where the dwell time for a beam position was 100 milliseconds and the distance between points was 0.19 micrometers. This dwell time was chosen as optimum for the system as a whole, including response time of the EBIC measurement system; i.e., this was found to be

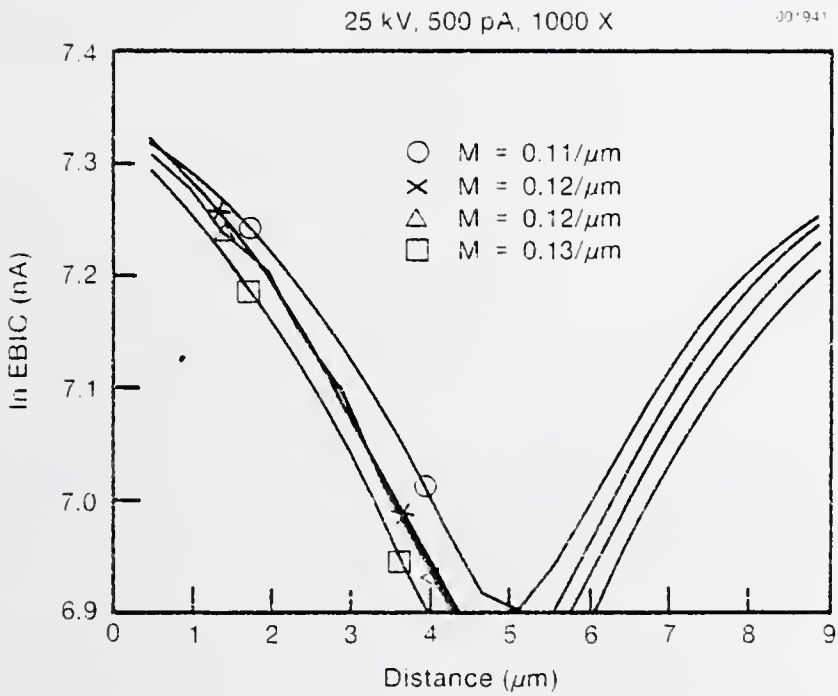


Figure. 6.2 Digitally acquired EBIC linescans, similar to those of Fig. 6.1, but taken with a beam current of 500 picoamperers. Beam voltage, dwell time and step size are the same as for Fig. 6.1.

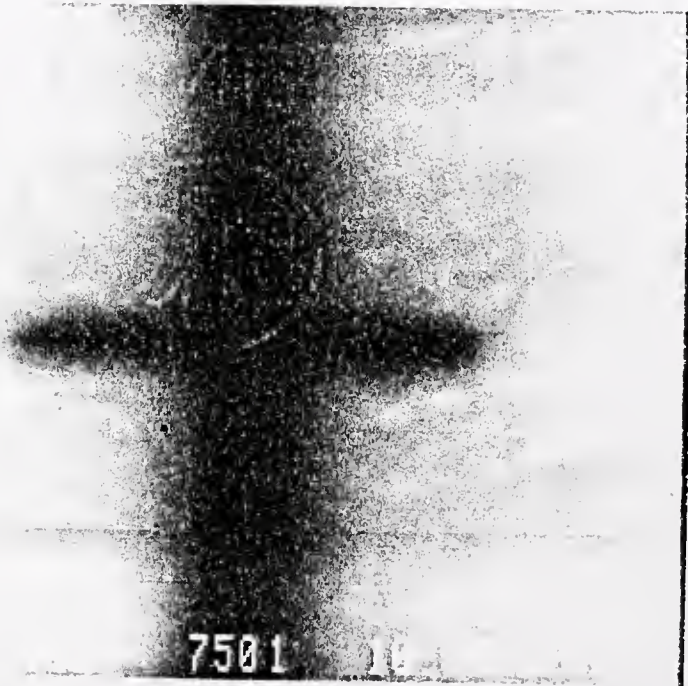


Figure 6.3 EBIC micrograph of a silicon grain boundary which has been damaged by long term exposure to high beam currents.

the shortest dwell time for which reproducible measurements could be obtained. The distance between points was chosen as the largest value which did not reduce the degree of reproducibility with which the slope could be obtained. Longer dwell times and/or shorter step size was found to increase the amount of beam damage for a given beam current and voltage, but did not lower the useful range of either for reproducible measurements.

Analog scans were found to produce less beam damage, as determined by observing the EBIC image, but reproducibility of slope measurements generally was no better than ten percent. Therefore, analog scans were not considered useful for any qualitative measurements.

A series of experiments were next designed and performed in which the effect of beam voltages (from fifteen to forty-five kilovolts) and beam currents (from ten to five hundred picoamperes) on measured values of asymptotic slope of I_{EBIC} as a function of distance to a grain boundary was investigated. The major purpose of these experiments was to determine over what range of these parameters measured values of grain boundary recombination velocity would be equivalent. The results of the experiments are summarized in graphical form in Figs. 6.4 and 6.5.

In Fig. 6.4, measured slope values are plotted as a function of primary electron beam voltage. Six separate plots are included, each representing a different fixed beam current, in the range of ten to five-hundred picoamperes. Data taken with beam voltages below fifteen kilovolts were omitted from the graph, as this data could not be obtained reproducibly. This was due partially to the fact that an

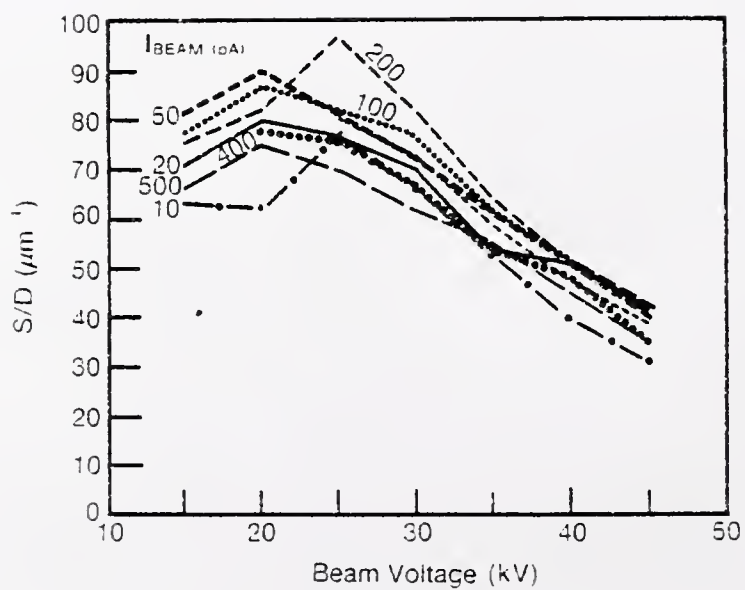


Figure 6.4 Asymptotic slope of EBIC linescan dip at grain boundary as a function of primary accelerating voltage.

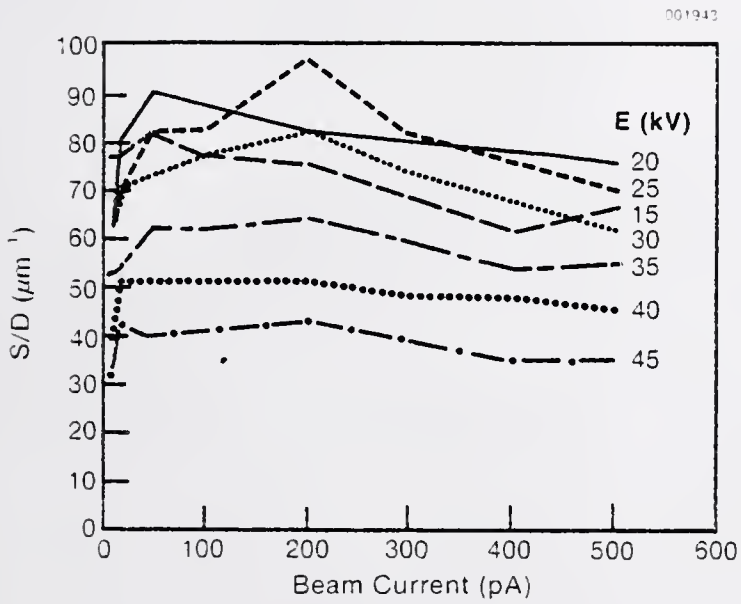


Figure 6.5. Asymptotic slope of EBIC linescan dip at a grain boundary plotted as a function of primary beam current.

aluminum metal layer had to be penetrated by the primary beam before carriers in the silicon were excited (see Chapter Eight) and partially to signal-to-noise problems in the electronics used to measure the low level EBIC signals. It was determined that only with time resolved EBIC techniques,⁷⁰⁻⁷² incorporating beam blanking and lock-in amplifier techniques, could the signal-to-noise limit be substantially improved. These techniques were developed to verify the ability to measure much lower EBIC signals, down to the low nanoampere range, but the work was only preliminary and will not be included as part of this thesis.

The results shown in Fig. 6.4 clearly indicate a strong dependence of the measured slope values on the primary acceleration voltage used. The values tend to have a maximum at twenty to twenty-five kilovolts, with a small decrease as the beam voltage decreases, and a large, fairly constant decrease with increasing beam voltage. The limits of the instrumentation used did not allow acquisition of data for beam voltages greater than forty-five kilovolts. The total spread of values obtained, in units of inverse micrometers, ranged from thirty to one hundred. For a given beam current value, the spread was as large as forty to one hundred. It is thus clear that if comparisons are desired for differences of less than a factor of two or three, the beam voltage must not be varied in the experiments. Also, since one of the major effects of changing beam voltage is the change of electron range, the thickness of any metal layer, such as the aluminum layer on the MIS devices of this study, should be equal or low enough to make any scattering by the metal layer insignificant for all samples for which intercomparisons are made.

The same data used for Fig. 6.4 are shown replotted in Fig. 6.5 in the form of measured slope values as a function of primary electron beam current. Here the six separate curves represent the six separate, fixed primary beam accelerating voltages used. It is clear from this plot that for beam currents above fifty picoamperes (up to the highest beam current used of five-hundred picoamperes) the measured slope values are fairly constant, with only a very small decrease with increasing beam current. The strong dependence on primary beam accelerating voltage is readily apparent in this plot as it was in Fig. 6.4. A trend of somewhat less dependence on beam current at higher beam voltages is also observed. It is felt that the change in slope of the curves at low beam current is at least partially due to the instability of the primary beam at these current levels, and to the difficulties of measuring the lower level EBIC signals obtained with the low beam currents. Also, the ability to accurately measure the beam current below fifty picoamperes with the system used is somewhat questionable.

For all measurements represented by Figs. 6.4 and 6.5, no beam damage was found to occur. This was verified by performing reproducibility tests such as those illustrated in Figs. 6.1 and 6.2 and by observation of the EBIC micrographs obtained before and after the series of measurements. Also no observable contamination was present after the measurements. All measurements were performed in a turbomolecular pumped vacuum system, with the sample chamber pressure in the low 10^{-7} Torr range. When similar measurements were performed in an oil diffusion pumped system with somewhat higher sample chamber pressure, considerable contamination was observed. Thus these experiments are only

possible in a relatively clean vacuum system. For an oil diffusion pumped system, the use of a liquid nitrogen cold finger anti-contamination plate was found to reduce the contamination rate to levels similar to that obtained in a turbomolecular pumped system.

Discussion

The ability to obtain reproducible EBIC linescan data across silicon grain boundaries has been demonstrated. However, limitations as to the useful range of primary electron beam voltage and current were observed. The useful beam voltage range is limited on the low end by the scattering of the beam by any coatings, such as the metal in an MIS device, covering the active semiconductor. The low end is also limited, along with the beam current, by the requirement of a large enough induced current to provide adequate signal-to-noise ratio (>1) in the measurement. This limitation can be reduced with the addition of beam blanking and lock-in amplification techniques, which decrease the noise level.

The upper limit on beam voltage is an instrumental limit, as most SEM's or EPMA's are limited to fifty keV or less. The upper limit on beam current is affected by the level of vacuum (to avoid contamination) and device stability.

It was shown that if the asymptotic slope of EBIC grain boundary linescans are to be used for comparative grain boundary recombination velocity studies, all analysis must be taken with the same primary beam voltage. The calculated velocity will be greatest, for the MIS device used in this work, when a beam voltage of twenty to twenty-five keV is

used. At lower beam voltages, recombination at the sample surface, which is ignored in the analysis (hence the use of the effective designation in $S_{\text{eff}}^{\text{gb}}$), more strongly influences the EBIC signal. At higher voltages the point generation source approximation becomes less valid. The technique for measuring $S_{\text{eff}}^{\text{gb}}$ was not found to be strongly affected by primary beam current for values between 50pA and 500pA; which defines a useful working range. This indicates that high injection conditions are not reached in this beam current range, since a change from low to high injection conditions would be expected to result in a large change in EBIC data. Beam damage, either in the form of rapid contamination buildup or alteration of interfacial regions of a device, was found to occur commonly for beam currents above 500pA. This damage is due either to a buildup of contamination on the sample surface or to chemical changes or charging, occurring at the Si/SiO_x or SiO_x/Al interface or in the oxide layer. In most cases examined in this work, charging of the oxide layer is believed to cause the damage, as evidenced by the ability of the sample to recover from the damage with time.

Based on the large dependence of calculated S_{gb} values on beam voltage, as shown in Fig. 6.4, and the fact that the model used assumes no dependence of S_{gb} on beam voltage, the accuracy of S_{gb} measured in this way must be considered as no more than a factor of two. There are two factors which affect the general shape of the curves in Fig. 6.4. These are the increase in average distance of carrier generation from the sample surface and the increase in diameter of the carrier generation volume with increasing beam voltage. The increase in generation volume causes an increase in measured S values since this increase allows for some of the carrier generation to exist at and beyond the

recombination plane (the grain boundary). This causes the increase in S for beam voltages up to 20 or 25 keV. At these voltages, however, the presence of top surface, with its finite recombination velocity, serves to decrease the measured EBIC current and hence give higher values for S_{gb} . As the beam voltage is increased beyond 25 keV, the generation volume is displaced further from the sample surface and hence a more realistic value of S_{gb} is approached at higher beam voltages. Thus, to minimize these artifacts, a beam voltage of 45 keV is used in the studies to be described in Chapter Eight.

While there is uncertainty in the absolute accuracy of the S_{gb} values obtained using 45 kV excitation, the values will be valid for comparative purposes. The data in Fig. 6.5 show that values of beam currents from 20 to 500 picoamperes can be utilized for beam voltages of 45 keV without influencing the measured S_{gb} values more than a few percent. As mentioned earlier, this clearly indicates that the condition of low carrier injection level is maintained over these values of beam currents. The upper limit of useful beam current as determined by the onset of beam damage effectively prevents the problem of high injection conditions occurring.

CHAPTER SEVEN

GRAIN STRUCTURE AND GRAIN BOUNDARY EFFECTS

Introduction

In this chapter, studies related to grain size and grain structure of cast polycrystalline silicon will be presented. Optical microscopy of etched samples forms the basis of the studies, with scanning electron microscopy used to provide supporting data. Further, EBIC techniques are used to determine electrical response of grain boundaries and twin boundaries. Both EBIC and optical microscopy techniques are used to study the junction structure of diffused p-n junctions at and near grain boundaries.

Grain Structure

To enable the study of the grain structure of cast polycrystalline silicon, as received wafers were chemically etched to reveal the grain and twin boundaries. The most successful etch was found to be a 6:1:1 mixture of hydrofluoric, acetic and nitric acids. This etch is strongly affected by crystallographic orientation and thus results in strong surface delineation of the grain structure.

The grain structure of the cast Wacker Silso polysilicon is found to be strongly influenced by the casting process itself.⁶⁷⁻⁶⁹ The process results in three distinct regions of differing grain structure in a typical wafer sliced from a cast ingot. These regions are shown schematically in Fig. 7.1. Region A, from adjacent to the mold wall, is composed of randomly oriented small grains nucleated due to the presence

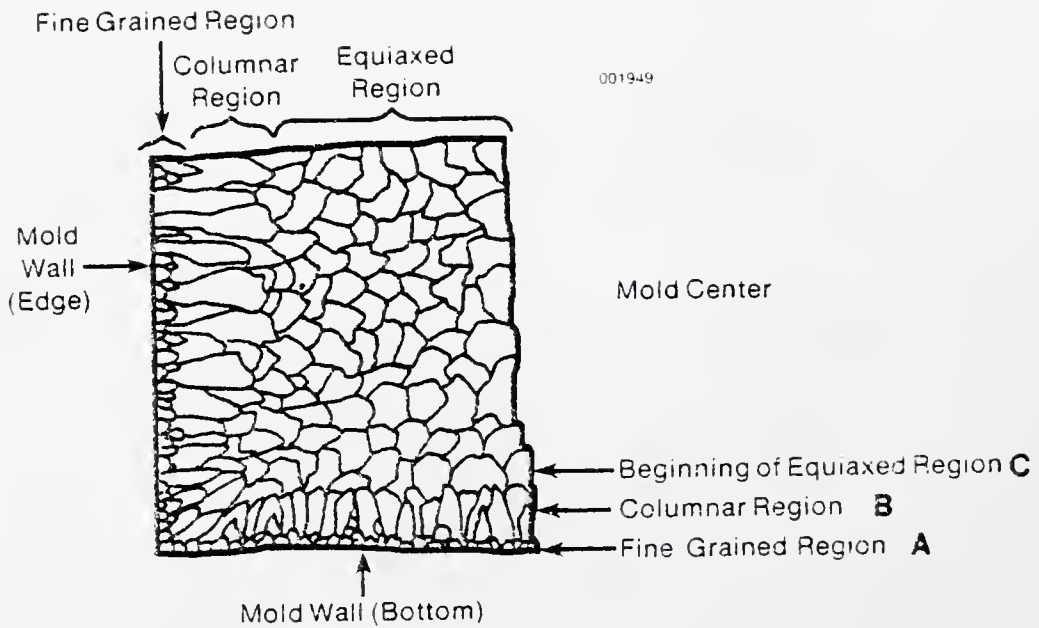


Figure 7.1 Schematic drawing of typical grain structure of a wafer sawn from a cast polycrystalline silicon ingot.

of the heat sink, i.e., the mold wall. As these grains are randomly composed of randomly oriented small grains nucleated due to the presence of the heat sink, i.e., the mold wall. As these grains are randomly oriented, some will naturally exist with the direction of maximum growth perpendicular to the mold wall. Lateral growth is limited by the space available between neighboring nucleation sites, however crystals growing fastest perpendicular to the wall will also grow laterally when they have passed the neighboring grains. This will block further growth of the slower growing crystals and result in the thin region of fine grains near the mold wall.

In region B, each grain has the axis of fastest growth roughly perpendicular to the mold wall, and all grains have grown at roughly equivalent rates. Thus, after the smaller grains are blocked from further growth, a columnar structure perpendicular to the mold wall extends inward towards the center of the casting. During the growth of this columnar structure, the liquid in the center of the casting undercools enough to cause nucleation of (randomly oriented) grains. These grains, of Region C, stop the growth of the columnar region and form an equiaxed grain region comprising the bulk of the casting. The average grain size in this equiaxed region varied slightly from casting to casting but remained in the range of one to two millimeters.

The bottom of the casting had a grain structure very similar to that near the mold wall since the mold bottom is thermodynamically very similar to the mold walls. This is shown schematically in Fig. 7.1. No samples could be obtained from the top of the casting. The grain structure of the central region (i.e. more than a few centimeters from any

edge) of all castings examined consisted of roughly equiaxed grains.

The line intercept count method was used for grain size measurements.⁷⁹ On a typical wafer, taken from a central region of a casting, grain size measurements were made with twin boundaries included. The results of 49 sample points using a 1.16 millimeter intercept line were: mean number of intercepts = 2.02, standard deviation = 1.27; resulting in a grain size of 1.14 ± 0.44 millimeter. The measurement was then repeated, excluding twin boundaries, and the analysis of 57 sample points using a 4.3 millimeter intercept line resulted in a grain size of 1.53 ± 0.38 millimeters. This difference indicates the presence of a large number of twins in this material. The twin-free measurement was repeated on another wafer from the same casting, using 68 sample points and a 3.7 millimeter intercept line and a grain size of 1.63 ± 0.45 millimeters was obtained. Visual examination of 1000 wafers, taken from ten different castings with 100 wafers per casting, revealed very similar grain size (i.e. between 1 and 2 millimeters) and grain structure in all cases.

The above observations on grain structure indicate that the true columnar grain structure, often used for modeling of polycrystalline devices, is obtained only if slices are taken parallel to the mold wall and in a very limited region. The grains of Region C, however, are large enough to somewhat approximate columnar structure in wafers much less than one millimeter thick. These grains are not columnar in a true sense and intersect the surface (and hence the collecting junction) at a wide range of angles, which cannot be properly modeled as perpendicular to the junction.

Actual optical micrographs of the above described grain structure are shown in Figs. 7.2 through 7.5. Regions A and B are shown in Fig. 7.2, which is a montage of many micrographs used to show the transition from fine grain size to elongated or columnar grains. Fig. 7.3 is indicative of the equiaxed grain structure of Region C, well away from the mold wall. A cross-sectional micrograph of the region shown in Fig. 7.2 is shown in Fig. 7.4, again clearly showing the transition from fine grains near the mold wall to elongated grains grown in a direction perpendicular to the mold wall. Fig. 7.5 shows a cross-section from Region C. This particular cross section was taken from a wafer cut from near a corner of the casting thus showing a preferential inclination of the grain boundaries. Wafers from central regions did not contain preferentially inclined grain boundaries.

An EBIC micrograph, shown in Fig. 7.6 verifies that the grain structure defined by electrically active grain boundaries, i.e. grain boundaries which exhibit high carrier recombination, is identical to that revealed by optical microscopy. All regions, (A, B, and C) can be seen in the EBIC micrograph. This observation has been verified for many samples thus indicating that in general the electrically defined grain size and structure are very similar to those defined by etching and optical microscopy. The major difference noted in the EBIC case is the absence of any twin boundary delineation, and the absence of a small number of grain boundaries that are visible optically. Fig. 7.7 shows complementary EBIC and optical micrographs which illustrate the absence of EBIC contrast at twin boundaries and at a small number of grain boundaries. Measurements of grain boundary length visible in both cases

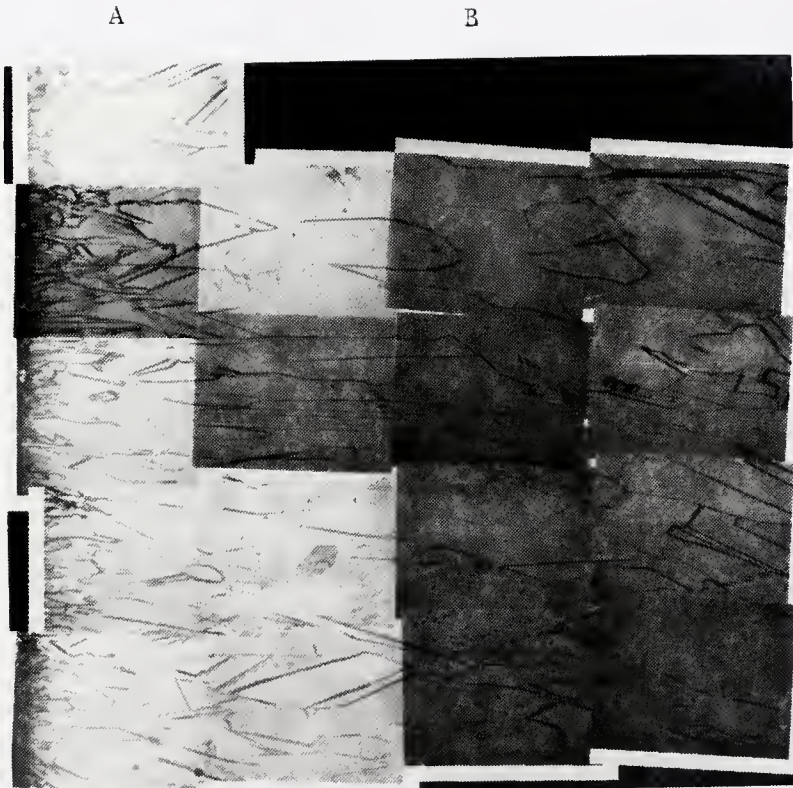


Figure 7.2 Montage of optical micrographs of an etched polycrystalline silicon wafer showing region from near the mold wall.



Figure 7.3 Optical micrograph of an etched polycrystalline silicon wafer showing a typical region from well away from mold walls.



Figure 7.4 Cross-sectional optical micrograph of an etched polycrystalline silicon wafer, showing the same region as shown in Figure 7.2.



Figure 7.5 Cross-sectional optical micrograph of an etched polycrystalline silicon wafer showing a section well away from mold walls. Angular orientation of grains is due to position near bottom of casting.



Figure 7.6 EBIC micrograph of polycrystalline silicon device showing three distinct grain structure regions as described in text.

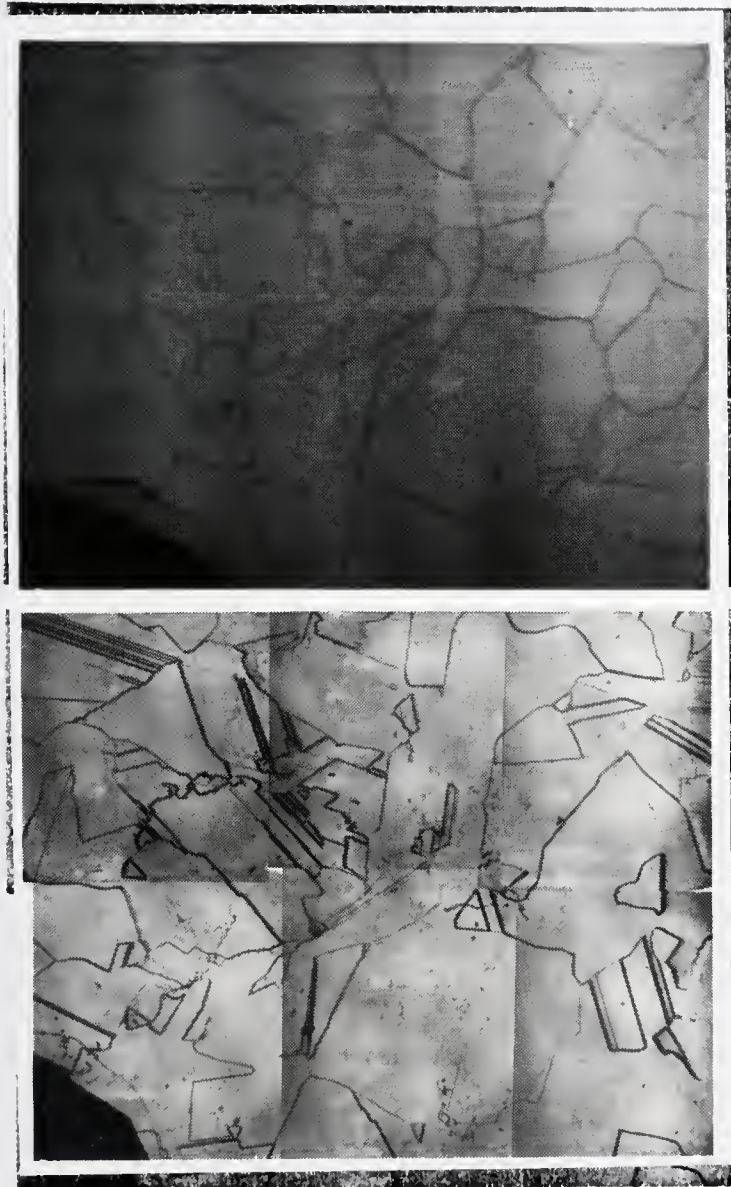


Figure 7.7 Complementary EBIC (top) and secondary electron (bottom) micrographs of the same region of a polycrystalline silicon device, showing the absence of EBIC contrast at twin boundaries and at a few grain boundaries.

were made and approximately 90% of the optically visible grain boundaries were visible in the EBIC micrograph. This was measured quantitatively for over 130 millimeters of grain boundary length for a test wafer, and verified qualitatively for more than thirty other wafers. In most cases, even the grain boundaries not initially visible in EBIC micrographs could be imaged in the EBIC mode if amplification was increased, indicating that these grain boundaries act as weak recombination sites as compared to the typical grain boundary.

Uniformity of Grain Boundary Response

More than three hundred silicon grain boundaries have been examined via EBIC techniques in this study. The most commonly observed grain boundary in the case of a diffused p-n junction diode exhibited strong, uniform recombination as judged from uniform EBIC contrast along its length. Some grain boundaries, however, exhibit very dramatic EBIC contrast changes along their length. An EBIC micrograph of such a grain boundary is shown in Fig. 7.8. Close inspection of the micrograph reveals the intersection of twin boundaries with the grain boundary precisely at the point of discontinuity of EBIC contrast. Where the grain boundary is actually formed by two grains of identical relative orientation (with respect to one another) the EBIC contrast is similar. An abrupt change of orientation such as a twin plane can drastically change the EBIC contrast (and thus the recombination velocity) at the grain boundary. All twin boundaries observed exhibit

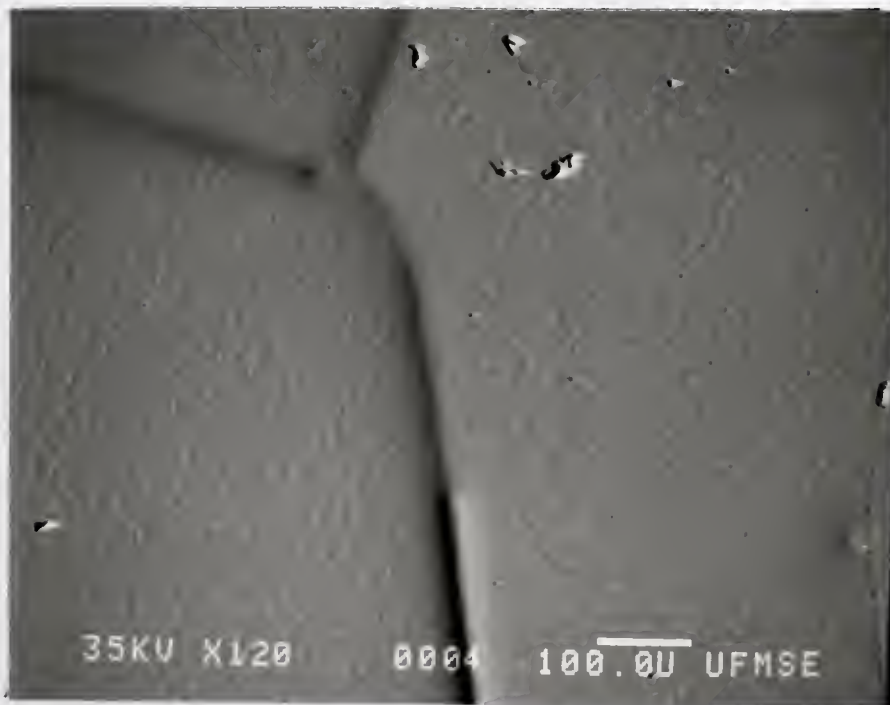


Figure 7.8 EBIC micrograph of a polycrystalline silicon device showing dramatic EBIC contrast changes along a grain boundary.

only very weak or no EBIC contrast, thus indicating extremely low twin boundary recombination velocities. This is illustrated in Fig. 7.9 which shows complementary secondary electron and EBIC micrographs of a twin boundary and a grain boundary, and an EBIC linescan (linear scale) across both.

To examine the grain boundary recombination properties beneath the sample surface, and below the junction depth, p-n junction devices were fractured and examined in the SEM in both secondary and EBIC modes. The samples were examined in a tilted position (30° to normal) to allow for observation of grain boundaries on the sample surface and on the fracture surface simultaneously. Examples of such complementary secondary and EBIC micrographs are shown in Fig. 7.10. From Fig. 7.10, it is obvious that grain boundaries which exhibit strong recombination contrast on the surface of a device exhibit similar effects beneath the surface. Twin boundaries which do not show recombination effects on the device surface similarly do not show recombination effects beneath the junction. Thus it is concluded that an EBIC recombination map of a device surface is representative of the recombination properties of grain boundaries even at depths beyond the range of the carrier generation for the primary electron beam.

P-N Junction Structure at Grain Boundaries

Complementary staining and EBIC techniques were used to examine the influence of grain boundaries on the structure of a diffused p-n junction. It is well known that diffusion at grain boundaries occurs more rapidly than diffusion in the bulk for many materials. Queisser

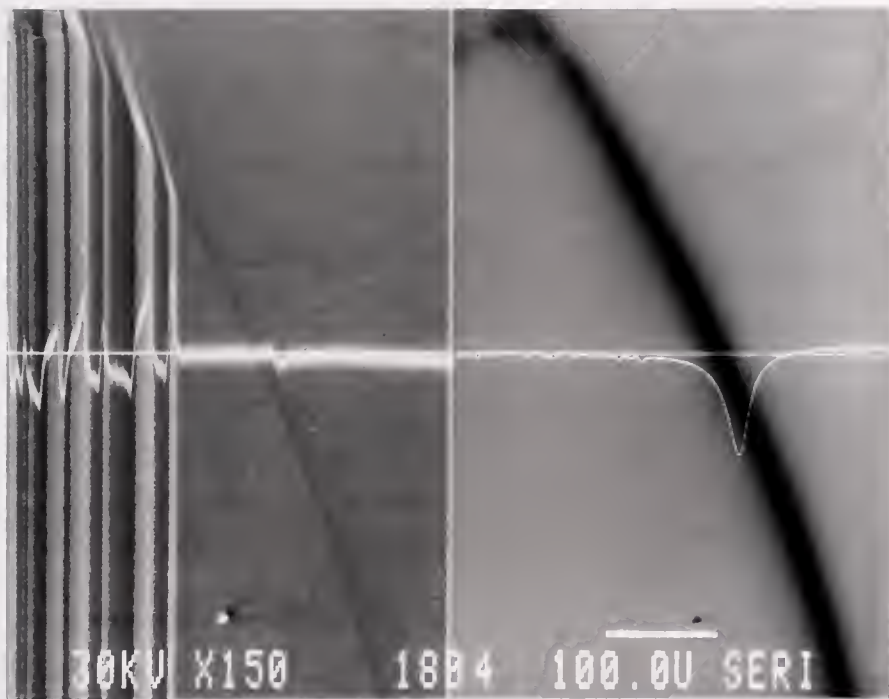


Figure 7.9 Complementary secondary electron (left) and EBIC (right) micrographs, with EBIC linescan (linear scale) superimposed on the EBIC micrograph illustrating the dramatic differences in the recombination velocity of grain boundaries versus twin boundaries.

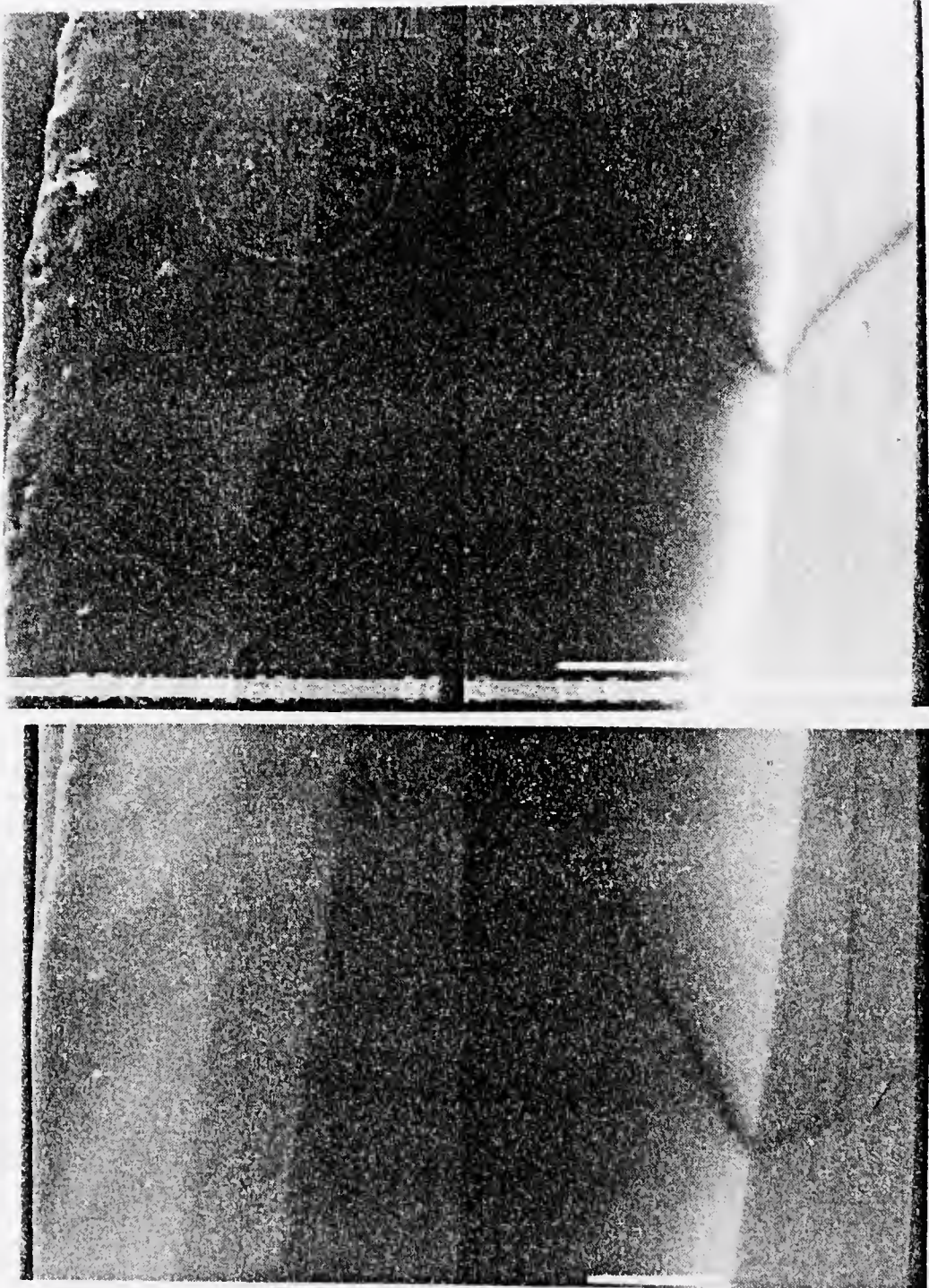


Figure 7.10 Complementary secondary and EBIC micrographs of fracture p-n junction diodes showing recombination properties beneath the sample surface. Note the twin boundaries in the top of (a).

et al.⁸⁰ have studied this phenomenon for the case of phosphorus in silicon low angle grain boundaries and reported that the diffusion along such grain boundaries may be of the order of 10^5 times faster than bulk diffusion at 900°C.

Staining techniques are well established and routinely used for p-n junction depth measurements.⁸¹ The technique is based on the preferential staining by chemical means of different conductivity type silicon regions. To enable one to accurately measure typical junction depths (one tenth to a few microns) with standard optical microscopes, grooving or beveling techniques are used. These techniques use angle-lapping the surface at a small, well known angle to the sample surface which allows one to measure a distance from the bevel edge to the junction location, and then to simply calculate the corresponding junction depth from the original surface.

Diffused p-n junctions were fabricated by first growing a phosphorus glass on a clean polysilicon wafer at 900°C and then heating the glass coated wafers of 1040°C for periods of one half to one hour. The bulk diffusion of phosphorus in single crystal silicon under these conditions results in a p-n junction depth of approximately one and one-half to two microns. The samples were then grooved or beveled and stained, and examined with optical microscopy. Spikes in the junction profile at some, but not all, grain boundaries were observed. No spikes were observed at twin boundaries. The depth of the grain boundary spikes was found to vary from one boundary to another up to a maximum depth of about five times the junction depth.

It is important to realize that the depths of spikes observed with the bevel and stain technique do not indicate the maximum depth of grain boundary diffusion. The technique reveals an isoconcentration boundary where the donor density is proportional to the acceptor density,⁸² and as such gives no indication of grain boundary diffusion resulting in concentrations much less than the base doping.

The width of the p-n junctions formed along grain boundaries was consistently found to be approximately 5 microns, while the depth varied from undetectable to as high as ten microns. The observed spikes taper down in width to about 1 micron, after which they become undetectable, or actually end. The two techniques used, however, have a maximum resolution of approximately one micron so any junction (i.e., diffusion spike) of lesser width would probably be undetected. A p-n junction spike at grain boundaries would have several effects on the electrical properties of a polysilicon diode (or solar cell). For example, the increase in total junction area of the device would cause an increase in capacitance when compared to a single crystal device of the same size. This effect has been experimentally verified.⁸³

The EBIC technique has been used to verify the results of the bevel and stain studies. The sample configuration was based on that of Hackett⁶⁰ and is shown schematically in Fig. 7.11. Samples were first beveled and stained to show the isoconcentration boundary previously described. The results of these stainings were recorded for reference. Front and back contacts were then attached as shown in Fig. 7.11 and the samples were examined in the EBIC mode. EBIC micrographs of such beveled samples are shown in Fig. 7.12. While staining did not

001940

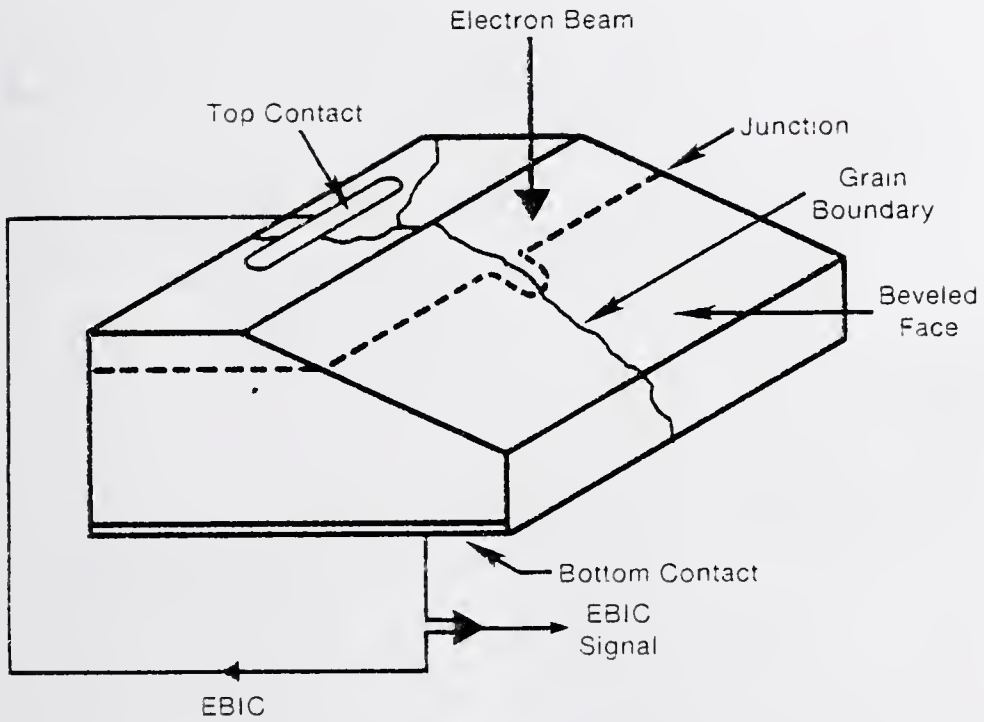


Figure 7.11 Schematic of beveled EBIC sample configuration.

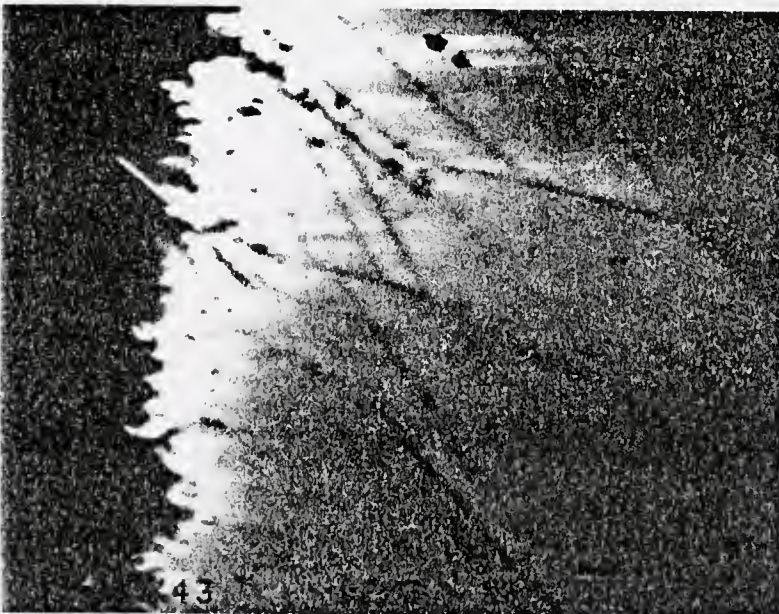


Fig. 7.12 EBIC micrographs of beveled p-n junction diodes showing enhanced grain boundary diffusion.

reveal junction spikes at all grain boundaries, EBIC analysis revealed electrical evidence of diffusion spikes at almost all grain boundaries. After heat treating at 1040°C for 40 minutes, the junction in the middle of the grains was $\sim 6 \mu\text{m}$ at the grain boundary. This is an average value and was observed to vary $\pm 50\%$. Examination with either EBIC or with staining produced similar results for distance of preferential penetration along the grain boundaries. However, not all of the grain boundaries could be decorated by staining, but most exhibited electrical activity with EBIC analysis. (This is a general observation, but not quantified.) In samples heat treated for one hour at 1050°C, the preferential penetration along the boundary was $\sim 11 \mu\text{m}$.

Based on these experimental data, Holloway⁸⁴ has recently calculated the ratio of grain boundary to bulk diffusion coefficient (D' to D) of phosphorus in silicon for the conditions defined above. He approximated the silicon substrate as semi-infinite and used the results of Whipple⁸⁵ and LeClaire⁸⁶ for his calculations. The ratio of D' to D was calculated to be approximately 5×10^3 from the 40 minute data and approximately 1×10^4 from the 1 hour data. Thus, the grain boundary diffusion coefficient for phosphorous in Wacker polycrystalline silicon is approximately 3×10^3 larger at 1040°C than for bulk diffusion. Holloway⁸⁴ also illustrated the effects of grain boundary transport on various device processing cycles using the model of Suzuoka.⁸⁷

Discussion

The results described in this chapter clearly show that the grain structure of Wacker Silso polysilicon is controlled by the casting

process. Three distinct grain structure regions were identified: a fine grained region from near the mold walls, a columnar region extending perpendicular to the mold walls, and an equiaxed region comprising the bulk of the casting. This grain structure was found to be consistent in ten different castings by examination of 100 wafers from each casting. The grain size in the equiaxed region was found to be 1.63 ± 0.45 millimeters. A large number of twins were observed in all wafers.

EBIC data confirmed that the electrically active grain structure was very similar to the actual grain structure, with the exception that twin boundaries were not found to be electrically active. EBIC data also showed that grain boundary recombination was uniform along a grain boundary unless a change in orientation occurred. EBIC images of fractured samples revealed that an EBIC map of a device surface is representative of the recombination properties of grain boundaries through the wafer thickness.

P-N junction structures at grain boundaries were examined by staining and EBIC techniques. Preferential diffusion of phosphorus at silicon grain boundaries was observed for temperatures of 900°C and 1040°C . This results in p-n junction spikes at grain boundaries in solar cells or diodes fabricated by standard diffusion processes. Thus, any studies of the properties of grain boundaries in diffused junction polysilicon devices must take the preferential diffusion of phosphorus into consideration.

With the basic understanding of the grain structure and general chemical and electrical properties of silicon grain boundaries developed in this chapter, specific studies of the recombination properties of

grain boundaries in Wacker Silso were undertaken. These studies are described in detail in the following chapter.

CHAPTER EIGHT

THE EFFECT OF HEAT TREATMENT ON GRAIN BOUNDARY PROPERTIES IN CAST POLYCRYSTALLINE SILICON

Introduction

The effects of heat treatment at temperatures appropriate for solar cell device fabrication on grain boundaries in cast polycrystalline silicon have been studied. An MIS device structure using a 200°C heating was used for fabricating test devices on heat treated samples for EBIC studies. Grain boundary effective surface recombination velocities (S_{eff}^{gb}) and effective mid-grain diffusion lengths (L_{eff}) were measured using EBIC techniques described in Chapter Three. The effective recombination velocity of grain boundaries was found to increase after heat treatment. Segregation of oxygen to grain boundaries has been observed in heat treated samples.

Redfield first reported that grain boundaries in Wacker polysilicon were electrically inactive in the as-cast condition.^{88,89} He pointed out that virtually all existing studies on the electrical properties of grain boundaries were conducted on polysilicon that had received some sort of heat treatment as part of device fabrication. Redfield used the liquid crystal technique to examine pieces of polysilicon before and after heating to approximately 900°C. He observed virtually no grain boundary contrast on the unheated samples, but very strong contrast at most grain boundaries in the same sample after heating. The contrasts observed by this technique were found to correlate well with contrast due to electrically active grain boundaries as observed with a laser scanning system on a fabricated diode. While this observation was

qualitative at best, it did indicate that grain boundaries in as-cast Wacker polysilicon have some properties which are dependent on thermal history after casting. Redfield also reported that grain boundary transconductance, and hence grain boundary barrier height, increased dramatically after heating. In other studies, (e.g. Seager), the measured grain boundary barrier heights did not show similar dependence on thermal history.⁹⁰ It was observed, however, that Seager's data were taken primarily on grain boundaries from near the edge of the Wacker casting, whereas Redfield's data were all taken on grain boundaries well away from the edge of the casting. Also, the various wafers used were not from the same casting nor from the same region of different castings. This may account for differing thermal history and thus crystallographic differences as described in Chapter Seven and chemical differences, if temperature dependent processes such as segregation or diffusion are acting.

The purpose of this study was to determine the effects of heat treatment on the electrical properties of grain boundaries in cast polycrystalline silicon in a systematic manner, since previous reports on the effects of heat treatment had been conflicting.^{89,90} Samples were first heated then fabricated into devices at $T \leq 200^\circ\text{C}$ to allow investigation of both the effects of heat treatment on grain boundary recombination and the mechanisms causing the changes. Heat treatment temperatures which are appropriate to fabrication processes for polycrystalline silicon solar cells have been used. The effects of heating were measured with the electron beam induced current (EBIC) technique and by physical analysis of the grain boundary.

Experimental

In order to have control over the heat treatment schedule, both Schottky barrier and metal-insulator-semiconductor (MIS) rectifying contacts were studied. It was found that fabrication of true, reproducible Schottky barriers was very difficult due to the formation of the native oxide on the clean silicon surface. Since no technique for cleaning the silicon surface in a vacuum system suitable for metallization was available, an Al-SiO_x-Si (p-type) MIS structure was chosen for the present studies. This structure can be fabricated by heating to temperatures $\leq 200^{\circ}\text{C}$ in air to form an insulating oxide. Initially, MIS samples were produced by growing an oxide in boiling H₂O, but these devices were not as reproducible as desired. The problem is believed to be one of nonuniform oxide coverage and/or impurity incorporation into a hydrated silicon oxide layer; this was verified by SIMS profiles, such as shown later, showing H decoration at the interface. To improve the insulator quality, oxides formed in air by heating for ten minutes at 200°C, 300°C, and 400°C were studied. To show that ten minutes at these temperatures did not affect the electrical properties of grain boundaries, samples were first heat treated at 200°C to 400°C, any oxide was etched off, then an insulator layer was grown in boiling water for EBIC analysis. These samples were identical in EBIC response within experimental scatter to samples not receiving heat treatment. Data reported in the following were all taken on samples with oxides fabricated at 200°C in air.

Samples were initially heat treated in a tube furnace with flowing argon gas. Because EBIC data showed this caused a very high density of electrically active defects after heating, the data reported here (unless indicated otherwise) were taken from samples encapsulated in electronic grade quartz tubes, evacuated and back-filled with helium four times, and heated in the tube furnace. The samples were carefully pushed into and pulled out of the hot zone over periods of approximately three minutes to avoid thermal shocking.

Besides using the EBIC technique, effective bulk minority carrier diffusion lengths have been measured using homogeneous minority carrier generation by energetic x-rays.⁹¹ In this technique, the photocurrent from a calibrated single crystal silicon solar cell is compared to that from a polycrystalline solar cell when both are simultaneously exposed to a high flux of white x-rays with a cutoff energy of approximately 200 keV. This gives a uniform carrier generation rate, and after accounting for differences in the areas of the two cells, the average bulk diffusion length may be determined for the polycrystalline sample from the known value of the single crystal sample (assuming other properties, such as surface recombination velocity, are identical in the two cells).

The main electrical properties characterized in this study are recombination of minority carriers at grain boundaries and effective intragranular diffusion lengths. The effective grain boundary recombination velocity, S_{eff}^{gb} , was used to characterize localized recombination, and we have calculated this from EBIC data. For EBIC measurements of grain boundary recombination and diffusion lengths, the Cameca MBX electron microprobe system described in Chapters Three and Five was

used to study samples heat treated at 600°C, 750°C and 900°C for times of approximately 1/2 hour, 1 hour and 20 hours. Initial data was taken in a manual mode, which provided the driving force for the development of the automated EBIC system described in Chapter Five. All samples were fabricated from Wacker cast polycrystalline silicon (p-type, 1-10 Ω-cm). The half millimeter thick wafers were all from the same ingot and taken from a group of ten sequential 10 cm x 10 cm wafers, to minimize variables due to the casting process itself.

Changes in the magnitude of the EBIC response are commonly used as a qualitative indication of grain boundary recombination. As discussed in Chapter Three, if the electron beam is scanned across a grain boundary which is perpendicular to the surface, the change in EBIC as a function of distance from the grain boundary is related to $S_{\text{eff}}^{\text{gb}}$ by

$$\frac{\partial}{\partial z} \ln I_{\text{EBIC}} \Big|_{\lim z \rightarrow 0} = \frac{S_{\text{eff}}^{\text{gb}}}{D}$$

where carriers are being generated a distance z from the grain boundary, and D is the minority carrier diffusion coefficient. The major assumption made in deriving the above equation is that carriers are generated at a point source. Independent knowledge of the value of D is also required, and in the present case data from the literature⁹² has been used. The uncertainty in this value is of the order of $\pm 20\%$, based on the uncertainty in the local carrier concentration in the polysilicon used.

Results

The first problem encountered in this study was that of reproducibility creating, at low temperature, devices suitable for EBIC measurements. This obviously eliminates high temperature diffusion processes to create a p-n junction, and suggests either using ion-implantation for forming a homojunction, or forming an induced junction via a metal-semiconductor or metal-insulator-semiconductor (MIS) contact. Ion implantation typically requires a thermal anneal to activate the dopants, but Schottky barrier or MIS devices can be formed without high temperature thermal processing and therefore were the processes investigated. Furthermore, ohmic contacts were formed on the back, also at low temperatures.

The native oxide growth on a clean silicon sample gave problems in the fabrication of reproducible Schottky barrier devices. As the goal of this device processing was to fabricate the simplest, reproducible devices without high temperatures, it was decided to use the native oxide problem constructively for the fabrication of MIS devices. Initially fabrication was attempted using the so-called beaker oxide technique in which a cleaned Si wafer was immersed in boiling, deionized H₂O for oxide growth. An aluminum dot was thermally evaporated onto the beaker grown oxide to complete the MIS contact. The oxide on the back of the device was then etched off with 10% HF and the device immediately inserted into the vacuum evaporator for aluminum back contact deposition. Verification of the ohmic contact was achieved by simply placing a wire mask on the device during back contact evaporation and using a curve tracer to verify the ohmic path from one side of the aluminum

through the silicon, to the other aluminum pad. A curve-tracer was also used to verify the existence of a single rectifying junction in the finished device. Figure 8.1 shows the geometry of the finished device structure. Examples of I-V curves taken on beaker oxide samples are shown in Fig. 8.2; as shown results were not reproducibly obtainable. A SIMS analysis, using a cesium primary beam, was performed to determine the nature of the thin oxide layer. A depth profile is shown in Fig. 8.3. Contamination by Cl and H at the Si/SiO_x interface was detected. The levels of these impurities, as well as Na, were found to vary from sample to sample and correlated roughly with the device I-V characteristics (i.e., more contamination resulted in less ideal devices). It was thus concluded that the beaker oxide technique was non-reproducible due to difficulties in controlling ionic contaminants at the interfaces and in the oxide layer. In addition, analysis by EBIC showed that some grains exhibited a higher EBIC current than others within a given device. Such an EBIC micrograph is shown in Fig. 8.4. Subsequent SIMS analysis revealed that the grains with low EBIC response typically had a thinner, more heavily contaminated oxide layer than the grains with higher EBIC response. Thus the beaker oxide technique for MIS device fabrication was shown to be highly dependent on the crystallographic orientation of the silicon grains on which the oxide is grown.

To improve the quality and reproducibility of the MIS devices, the use of H₂O as the medium for oxide growth was eliminated and thermally grown oxides were investigated. The basic problem here, however, was to verify that any thermal processing of the devices during fabrication did not influence the electrical activity of grain boundaries. It was known

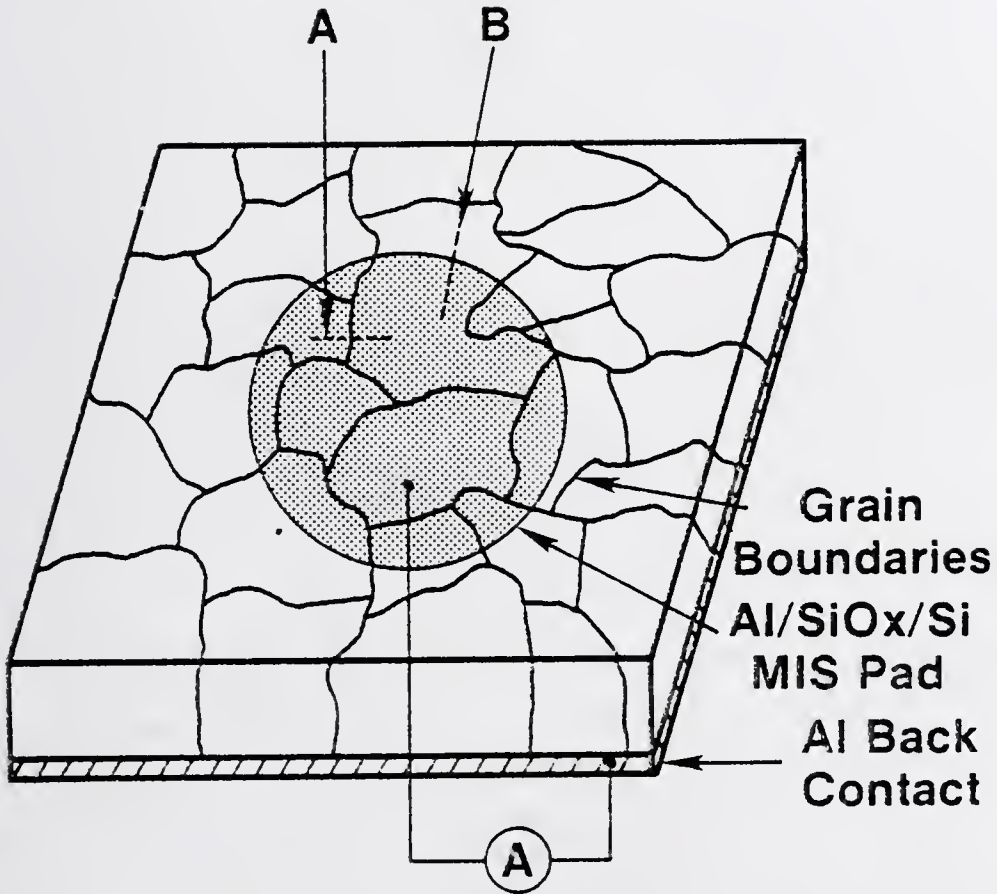
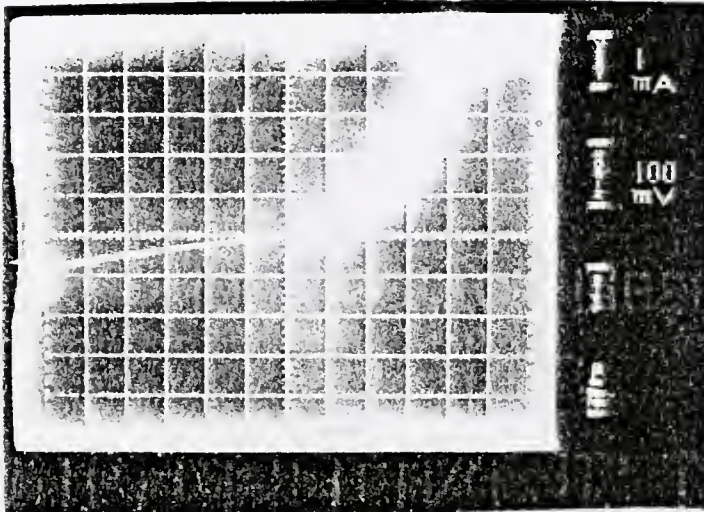
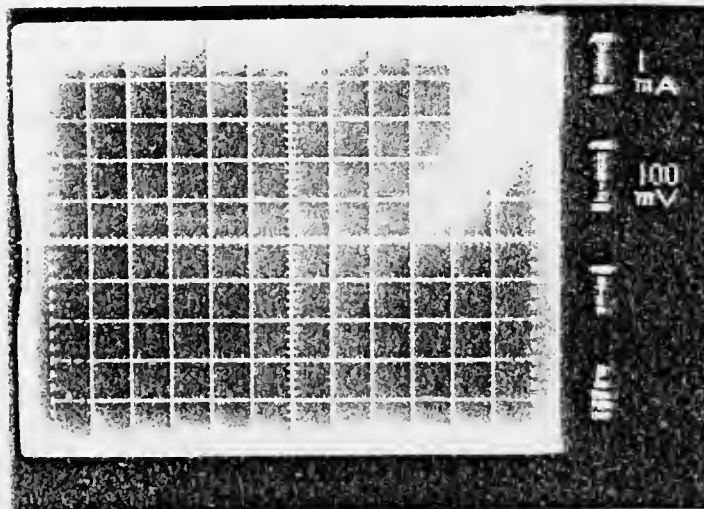


Figure 3.1 Schematic drawing of MIS device structure used for EBIC analysis. Position A used for S_{eff}^{gb} measurements and position B used for L_{eff} measurements.



(b)



(a)

Figure 3.2 Curve tracer I-V plots of MIS devices fabricated with the beaker oxide technique: (a) good device; (b) bad device.

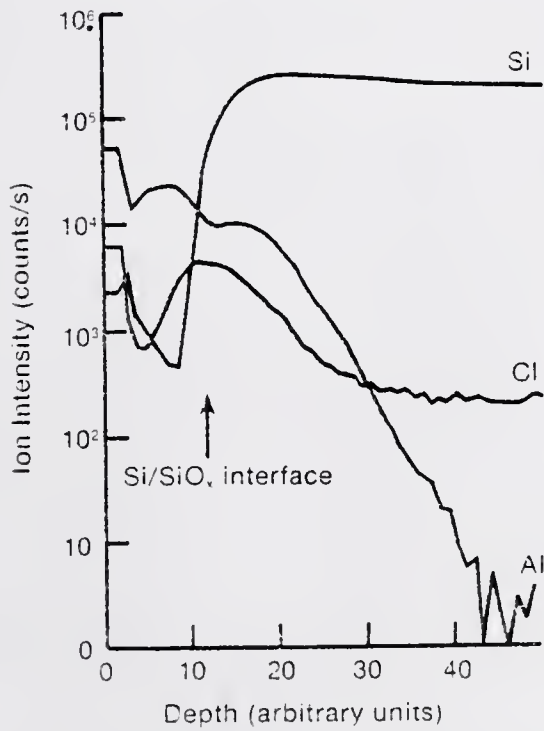
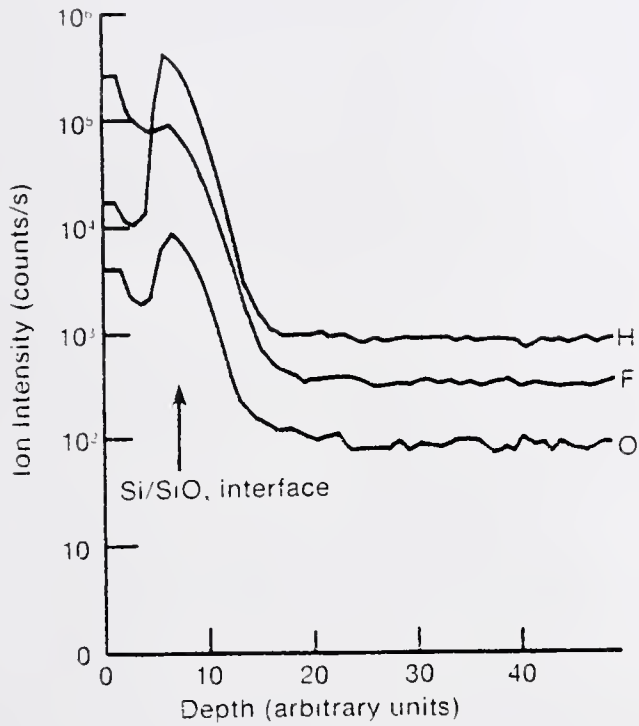


Figure 8.3 SIMS profiles of an MIS device fabricated with the beaker oxide technique.



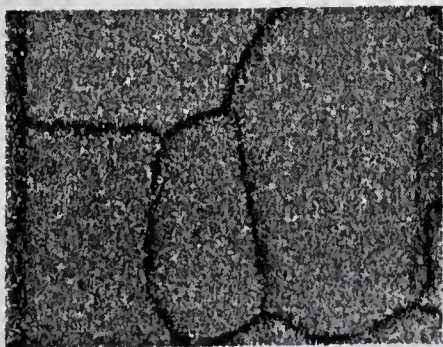
Figure 8.4 EBIC micrograph of an MIS polycrystalline silicon device fabricated with the beaker oxide technique showing changes in EBIC response from grain to grain.

from discussions with other researchers⁹³ that reproducible devices could be fabricated with an oxide grown at 600°C. Preliminary investigations in this work, however, indicated some change in grain boundary EBIC contrast due to 600°C heating. As reported above in this chapter, heating in air for ten minutes at temperatures up to 400°C did not affect the grain boundary EBIC contrast on finished devices. It was thus concluded that a fabrication process involving oxide growth at 200°C could be used without changing the as-cast condition. Results showed that oxidation at 200°C in air for ten minutes was sufficient to provide reproducible devices. Device processing was identical to that described earlier for the beaker oxide devices except for the actual oxide growth step. Details of the device fabrication are included in Appendix IV.

After devising a suitable device fabrication process, a suitable heat treatment procedure and schedule of appropriate times and temperatures had to be developed. A tube furnace was chosen due to availability of accurate temperature regulation, well known temperature profile and an ambient gas control system. Temperatures of 600, 750 and 900°C were chosen to best cover the range of temperatures of interest in various device processing schemes. A quartz tube and quartz boat with an atmosphere of flowing high purity argon were used for the initial heat treatments. All heat treatments were conducted on polysilicon which had been cut into one centimeter squares and cleaned and chemically polished as described in Appendix V. After heat treatment, the samples were again cleaned, etched to remove any oxide and then processed into devices as described above.

An EBIC map typical of the initial heat treated samples is shown in Fig. 8.5. While the grain boundaries act as strong recombination sites as expected, many intergrain recombination sites were also observed. These sites were unexpected, based on the absence of any such sites in p-n junction devices fabricated on similar materials and receiving similar heat treatment. Since the heat treatments of the MIS devices were not carried out in a clean-room environment, some form of contamination during heat treatment was suspected. To test this hypothesis, samples of cleaned polysilicon were encapsulated in quartz which was evacuated and back-filled with helium at least four times. This process did not provide a noticeable reduction of intergrain recombination sites. Further investigation revealed that the intergrain recombination sites were related to the rate at which the samples were heated to and cooled from the annealing temperature. The samples with a high density of intergrain sites had been thermally shocked. Samples which were slowly inserted into and removed from the hot zone of the furnace exhibited virtually no such sites.

The data to be presented in this chapter were all taken on samples which were heated and carefully handled to avoid thermal shock and which were quartz encapsulated during heating as described above. Other samples were prepared with identical processing except flowing argon, nitrogen or air was used in the tube furnace with the samples held in open-top quartz boats. Samples were also quartz encapsulated with air rather than helium. These samples resulted in identical devices, as determined by the EBIC measurements described below, to those which had been quartz uncapsulated in helium for heat treatment.



NO THERMAL SHOCK



THERMAL SHOCK

Figure 8.5 EBIC maps of devices fabricated on polysilcon which had been heated to 750°C.

The geometry of the EBIC measurement performed on a series of heat treated devices is shown in Fig. 8.1. Beam location A shows a typical scan path perpendicular to a grain boundary was used to evaluate $S_{\text{eff}}^{\text{gb}}$. Three to six grain boundaries were analyzed on each device and average values are reported. Figure 8.6 is a plot of $\ln I_{\text{EBIC}}$ versus distance for (a) an unheated sample, (b) a sample heated to 600°C, and (c) a sample heated to 900°C, each for one half hour. The asymptotic slope of $\ln I_{\text{EBIC}}$ for the 900°C sample ($\sim 0.08 \mu\text{m}^{-1}$) is considerably larger than for the unheated ($\sim 0.007 \mu\text{m}^{-1}$) or 600°C sample ($\sim 0.02 \mu\text{m}^{-1}$). Thus, assuming the value of D is the same for all samples, $S_{\text{eff}}^{\text{gb}}$ for the sample heated to 900°C is approximately four times larger than for the 600°C. Notice that if the more qualitative method of comparing grain boundary EBIC contrast were used, the same conclusions would be reached (i.e. $S_{\text{eff}}^{\text{gb}}$ is a factor of three to four higher for heating at 900°C as compared to 600°C). This was true for every case examined, indicating that relative EBIC contrast is a good qualitative indication of the grain boundary recombination velocity.

The effects of recombination at the insulator-semiconductor interface upon EBIC current are ignored when the equation given above is used. To test the importance of this recombination, line scans similar to those shown in Fig. 8.6 were recorded at beam voltages between ten and forty-five keV. At the lower voltages the slope of $\ln I_{\text{EBIC}}$ versus distance curves are dominated by the top surface recombination. This is expected because of the close proximity of carrier generation and the recombination surface. This point is further illustrated in Fig. 8.7 where normalized EBIC current (i.e., EBIC current divided by the product

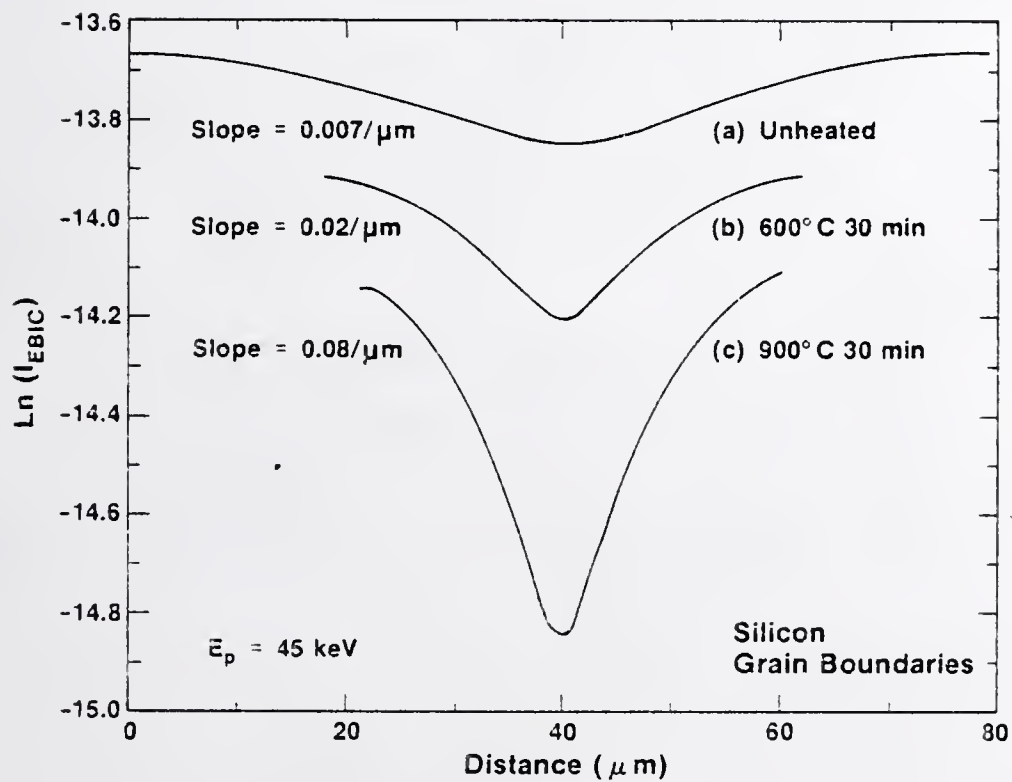


Figure 8.6 EBIC linescans across silicon grain boundaries which had received heat treatments of 200°C , 600°C and 900°C , plotted on a logarithmic scale.

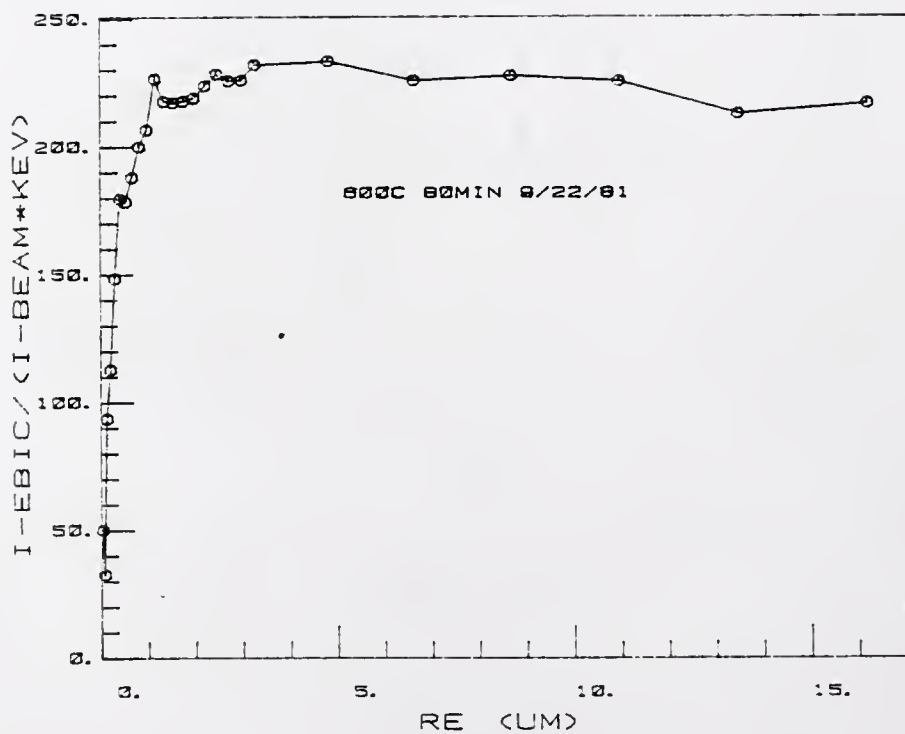


Figure 3.7 EBIC current divided by the product of the beam current and beam voltage versus the range of electrons in Si.

of primary beam current times beam voltage to normalize to constant generation factor) is plotted as a function of electron beam energy and hence electron range. Clearly the EBIC signal at low keV is dominated by top surface recombination. This shows up as a large increase in normalized EBIC as the electron range, and hence the distance from the top surface recombination plane, is increased. However, once the electron range is increased to four micrometers or larger, the effects of top surface recombination are less evident and the curve begins to decrease with increasing electron range. This decrease is due to an increase in the average distance from the collecting junction at which carriers are generated, and hence the slope is related to the carrier diffusion length.

For this study, data was taken at forty-five keV, where the expected electron range in silicon is approximately nineteen micrometers. Therefore, the generation depth is further from the insulator-semiconductor interface and this minimizes the distortion (such as that shown in Fig. 8.7) from recombination at this surface. Averages of experimental values of $S_{\text{eff}}^{\text{gb}}/D$ obtained from $\ln I_{\text{EBIC}}$ versus distance curves at forty-five keV are listed in Table 8-1 for the various heat treatments used in this study. If a typical value of twenty cm^2/sec is assumed for D ,⁹² the effective surface recombination velocities varied between $\sim 1 \times 10^3$ and 1×10^5 cm/sec. The recombination velocity increased upon heating for longer times at 600°C. The velocity was higher after heating 750°C and 900°C as compared to unheated samples or 600°C heat treated samples, but a time dependence was not readily apparent.

Table 8-1 Effective grain boundary recombination velocity (assuming $D = 20 \text{ cm}^2/\text{sec}$) and effective minority carrier diffusion length for heat treated polysilicon. One standard deviation of the data are reported.

Temperature	Time	$\frac{S}{D} (\mu\text{m}^{-1})$	$S(\text{cm}/\text{sec})$	$L_{\text{eff}} (\mu\text{m})$
unheated -		0.007 ± 0.004	1.4×10^3	20.2 ± 0.9
600°C	30 min	0.02 ± 0.005	4.0×10^3	18.2 ± 6.2
	70 min	0.02 ± 0.006	4.0×10^3	15.5 ± 3.4
	17 hours	0.04 ± 0.005	8.0×10^3	23.6 ± 2.3
	80 min	0.01 ± 0.005	2.0×10^3	17.9 ± 3.3
(air encapsulated)				
750°C	30 min	0.05 ± 0.008	1.0×10^4	16.9 ± 4.3
	1 hour	0.05 ± 0.01	1.0×10^4	10.5 ± 1.3
	18 hours	0.05 ± 0.01	1.0×10^4	13.8 ± 5.4
	65 min	0.06 ± 0.01	1.0×10^4	11.1 ± 0.6
(air encapsulated)				
900°C	30 min	0.06 ± 0.01	1.2×10^4	11.1 ± 2.0
	19 hours	0.05 ± 0.02	1.0×10^4	10.8 ± 1.7
	21 hours	0.06 ± 0.02	1.0×10^4	11.3 ± 2.9
	5 min	0.04 ± 0.01	3.0×10^3	13.3 ± 4.4
(thermal shock)				

Besides measuring $S_{\text{eff}}^{\text{gb}}$, the minority carrier diffusion length, L_{eff} , was also measured on all samples using beam position B as shown in Fig. 8.1. The beam was scanned perpendicular to the edge of the aluminum pad, and I_{EBIC} was recorded as a function of distance to the depletion region edge (i.e., Al edge). Measurements were made as far as possible from any grain boundaries. Under these conditions, L_{eff} is simply the inverse slope of the $\ln I_{\text{EBIC}}$ versus distance curves where the effective designation indicates that surface recombination effects are ignored.⁹⁴ L_{eff} values obtained using a 45 keV beam are included in Table 8-1. The data show that the effective diffusion length tended to increase with heat treatment time at 600°C as compared to the values of unheated samples. However, upon heating to 750°C or 900°C, the diffusion lengths were equal to, or less than, unheated samples and no systematic effects of heating time are apparent.

Similar to the case of grain boundary recombination velocities, the effective intragranular diffusion length measurements were affected by recombination at the insulator-semiconductor interface. To determine the effect of this upon the L_{eff} calculated from EBIC data, the bulk average diffusion length was measured by the x-ray technique described earlier. For an unheated sample, the average bulk value, L_{bulk} , was 94 μm . The two diffusion lengths L_{bulk} and L_{eff} , are different because of surface recombination, but may be related by⁹⁵

$$L_{\text{eff}}^2 = L_{\text{bulk}}^2 \left(1 - \frac{s_{\text{is}}}{s_{\text{is}} + 1} e^{-z/L_{\text{bulk}}} \right)$$

where s_{is} is the reduced insulator-semiconductor surface recombination velocity (see Chapter Three) and ξ is the generation depth of minority carriers for EBIC. The surface recombination velocity may be written as:

$$S_{is} = \frac{s_{is} D}{L_{bulk}}$$

where D is the minority carrier diffusivity. Using the value of $L_{eff} = 15 \mu\text{m}$ from an unheated MIS sample, and a value of $D = 20 \text{ cm}^2/\text{sec}$, S_{is} is about $2 \times 10^4 \text{ cm/sec}$. This value is reasonable based upon those reported previously for SiO_2/Si interface.⁹⁶

The data above indicated that L_{eff} tends to decrease on heating to 750°C or 900°C . This could be due to either a true decrease in bulk lifetime, and thus L_{bulk} , or an increase in S_{is} . For example, S_{is} could change during heat treatment if surface bonds are changed in the interfacial regions. Which mechanism is acting cannot be clearly identified without further data.

Physical Measurements

Auger Electron Spectroscopy and Secondary Ion Mass Spectroscopy with ion imaging have been used to physically investigate grain boundary chemistry before and after heat treatment. In-situ fracturing of polysilicon in a Perkin Elmer Model 590 Scanning Auger Microprobe was used to investigate impurity levels at grain boundaries for heated and unheated samples. It was found that grain boundaries of samples heated to 900°C exhibited oxygen Auger peaks. SIMS profiles of fractured grain

boundaries show that oxygen concentrations are higher over a much larger depth from the grain boundary fracture plane in heated samples versus unheated samples (~ 8 to 12 times deeper). Examples of the SIMS profiles are shown in Fig. 8.8, and corresponding SIMS spectra are shown in Fig. 8.9.

A Cameca IMS-3F ion microscope has been used to obtain ion images of grain boundaries. Oxygen images of grain boundaries have been obtained for some samples heated to 900°C, whereas no grain boundary oxygen could be imaged in unheated samples. Shown in Fig. 8.10 are oxygen ion images of silicon grain boundaries which had received a 900°C heat treatment. Another technique used to definitively identify oxygen accumulation to silicon grain boundaries after heat treatment was the SIMS linescan technique. In this technique a cesium ion beam is focused to a few microns, with the highest possible beam current density, and is held in a fixed position as the sample is scanned beneath the beam in the ion microprobe. The secondary ion optics are adjusted to obtain maximum spatial resolution in the depth profile mode, and a profile is made of each sample step position. The total counts at each step position are summed, excluding those obtained in the first two seconds to reduce artifacts, and the sums are plotted as a function of distance along the sample surface. Such a plot is shown in Fig. 8.11, definitively verifying the accumulation of oxygen at the grain boundary in a sample which had been heated to 900°C. Under identical conditions, no change in oxygen level was observed for unheated samples. Other bulk impurities identified by SIMS were C and Fe; however, no definitive

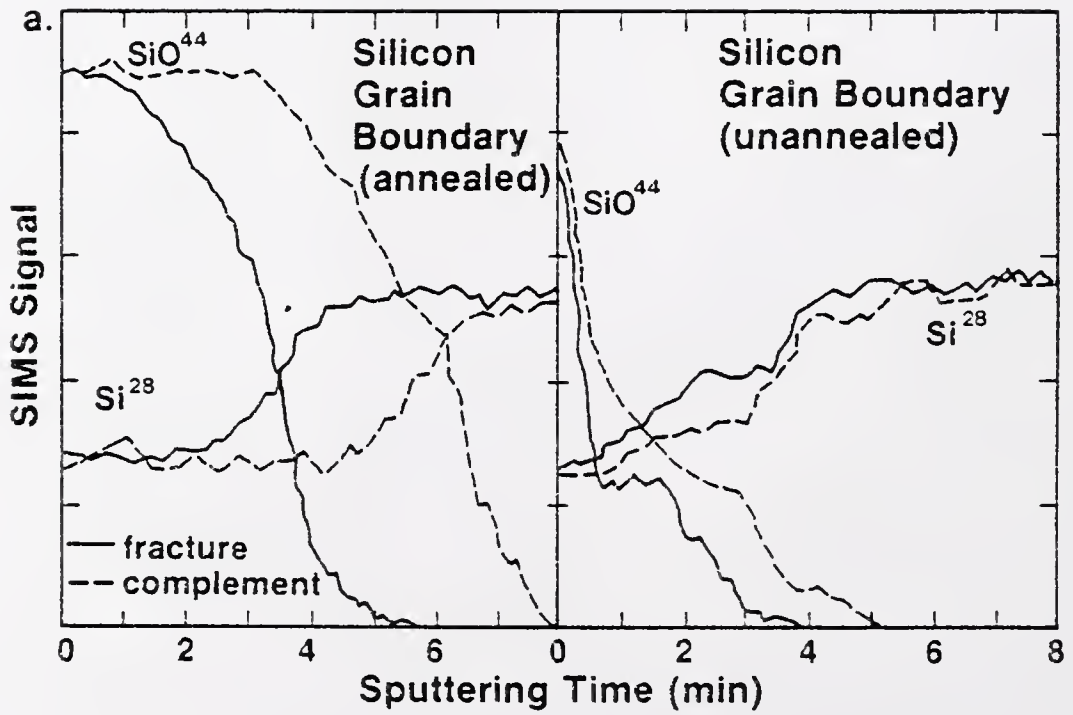


Figure 3.8 SIMS depth profiles of fractured polycrystalline silicon grain boundaries showing the effect of heating to 900°C before fracture.

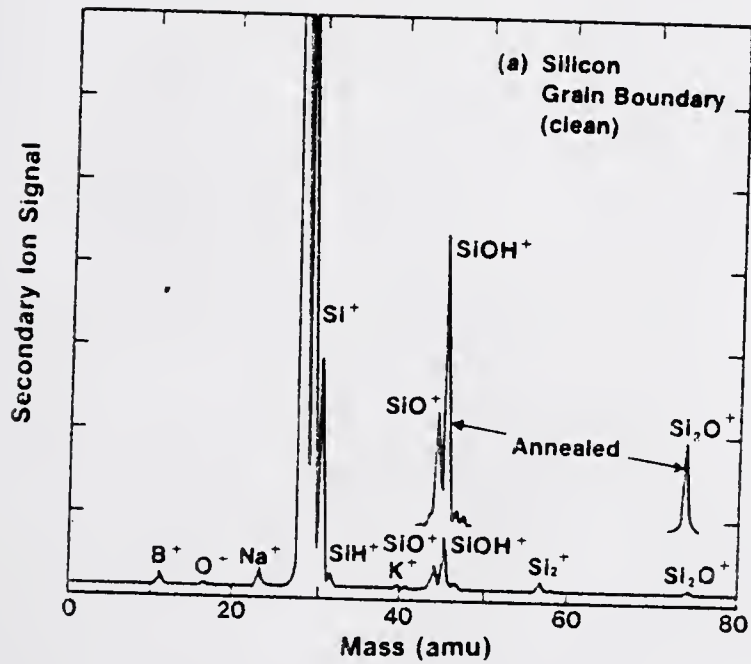


Figure 8.9 SIMS spectra of fractured polycrystalline silicon grain boundaries showing differences between heated and unheated conditions.

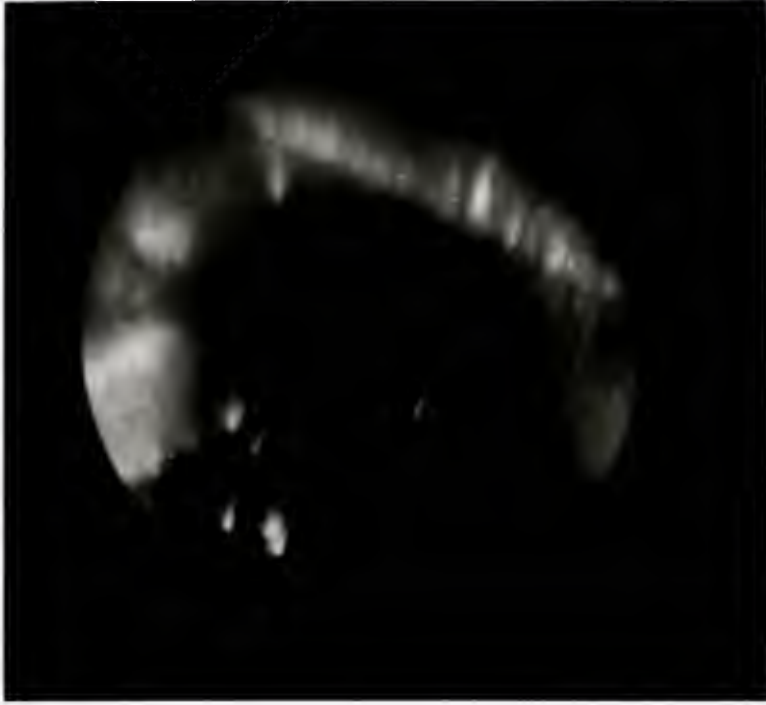


Figure 3.10 Oxygen ion microprobe images of 900°C treated polysilicon. Bright regions indicate oxygen presence. These regions were optically identified as grain boundaries. Image field is 400 microns.

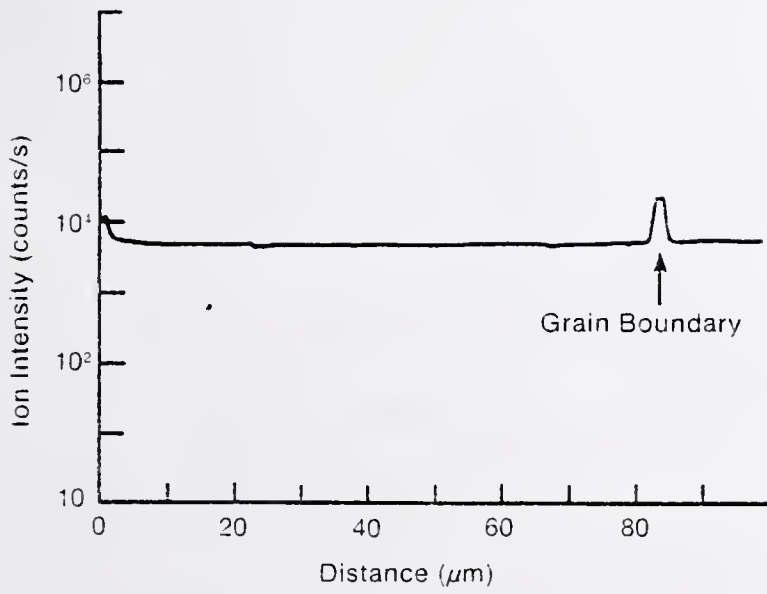


Figure 8.11 SIMS step scan across a heat treated (900°C, 300 minutes) silicon grain boundary.

accumulation of either of these at grain boundaries due to heat treatment has been measured. Attempts were made to examine grain boundary fracture surfaces in the ion microscope, but the inherent requirement of the system design for sample flatness prevented definitive analysis.

Heat treatments to temperatures in the range used in this work are known to affect the carrier lifetime in single crystal silicon.⁹⁷ For example, anneals of 450°C are known to activate thermal donors which are believed to be oxygen related. The mechanisms involved in such lifetime changes with heat treatment are not known, but are the subject of active current research.⁹⁷ In this work, the effective minority carrier diffusion length has been measured in all samples as a method of assuring that no large lifetime changes were affecting the results of the grain boundary recombination velocity measurements.

Discussion

The results described above clearly show that heat treatment of cast polycrystalline silicon increases the recombination of carriers at grain boundaries. Some effects are seen at temperature as low as 600°C, while no effects were observed for a 400°C anneal. Anneals at 750°C or 900°C greatly increase grain boundary recombination after one-half hour at temperature.

Transmission electron microscopy was utilized on heated samples to investigate the possibility of grain boundary precipitation. The major problem encountered in this work was the development of reliable sample thinning techniques. Chemical thinning techniques were investigated

initially, but abandoned due to the preferential chemical attack at grain boundaries. Therefore, ion milling techniques were developed as described in Chapter Three. In a single sample, typically only one to five micrometers of grain boundary length could be examined properly. Therefore many samples were prepared until a total grain boundary length of over 200 micrometers was examined. Microscopy at magnifications of at least 180,000 was used to look for grain boundary precipitates. This assured the ability to observe any precipitate with any dimension of fifty angstroms or more. No precipitates were observed in any of the heat treated samples, and thus the heat treated grain boundaries could not be distinguished from non-heated boundaries by conventional TEM.

The values obtained for grain boundary recombination velocity in this work were in the range of 10^3 to 10^4 cm/sec for activated, or heat treated grain boundaries. Mazer⁹⁸ has recently reported calculation of grain boundary recombination velocity, based on I-V measurements, of $\sim 2.2 \times 10^4$ cm/sec for devices fabricated on material similar to that used in this study. His devices had received heat treatments of $\geq 900^\circ\text{C}$. For devices receiving similar heat treatment in this work, an average value of 1.2×10^4 cm/sec was obtained. These values are in very good agreement considering the very different techniques used for the measurements. Seager's⁶⁴ suggestion that the technique used in this work will result in values a factor of 2 to 10 too low (see Chapter Three) would explain the discrepancy between the two values. However, as

discussed in Chapter Three, Zook's⁶² technique requires curve fitting by computer and has not been shown to provide more accurate results than the approach used in this work.

The most likely mechanism for the type of temperature dependent behavior reported above is impurity segregation. Oxygen redistribution during high temperature (800°C - 1000°C) anneal has been clearly demonstrated by others in single crystal silicon. Oxygen has been found to segregate to surfaces,⁹⁹ damaged layers (from ion implantation)¹⁰⁰ and to dislocations.¹⁰¹ Grain boundary segregation from the bulk is known to occur at elevated temperatures in polycrystalline materials.¹⁰² Physical evidence of oxygen segregation to grain boundaries has been obtained for samples annealed at 900°C in this work. Values of the diffusion coefficient of oxygen in silicon have been reported in the literature.¹⁰³ Using the reported value of $D = 10^{-11}$ cm²/sec for 900°C, a diffusion distance of two micrometers for sixty minutes of 900°C is obtained. Thus diffusion of oxygen at the temperatures used in this work is expected to be sufficient to explain the results reported.

It has been suggested in the literature that impurities other than oxygen segregate to silicon grain boundaries.¹⁰⁴⁻¹⁰⁶ For example, Kazmerski et al.¹⁰⁵ examined fractured grain boundaries in polycrystalline silicon containing intentional impurities of Al, Ti or Cu at ~ 0.001 atomic %. In each of these cases the intentional impurities were found to segregate to grain boundaries. In addition, in some samples which did not have intentional impurities added Fe and/or Al was found at fractured grain boundary surfaces in addition to oxygen. This occurred primarily in SEMIX¹⁰⁷ polycrystalline silicon which was found to

have cleaner grains, but more impurities at grain boundaries than Wacker material. This is probably due to a casting process that more efficiently fosters the grain boundary segregation of impurities for the SEMIX material. (Details of the SEMIX casting process are proprietary and thus unknown to the author.) Even in the SEMIX material, however, oxygen was observed at all grain boundaries where Fe and Al were observed, and at many boundaries only oxygen was observed. Kazmerski et al.¹⁰⁵ further report that metallic impurities were found to be localized rather than spread throughout the grain boundary plane. The oxygen was observed to be much more uniform in concentration on the grain boundary fracture surface. Thus, the oxygen is a more likely candidate for determining the recombination properties of grain boundaries reported in this work.

Attempts were made to detect grain boundary segregation of impurities using AES mapping of un-fractured samples (i.e., along the intersection of the grain boundary plane with the wafer surface). These attempts, however, were unsuccessful due either to the low levels of impurities present or to the alteration of this region during wafer cleaning and etching processes. This prompted the ion microscopy studies described above, which were successful in the identification of oxygen segregation. Similar studies were attempted to look for Fe segregation, using an oxygen primary beam to enhance the yield of secondary Fe ions, but no Fe segregation would be detected by ion microscopy. This is in agreement with the literature results discussed above which indicate that Fe, when present at grain boundaries, occurs only in very localized regions on the grain boundary plane. This further

supports the conclusion that the oxygen segregation is the only impurity segregation that can be directly linked with the uniform (along a grain boundary length) increase in grain boundary recombination velocity.

Based on the fact that oxygen was detected in fractured grain boundaries using AES, and that the detection limit of AES for oxygen in silicon is approximately 0.1 atomic %, it is apparent that the oxygen content in the grain boundary plane for heated samples is at least 0.1 atomic %. An estimate of the oxygen concentration indicated by the SIMS data has been made for comparison. The SIMS stepscan data was utilized for this analysis. In the stepscan mode the effective beam size on the sample surface is controlled by the field limiting aperture used. The data shown in Fig. 8.11 was taken using an effective spot size of 1.4 μm diameter. Thus the area analyzed in a given step is approximately $2 \times 10^{-8} \text{ cm}^2$. If the beam is centered on a grain boundary, a small fraction of the analyzed area will consist of the grain boundary. If we assume an effective grain boundary width of 200 \AA , then the grain boundary area is a rectangle 200 \AA by 1.4 μm with an area of $\sim 3 \times 10^{-10} \text{ cm}^2$. Thus the ratio of grain boundary area analyzed to total area analyzed is $(3 \times 10^{-10} \text{ cm}^2)/(2 \times 10^{-8} \text{ cm}^2) \approx 2 \times 10^{-2}$. Thus the apparent concentration in the step scan plot will be $\sim 2\%$ of the actual concentration in the grain boundary. For the Wacker polycrystalline silicon used in this work, the background oxygen concentration is estimated to be $\sim 5 \times 10^{17} \text{ cm}^{-3}$. From Fig. 8.11, the apparent oxygen concentration at the grain boundary is ~ 8 times the background concentration, or $\sim 4 \times 10^{18} \text{ cm}^{-3}$. Thus using the above analysis, the actual grain boundary concentration would be 2% of $4 \times 10^{18} \text{ cm}^{-3}$ or $2 \times 10^{20} \text{ cm}^{-3}$.

The atomic density⁹² of Si is $5 \times 10^{22} \text{cm}^{-3}$, so this concentration corresponds to 0.4 atomic %. The uncertainty in this calculation must be considered to be at least a factor of two, but the agreement with the estimate from the Auger detection limit is very good.

The initial heat treatment schedule and subsequent EBIC data clearly showed a high density of high recombination defects. Careful control of heat treatment to avoid thermal shock of the samples provided samples with greatly reduced concentrations of such mid-grain recombination sites. It is believed that thermal shocking of polysilicon was inducing dislocations which act as recombination sites. The thermal shocking did not have a measurable effect on $S_{\text{eff}}^{\text{gb}}$, but did make the use of EBIC to measure $S_{\text{eff}}^{\text{gb}}$ much more difficult. Heating of samples in flowing argon, nitrogen and air was compared to samples sealed in He filled quartz tubes for heating. We did not find obvious differences except in the case of growing an oxide for the MIS structure. The source of the segregating oxygen is believed to be internal, i.e., any segregated oxygen appears to come from the bulk grains.

Conclusions

It has been shown that heat treatment of cast polycrystalline silicon to temperatures appropriate for solar cell device fabrication substantially alters the properties of grain boundaries. Effective grain boundary recombination velocity has been shown to increase on heating to 600°C, with a definite time dependence observed. Heating to 750°C or 900°C has a larger effect on $S_{\text{eff}}^{\text{gb}}$, with no time dependence observed for anneals of thirty minutes to twenty hours. Grain boundary

segregation of oxygen was detected for the annealed samples, consistent with data in the literature. Thus, it was concluded that oxygen segregation is the most likely mechanism for altering $S_{\text{eff}}^{\text{gb}}$ during heating of polysilicon. We have also shown that anneals of 400°C or lower do not substantially effect $S_{\text{eff}}^{\text{gb}}$. The usefulness of the EBIC technique to study grain boundaries has been demonstrated. Careful analysis of the slope of the EBIC current approaching grain boundaries was used to arrive at $S_{\text{eff}}^{\text{gb}}$ values, and the results were shown to agree with more qualitative approach of comparing EBIC contrast. Thus it is concluded that comparisons of EBIC contrast of grain boundaries is a valid qualitative measure of $S_{\text{eff}}^{\text{gb}}$. EBIC was also used to show that thermal shocking of polysilicon induces dislocations which act as high recombination sites.

CHAPTER NINE

DISCUSSION AND CONCLUSIONS

Discussion

The purpose of this work was to gain an understanding of the electrical and chemical properties of grain boundaries in polycrystalline silicon. The major emphasis of the work was related to the potential use of polycrystalline silicon as a low cost solar cell material. However, an understanding of silicon grain boundaries is also important in the VLSI field where the use of polycrystalline silicon is becoming important. A general review of the properties of grain boundaries in silicon was given in Chapter Two with an emphasis on electrical properties and models. Current and potential applications of polysilicon were reviewed and the specific case of polysilicon as a solar cell material was reviewed in more detail. For solar cell applications, carrier recombination at grain boundaries is the major limitation of polysilicon. Carrier transport across grain boundaries is not generally considered to be a major problem since this can be avoided with proper grain structure control.

The EBIC technique has been used extensively in this work to investigate local recombination properties of silicon grain boundaries. A brief review of the EBIC technique was given in Chapter Three, beginning with an historical overview. The simple modification necessary to a conventional SEM to allow collection of EBIC data were discussed. Specific techniques for measuring minority carrier diffusion length and surface recombination velocity were described and theoretical models

used for data interpretation were discussed. Finally, limitations of currently available hardware and theory for the obtaining of quantitative EBIC results were outlined.

To improve on the hardware limitations of available EBIC systems, a new totally automated EBIC system was designed and incorporated into a Cameca MBX electron probe and a JEOL 35C SEM. The details of this system were described in Chapter Five. The major motivation in designing an automated EBIC system was the desire to be able to obtain a large number of quantitative EBIC linescans with the highest accuracy (both in current and distance) possible and the least human input possible. This was due to the fact that a large number of EBIC measurements of a large number of silicon grain boundaries were required to obtain statistically meaningful results on the polysilicon studied.

The specific functions automated with the system described in Chapter Five include electron beam current and position, beam current regulation, sample stage position, EBIC current reading and recording, data display, storage, analysis and output. EBIC stages were developed to allow for rapid sample exchange without breaking vacuum. Such a stage was designed for both an SEM and an EPMA. Specific advantages of the use of an EPMA system over an SEM system were discussed. Although the automated EBIC system was developed for this study of silicon grain boundaries, it has been used in studies of many other materials as well. References to these works were given in Chapter Five.

In Chapter Six, the experimental importance of EBIC parameters was measured and discussed. Reproducibility of EBIC linescans data was of major concern, and reproducibility of within a few percent was

demonstrated using the automated system described in Chapter Five. The useful range of electron beam current and voltage was examined and found to be limited on the low end mainly by signal-to-noise problems and on the high end by the onset of beam damage. Beam currents below 500 pA were found useful for beam voltages up to 50 keV. This upper limit of beam current effectively prevents high injection conditions from existing during EBIC analysis as well.

The use of EBIC imaging techniques, complemented by optical microscopy, groove and stain techniques and conventional SEM imaging provided considerable insight into the grain size, grain structure, junction structure and general recombination effects of silicon grain boundaries. Grain size was measured as 1.63 ± 0.45 millimeters. EBIC techniques using beveled samples containing a diffused p-n junction were developed and revealed enhanced grain boundary diffusion of phosphorus resulting in p-n junction spikes at grain boundaries after diffusion at 900°C or 1040°C.

Studies of the effects of heat treatment at temperatures typical for junction diffusion were conducted using the EBIC techniques developed. This resulted in the first reported systematic study of the effects of heat treatment on grain boundaries in polycrystalline silicon.²¹ Grain boundary recombination velocities were found to increase at least one order of magnitude as a result of heat treatment. For 400°C heat treatments, no effects on $S_{\text{eff}}^{\text{gb}}$ were observed. For 750°C and 900°C, $S_{\text{eff}}^{\text{gb}}$ was found to increase with no apparent time dependence for times of one-half to twenty hours. A maximum average value of 1×10^4 cm/sec was reported.

The results of the EBIC studies on heat treatment effects suggested that chemical segregation may be causing changes in grain boundary electrical activity. This led to the development of surface analysis techniques for the investigation of silicon grain boundary chemistry. In-situ grain boundary fracturing techniques were developed which allowed for complementary AES and SIMS measurements to be made of a fractured grain boundary surface. Use of these techniques revealed the segregation of oxygen to grain boundaries during heat treatments of 600°C or higher. However, the fact that the fracturing technique was somewhat unreproducible (i.e., it was not always possible to fracture a sample along a given grain boundary) direct ion microscopy techniques were developed to verify the occurrence of oxygen grain boundary segregation. These techniques included direct imaging of secondary oxygen ions using a cesium primary ion beam and the stepping of a finely focused cesium primary beam across a grain boundary and plotting oxygen ion intensity as a function of primary beam position. These techniques verified the segregation of oxygen to grain boundaries in silicon samples heated to 900°C. Local concentrations of 0.1 atomic % were measured. TEM analysis was used to look for the presence of any precipitation of grain boundaries after heat treatment. After investigation of over 200 μm of grain boundary length, it was concluded that the oxygen segregation observed by AES and SIMS was not accompanied by precipitation.

As alluded to early in this dissertation, a grain boundary is formed in a material when two crystals oriented differently in space have a common interface. In a perfect single crystal, atoms are

spatially arranged in a very predictable periodic lattice. It is the periodicity of a crystal lattice that gives rise to the predictable, symmetric (in the case of symmetric crystals) properties of single crystal materials. The materials scientist's understanding of the behavior and properties of crystalline materials is largely due to his understanding of the periodicity and symmetry of the crystal lattice. These properties form the basis of the quantum theory of the solid state. The band structure model, heavily relied upon for the prediction and understanding of the properties of semiconductor crystal, is a result of periodic boundary conditions applied to the Schroedinger equation description of electrons. Thus, it is not surprising that the level of understanding of solid materials at grain boundaries, where symmetry and periodicity conditions break down, is incomplete at best. The major purpose of this work was to increase the level of understanding of silicon grain boundaries, in particular as related to the use of polycrystalline silicon as a solar cell material.

The author's first approach to gain an understanding of silicon grain boundaries was through the investigation of the crystallography of the interface itself. These investigations were inspired by the work of Walter Bollmann¹⁰⁸ whose theory of crystalline interfaces provides a starting point for the fundamental understanding of grain boundaries.³⁴ The basic premise of Bollmann's theory is that by knowing the exact spatial relationship of one grain to another and the location of the grain boundary plane one can then predict the energetically favorable atomic positions which will be occupied at and near the grain boundary. One could then predict the two-dimensional symmetry of the

grain boundary itself and infer the most likely dislocation structure and energy content of the grain boundary. This in turn would be related to the specific properties of grain boundaries such as segregation coefficients, diffusion coefficients, electrical conductivity, recombination sites, etc. The crystallography of a grain boundary is its most fundamental property and all other properties are inherently derived from its crystallography. This approach to understanding grain boundaries is appealing because of its very fundamental nature.

To make use of Bollmann's theory to describe grain boundaries in polycrystalline silicon, techniques were needed to determine the exact crystallographic relationship of one grain with respect to the reference grain. The use of electron channeling techniques in a scanning electron microscope was thoroughly investigated for this purpose. The reasons for the choice of the electron channeling technique included the ability to rapidly obtain crystal orientation from a small single grain ($\geq 100\mu\text{m}$) in a bulk polycrystalline sample, the ease with which the information could be acquired, and the availability of equipment (JEOL JSM 35C SEM with selected area diffraction component (SDC) attachment). A complete review of the technique has recently been given by Joy, Newbury and Davidson.¹⁰⁹ It was found that while the electron channeling patterns were easy to obtain and interpret, the accuracy with which a given grain could be oriented was on the order of two degrees of rotation around each axis of an orthogonal coordinate system. This is not sufficiently accurate to uniquely determine the atomic structure of a grain boundary or to apply Bollmann's model. It was thus decided that the approach of understanding grain boundaries via an exact determination of their

crystallography was not currently feasible for a bulk polycrystalline material such as the Wacker polysilicon used in this work. Such studies would only be possible on selected grain boundaries and would require techniques such as transmission electron microscopy where extensive sample modification is required. The results of the work presented here must be considered more of a statistical nature, providing average properties of grain boundaries. Future work dealing with well controlled and well characterized single grain boundaries is needed before a complete understanding of the electrical and chemical properties of silicon grain boundaries can be gained.

Conclusions

The main contributions of this dissertation are as follows:

- (A) The development of a fully automated electron beam induced current measurement system including hardware and software development (Chapter Five) and the demonstration of its usefulness on both a scanning electron microscope and an electron probe micoralyzer for the investigation of grain boundaries in polycrystalline silicon solar cells (Chapter Eight).
- (B) The detailed investigation of the influence of experimental parameters on the measurement of grain boundary recombination velocity and the defining of a useful range of beam current and voltage values for which beam damage can be avoided and reproducible data obtained (Chapter Six).
- (C) The measurement of grain size and grain structure in Wacker Silso cast polycrystalline silicon (Chapter Seven).

- (D) The measurement, with complementary bevel and stain and bevel/EBIC analysis techniques of preferential diffusion of phosphorus in silicon grain boundaries. These measurements lead to the determination that the grain boundary diffusion coefficient is 8×10^4 times large than the corresponding bulk coefficient (Chapter Seven).
- (E) The development of a test device structure for EBIC analysis of p-type polycrystalline silicon which does not require high temperatures for device fabrication (Chapter Eight).
- (F) The measurement of increased grain boundary recombination velocity as a result of heat treatment of polycrystalline silicon using EBIC techniques (Chapter Eight)
- (G) The development of surface analysis techniques for the study of grain boundary segregation in polycrystalline silicon and the use of these techniques to observe the grain boundary segregation of oxygen as a result of heat treatment (Chapter Eight).

REFERENCES

1. H. Fischer, in Photovoltaic Solar Energy, edited by A. Strub (D. Reidel, Holland, 1977), p. 52.
2. J. Lindmayer, in Proceedings of Twelfth IEEE Photovoltaic Specialists Conference (IEEE, New York, 1976), p.82.
3. M.A. Green, A.W. Blakers, M.R. Willison, E. Gauja and T. Szpitalak, in Proceedings of Sixteenth IEEE Photovoltaic Specialists Conference (IEEE, New York, 1982), (in press).
4. H. Fisher and W. Pschunder, IEEE Trans. Electron. Devices ED-24, 438 (1977).
5. T.L. Chu, J. Cryst Growth 39, 45 (1977).
6. E.A. DeMeo and P.B. Bos, EPRI Rep. ER-589-SR, (1978).
7. G.B. Turner, D. Tarrant, D. Aldrich, R. Pressley and R. Press, in Proceedings of Sixteenth IEEE Photovoltaic Specialists Conference (IEEE, New York, 1982), in press.
8. H. Fischer and W. Pschunder, in Proceedings of Twelfth IEEE Photovoltaic Specialists Conferences (IEEE, New York, 1976), p. 86.
9. T. Giszek, in Proceedings of Sixteenth IEEE Photovoltaic Specialists Conference (IEEE, New York, 1982), (in press).
10. T. Surek, in Proceedings of Symposium of Electronic and Optical Properties of Polycrystalline or Impure Semiconductors and Novel Silicon Growth Methods (Electrochemical Society, Pennington, N.J. 1980), p. 173.
11. L.L. Kazmerski, W.B. Berry and C.W. Allen, J. Appl. Phys. 43, 3515 (1972).
12. L.L. Kazmerski and P.E. Russell, in Semiconducteurs Polycristalins, les Editions de Physique (1982), (in press).
13. S. Amelinckx, and W. DeKeyser, Solid State Physics, Vol. 8 (Academic Press, New York, 1959), p. 325.
14. D. McLean, Grain Boundaries in Metals, (Clarendon Press, Oxford, 1957).
15. R.T.P. Whipple, Phil. Mag. 45, 1225 (1954).
16. H.J. Qulessner, K. Hubner and W. Shuckley, Phys. Dev. 123, 1245.

17. A. Ourmazd, P.R. Wilshaw, E. Weber, H. Gottschalk, G.R. Booke and H. Alexander, in Proceedings of Fourteenth annual Meeting Electron Microscopy Society of America, edited by G.W. Bailey (Claitor's Publishing Division, Baton Rouge, 1982), p. 438.
18. B. Cunningham, in Proceedings of Fourteenth Annual Meeting Electron Microscopy Society of America, edited by G.W. Bailey (Claitor's Publishing Division, Baton Rouge, 1982) p. 434.
19. B. Cunningham, H. Strunk and D.G. Ast, *Appl. Phys. Lett.* 40, 237 (1982).
20. C.B. Carter, in Grain Boundaries in Semiconductors, edited by H.J. Leamy, G.E. Pike and C.H. Seager, (North Holland, New York, 1982), p. 33.
21. P.E. Russell, C.R. Herrington, D.E. Burk and P.H. Holloway, in Grain Boundaries in Semiconductors, edited by H.J. Leamy, G.E. Pike and C.H. Seager (North-Holland, New York, 1982), p. 185.
22. D. Redfield, *Appl. Phys. Lett.* 38, 174 (1981).
23. N.M. Johnson, D.K. Biegelsen and M.D. Moyer, *Appl. Phys. Lett.* 40, 882 (1982).
24. L.L. Kazmerski in Polycrystalline and Amorphous Thin Films and Devices, edited by L.L. Kazmerski (Academic Press, New York, 1980), ch. 3.
25. R.L. Petritz, *Phys. Rev.* 104, 1508 (1956).
26. M.E. Crowder and T.O. Sedgewick, *J. Electrochem. Soc.* 119, 1565 (1972).
27. A.L. Fripp, *J. Appl. Phys.* 46, 1240 (1975).
28. L.I. Kamins, *J. Appl. Phys.* 42 4357 (1971).
29. P. Rai-Chedhury and P.L. Honeer, *J. Electrochem. Soc.* 120, 1761 (1973).
30. J.Y.W. Seto, *J. Electrochem. Soc.* 122, 701 (1975).
31. W.E. Taylor, N.H. Odell and H.V. Fan, *Phys. Rev.* 88, 867 (1952).
32. R.K. Mueller, *J. Appl. Phys.* 32, 635 (1961).
33. R.K. Mueller, *J. Appl. Phys.* 32, 640 (1961).
34. W. Bollmann, Crystal Defects and Crystalline Interfaces (Springer-Verlag, Berlin, 1970).

35. J.Y.W. Seto, J. Appl. Phys. 46, 5247 (1975).
36. A. Maxy, Y. Goldstein and N.B. Grover, Semiconductor Surfaces (North-Holland, Amsterdam, 1965), 5 and 9.
37. C.H. Seager and J.G. Castner, J. Appl. Phys. 49, 3879 (1978).
38. C.H. Seager and D.S. Ginley, Appl. Phys. Lett. 34, 337 (1979).
39. G.E. Pike and C.H. Seager, J. Appl. Phys. 50, 3414 (1979).
40. C.H. Seager, G.E. Pike and D.S. Ginley, Phys. Rev. Lett. 43, 532 (1979).
41. C.H. Seager and D.S. Ginley, in Proceedings of Photovoltaic Materials Device Measurements Workshop: Focus Polycrystalline Thin Film Cells (Solar Energy Research Institute, Golden, CO, 1979), p. 115.
42. C.H. Seager and G.E. Pike, Appl. Phys. Lett. 35, 709 (1979).
43. J.I. Goldstein, D.E. Newbury, P. Echlin, D.C. Joy, C. Fiori and E. Lifshin, Scanning Electron Microscopy and X-ray Microanalysis (Plenum Press, New York, 1981).
44. C.A. Klein, J. Appl. Phys. 39, 2029 (1968).
45. P. Rappaport, Phys. Rev. 93, 246 (1954).
46. J.J. Lander, H. Schreiber, I.M. Buck and J.R. Matheus, Appl. Phys. Lett. 3, 206 (1963).
47. I.E. Everhart, O.C. Wells and R.K. Malta, Proc. IEEE 52, 1642 (1964).
48. D.B. Holt, in Quantitative Scanning Electron Microscopy, edited by D.B. Holt, M.D. Muir, P.R. Grant and I.M. Boswarva (Academic Press, London, 1974), p. 213.
49. H.J. Leamy, J. Appl. Phys. 53, R51 (1982).
50. T.P. Ma, Appl. Phys. Lett. 27, 615 (1975).
51. W.R. Bottoms, D. Guterman and P. Roitman, J. Vac. Sci. Technol. 12, 134 (1975).
52. J.F. Bresse, in Proceedings of Fifth Annual SEM Symposium (IITRI, Chicago, 1972), p. 105.
53. A.E. Gruen, Z. Naturforsch 12A, 89 (1957).
54. H.J. Hovel, Solar Cells, (Academic Press, New York, 1975).

55. H.C.W. Huang, C.F. Aliotta and P.S. Ho, *Appl. Phys. Lett.* 41, 54 (1982).
56. S.M. Sze, Physics of Semiconductor Devices (J. Wiley, New York, 1969).
57. E. Miyazaki and K. Miyaji, *Japanese J. Appl. Phys.* 2, 129 (1963).
58. M. Watanabe, G. Actor and H.C. Gatto, *IEEE Trans. Electron. Devices* ED-24, 1172 (1977).
59. C. Van Opdorp, *Phillips Res. Reports* 32, 192 (1977).
60. W.H. Hackett, Jr. *J. Appl. Phys.* 43, 1649 (1972).
61. M. Watanabe, H.C. Gato and G. Actor, in *Proceedings of International Symposium Solar Energy*, edited by J.B. Berkowitz and I.A. Lesk (Electrochem. Soc., Princeton, N.J., 1976), p. 283.
62. J.D. Zook, *Appl. Phys. Lett.* 37, 223 (1980).
63. G.U. Hari Rao, H.E. Bates and K.U. Rauf, *J. Appl. Phys.* 47, 2614 (1976).
64. C.H. Seager, *J. Appl. Phys.* 53, 5968 (1982).
65. F. Berz and H.K. Kaiken, *Solid State Electron* 19, 437 (1976).
66. B. Authier, *Adv. in Solid State Physics* 18, 1 (1978).
67. D. Helmreich, in *Proceedings of the Symposia on Electronic and Optical Properties of Polycrystalline or Impure Semiconductors and Novel Silicon Growth Methods*, edited by K.V. Ravi and B. O'Mara (Electrochemical Society, Pennington, N.J., 1980), p. 184.
68. D. Helmreich and G. Ast, in *Proceedings of the Symposia on Electronic and Optical Properties of Polycrystalline or Impure Semiconductors and Novel Silicon Growth Methods*, edited by K.V. Ravi and B. O'Mara (Electrochemical Society, Pennington, N.J., 1980), p. 233.
69. D. Helmreich and H. Serter, in *Proceedings of the Second Electrochemical Photovoltaic Solar Energy Conference* (D. Reidel, Dordrecht, 1979), p. 742.
70. A. Georges, J.M. Fournier, J.P. Gonchond and D. Bois, Scanning Electron Microscopy (SEM, Inc., Chicago, 1980), p. 69.
71. A. Georges, J.M. Fournier and D. Bois, Scanning Electron Microscopy (SEM, Inc., Chicago, 1982) (in press).

72. A. Georges, J.M. Fournier, D. Bois and D. Monty, *J. Microsc. Spectrosc. Electron.* 6, 55 (1981).
73. F.H. Shamber, "Flextran," copywrited internal report, Tracor Northern, 2551 West Beltline Hwy., Middleton, WI, 1975.
74. P.E. Russell, O. Jamjoun, R.K. Ahrenkiel, L.L. Kazmerski, R.A. Mickelsen and W.S. Chen, *Appl. Phys. Lett.* 40, 995 (1982).
75. P. Sheldon, R.E. Hayes, P.E. Russell, R.N. Nottenburg, K.A. Emery, P.J. Ireland and L.L. Kazmerski, *J. Vac. Sci. Technol.*, 20, 410 (1982).
76. P. Sheldon, R.K. Ahrenkiel, R.E. Hayes and P.E. Russell, *Appl. Phys. Lett.* (1982). Oct. 15 issue, in press.
77. K. Emery, P. Withey, P.E. Russell, G. Cheek, R. Mertens, and R. Van Overstraeten, in *Proceedings of Sixteenth IEEE Photovoltaic Specialists Conference (IEEE, New York, 1982)* (in press)..
78. J.I. Haroka, R.O. Bell and B.R. Bathey, in *Proceedings of Symposia on Electronic and Optical Properties of Polycrystalline or Impure Semiconductors and Novel* K.V. Ravi and R. O'Mara (Electrochemical Society, Pennington, N.J., 1980), p. 76.
79. R.T. DeHoff, Quantitative Microscopy, edited by F.N. Rhines and R.T. DeHoff (McGraw-Hill, New York, 1968), 5.
80. H.J. Quiesser, K. Hubner and W. Shockley, *Phy. Rev.* 123, 1245 (1961).
81. C.P. Wu, E.C. Douglas, C.W. Mueller and R. Williams, *J. Electrochem. Soc.* 126, 1982 (1979).
82. R.M. Burger and R.P. Donovan, Fundamentals of Silicon Integrated Device Technology, Vol. 1 (Prentice-Hall, Englewood Cliffs, N.J., 1967), p. 313.
83. J.A. Mazer, Methods for Investigating the Properties of Polycrystalline Silicon P-N Junction Solar Cells (Ph.D. Dissertation, University of Florida, 1981) p. 103.
84. P.H. Holloway, *J. Vac. Sci. Technol.* 21(1), 19 (1982).
85. R.T.P. Whipple, *Phil. Mag.* 45 1225 (1954).
86. A.D. LeClaire, *Bri. J. Appl. Phys.* 14, 351 (1963).
87. T. Suzuoka, *Japanese J. Inst. Metals* 2, 25 (1961).

88. D. Redfield, in Proceedings of Fifteenth IEEE Photovoltaic Specialists Conference (IEEE, New York, 1981), p. 1179.
89. D. Redfield, Appl. Phys. Lett. 38, 174 (1981).
90. Solar Energy Research Institute Polycrystalline Silicon Subcontractors Review Meeting, SERI CP6141263 (1981).
91. W. Rozenzweig, Bell System Tech. J. 41, 1573 (1962).
92. A.S. Grove, Physics and Technology of Semiconductor Devices (John Wiley and Sons, New York, 1967).
93. Dorothea E. Burk, Private communication (1981).
94. W.H. Hackett, Jr., J. Appl. Phys. 43, 1649 (1972).
95. L. Jastrzeliski, J. Lagonski and H.C. Gato, Appl. Phys. Lett. 27, 537 (1975).
96. T.G. Fossum, F.A. Lindholm and M.A. Shibib, IEEE Trans. Elec. Div. ED-26, 1294 (1979).
97. Materials Research Society 1982 Symposium on Defects in Semiconductors, Boston, Massachusetts, Nov. 1-4, 1982.
98. J.A. Mazer, Methods for Investigating the Properties of Polycrystalline Silicon P-N Junction Solar Cells (Ph.D. Dissertation, University of Florida, 1981), p. 53.
99. L.L. Kazmerski and P.J. Ireland, Solar Energy Research Institute, Private Communication (1981).
100. T.J. Magee, C. Leung, H. Kawayoshi, B. Furman, C.A.A. Evans, Jr. and D.S. Day, Appl. Phys. Lett. 39, 260 (1981).
101. S.N. Chakravarti, P.L. Garliarino and K. Murty, Appl. Phys. Lett. 40, 581 (1982).
102. R.W. Balluffi, in Interfacial Segregation, edited D.L. Davidson, J. Appl. Phys. 53, R81 (1982).
103. J.C. Mickelsen, Jr., Appl. Phys. Lett. 40, 336 (1982).
104. L.L. Kazmerski, P.J. Ireland and T.F. Ciszek, Appl. Phys. Lett. 36, 323 (1980).
105. L.L. Kazmerski, P.J. Ireland and T.F. Ciszek, J. Vac. Sci. Technol. 17, 34 (1980).
106. L.L. Kazmerski, J. Vac. Sci. Technol. 20, 423 (1982).

107. SEMIX is a trade mark for polycrystalline silicon manufactured by SEMIX, Inc., Rockville, Md.
108. Walter Bollmann, Private communication (1980).
109. D.C. Joy, D.E. Newbury and D.L. Davidson, J. Appl. Phys. 53, R81 (1982).

APPENDIX I

TERMS AND DEFINITIONS USED IN EBIC SOFTWARE SYSTEM

EBIC: A Flextran program to provide automated EBIC linescan data collection, plotting, and interpretation will be available through the Tracor Northern software user's group.

FLEX: A compact command language that is used to program automatic sequential operations for the TN-2000 X-ray analyzer. By using FLEX commands the operator may create and execute FLEX strings which define complete data analysis and data reduction.

JOYSTICK: Tracor Northern hardware in the form of a 12x12x12 cm box. There are two joystick controls (1) One is used for the stage. It has a joystick control which provides simultaneous X and Y stage speed range (slow, fast, or off), and two buttons by the computer. (2) The other controls the digital beam cursor, threshold, brightness, and contrast. A joystick controls the position of two intersecting intensified lines on the CRT. The intersection point is used to define points on the

image to the computer. This control has the same white and red buttons as the stage control.

POINT TABLE:

A two dimensional array which contains the X, Y and Z stage coordinates of positions named by numbers from 0 through 25. Points are defined by the SET command, the GET command positions the stage to any specified point, and the DELETE command deletes any specified point or the entire table.

**POINTS OR DIGITAL BEAM
COORDINATE UNITS:**

These units are based on the CRT size where the size of the CRT is: 4095 by 4095 Units. Under digital beam control, the beam can be moved only in interger increments of these units.

STANDARD TABLE:

The same as the point table except that the position names are specified by a one to four character mneumonic instead of a number.

STEP SIZE:

The number of Digital Beam Coordinate Units that the beam shifts between data points.

TASK:

An electron microprobe automation program, written in Flextran, which provides a set of user oriented commands for instrument control. The commands are broken into five groups: general purpose, wavelength dispersive control, energy dispersive control, correction and external program linkage, and schedule execution. It is possible to control the filament on or off, beam blanking, beam current and position, stage position, spectrometer positions and crystal selections, detector voltages, pulse height analyzer windows, and the camera system. When used in conjunction with a schedule, TASK can perform simultaneous quantitative data collection, reduction and statistical evaluation. Definition of TASK (1) Taken from Sandia-TASK '78: An Electron Microprobe Automation Program, William F. Chambers, October 1978.

APPENDIX II
EBIC COMMANDS

A detailed description of the commands available in EBIC follows. The function, form, and an example are given. The portion of the command that is not necessary is included in parentheses. In the examples, portions underlined indicate human input and a † indicates a carriage return. Notes are enclosed within parentheses and are written in small characters.

BLANK

Function: Activates a solenoid which causes the movable Faraday cup to intercept the beam. The cup is located just below the beam regulation aperture so that the beam regulation is not altered as a result of blanking the beam in this manner. This command is automatically executed during stage motion and all standby periods to avoid unnecessary beam damage to the sample. No argument is used.

Form: B(LANK)

Example: EBIC: BLANK †

EBIC: (beam is now blanked)

CALIBRATE

Function: This provides a means to calibrate the

TN-1310 Imaging Module (or Digital Beam Control) to the specific SEM being used. The program moves the beam in a box pattern (). The X and Y gain and position controls on the digital beam control unit are adjusted to make the box co-inside with the edges of the CRT. This calibrates the digital beam coordinate system. No arguments are used.

Form: C(ALIBRATE)

Example: EBIC: CAL ↓ (observe box and adjust X and Y controls and hit SPACE BAR)

EBIC:

CLOCK

Function: Loads and executes a clock setup program. Sets the year, month, day, hour, a.m. or p.m., and minutes. Once set, the clock will keep the data and time as long as the computer is not boot-strapped. This is not a program that Tracor Northern provides. It was written by Joe Doyle of Rockwell.

Form: CL(OCK)

Example: EBIC: CLOCK ↓
 Year? 82 ↓ , Month? 1 ↓ , Day? 21 ↓ , Hour?
2 ↓ , AM(=1) or PM(=2)? 2 ↓ , Minute?

16 † , 1/21/82 2:16 pm

EBIC:

CUP

Function: Positions the movable Faraday cup into the beam's path, lists the required control settings on the TN-1244 Beam Current Monitor, and halts. When ready, the program zeros and then starts a scaler which is counting the current output of the Faraday cup. The prior beam current, new beam current and the percent change is displayed. No argument is used.

Form: CU(P)

Example: EBIC: CUP †

SET BCM: (1-MODE=VOLTAGE) (2-RANGE = .1-
IV) (3-MDTR = 2)
HIT SPACE WHEN READY [SP] 1/21/82 2:16 PM
PRIOR = 12.669 NEW= 12.646 NANOAMPS CHANGE
= -0.181%

DEFINE

Function: Allows the operator to adjust the stage axis scalers to the mechanical value as read on the stage. Also used to set one of

64 settings which regulate the beam current between 1.9 to 105nA. The beam current regulator will be set to the closest possible value which is greater than or equal to the value requested. Beam regulation is specific to the Cameca MBX.

Forms: D(EFINE) A(XIS)
D(EFINE) B(EAM) value

Examples: (1) EBIC: DEF AXIS +
X = 5 ? 10 + (10 is the current
reading from the three
Y = 5 ? 10 + stage mechanical
Z = 5 ? 10 + scales.)

EBIC:

(2) EBIC: DEF BEAM 20 +

EBIC: (Beam current will now be set
to the next setting > 20 nA.)

DELETE

Function: Used to delete either individual entries of or the entire point of standard table. The "Point Table" is a two dimensional array which contains the X, Y, and Z stage coordinates of points named by numbers from 1 through 25. The "Standard Table" is the same as the "Point Table" except the points are named by a one to four character

mnemonic, such as 'GAAS'. (See GET and SET commands also.)

Forms: DEL(ETE) type name where type references either P(OINT) or S(TANDARD) and name defines the point number, standard name, or TAB to delete the entire table.

Example: (1) EBIC:DEL POINT 8 + (point 8 is deleted)

EBIC:

(2) EBIC:DEL ST CU + (point Cu is deleted)

EBIC:

(3) EBIC:DEL POINT TAB + (entire point table is deleted)

EBIC:

EBIC

Function: Sets up parameters, collects data from line scan, stores data on disk, and plots linescan data on plotter if desired.

First there are three choices of how the data is to be manipulated. 1 - plot the data after line data is obtained, 2 - plot data that is stored on disk, and 3 - store the data on disk and then plot the data. In all cases, the data is displayed

on the CRT prior to hard plotting. This allows the data to be observed or scrapped and remeasured without waiting for a hard plot. Each of the three cases will now be treated individually. Plot scales are \ln (EBIC current) versus microns or EBIC (nA) versus microns.

i-Plot Data

For this case, the live data will simply be plotted without it being stored on disk. The linescan parameters stepsize and magnification as previously set are displayed. The STEP SIZE in microns is the distance between data points. This is also given in digital beam coordinate units as POINTS with microns between coordinate points given. The working magnification is given as MAG. One then has the option of changing any of these parameters or simply leaving them as they are. For example, the parameters may be as follows:

```
STEP SIZE = 10.000 UM = 10 POINTS (1
UM/POINT)
```

```
MAG = 1.00 KX
```

```
OK?
```

If no is the answer to OK, the magnification in KX is asked and a number of coordinate points between data points can be input. The number of coordinate points between data points is used since the beam can only be moved in interger increments of coordinate points. The distance between coordinate points is calculated from the given magnification and displayed so that the micron distance between data points can be easily figured. If a return is the answer to a question, that particular parameter is not changed.

Example: MAG (KX) = ? + (Mag stays at 1000X)
 SCALE FACTOR = 0.017908 UM/POINT
 # POINTS/STEP = 10 +

The next question is "NEW LINE?". If no is answered, the previous coordinates of the starting and ending points of the linescan will be used. If yes, the starting and ending points of the line scan can be defined using the cursor controlled by a joystick. The coordinates of each point are set and displayed when the white button on the joystick is pressed. Once

set, the space bar is pressed to begin the linescan. The data will appear on the CRT with one data point per channel as the linescan is in progress. Once the linescan has finished, the program asks if the linescan should be hard plotted or not. If no is answered, the "EBIC" prompt is returned. If yes is answered, a plot label is requested and will be typed across the top of the plot; it can be up to 25 characters. The pen numbers desired for the axes and the plot is then entered. The program then asks if a Least Square Fit is desired. If yes, the X coordinate values of two points, between which the slope or inverse slope is desired, is entered. For "X-VALUE PT #1" enter the micron value of one point and the same for PT #2. The slope of the fitted curve between the 2 given points is displayed. The effective diffusion length, L_{eff} , which is simply the inverse of the slope is calculated and displayed. One then has the option of printing either the slope or the diffusion length or neither on the plot. The pen is manually positioned to the desired

location. The end points of the slope are measured and are also plotted by circles. This slope measurement can be repeated as many times as desired by answering Y to "ANOTHER?".

Labels can be printed in any color and in any location on the plot by answering Y to "PLOT LABELS?". The label (up to 25 characters) and pen number are entered, the pen positioned to the desired location and then ENTER is pressed on the HP plotter to print the label.

There are three options at this point. (1) If a new plot is desired, enter RET. (2) If one wants to return to the EBIC prompt, enter 2. (3) If one wants a plot to be made on the same axis at the same scale enter 1. The previous procedure for "PLOT DATA" is just repeated only using new data. If the new data is to be plotted on the previous axis and it goes off scale it will state that the data is off scale and returns to the three choices of new plot, EBIC, or plot on same axis. The data can then be retaken with an adjustment made to the hardware to allow the data to fall

within scale. An alternative is to plot the data with the largest scale first.

2-Data From Disk

The program first asks "DATA FILE # TO BE PLOTTED = ?". The desired file # is entered. The data from that file is brought into memory and displayed on the CRT. The remainder of the procedure is identical to the Plot Data case.

3-Store Then Plot

This option begins in the same manner as option number 1 (PLOT DATA). After answering Y to the "PLOT?" question, the program asks what file number the data should be stored under on the disk in drive 1. If the file # designated is already used, the program says "FILE # XXX IS USED OK?." If Y is entered, file XXX is replaced. If N is the reply another file # is asked for. A file label can then be entered (up to 20 characters) and the data is transferred to disk with the label. The remainder of the procedure is the same as option 1.

Form: E(BIC)

Example: EBIC: EBIC †

1 = (PLOT DATA) 2 = (DATA FROM DISK) RET =
(STORE THEN PLOT) ETC.

GET

Function: Recalls the coordinates of previously set stage positions in either the Point or Standard tables and positions the stage to those coordinates. (See SET and DELETE commands also.)

Form: G(ET) type name

where type = P(OINT) or S(ID) depending on which stored position is desired.

name = a number from 1 through 25 POINT type or a four character mnemonic for STD type.

Example: 1) EBIC:GET POINT 10 † (coordinates of point #10 are positioned)

EBIC:

2) EBIC:GET STD CDTE † (coordinates of point CDTE are positioned)

LABEL

Function: Causes the program to jump to the plot labeling routine so that an entered label

(up to 25 characters) can be entered through the keyboard and printed by the HP plotter.

Form: L(ABEL)

Example: EBIC: LABEL †
 LABEL IS SAMPLE # 1234 †
 PEN #? 3 †

(manually move pen to desired location for the label and then hit the enter button on the HP plotter to initiate the label to be printed)

POSITION PEN

ANOTHER? NO † (yes answered to ANOTHER allows another label to be printed.)

EBIC:

LIST

Function: Allows either the point table or the standard table to be listed.

Form: L(IST) type
 where type = P(OINT) or S(TD)

Example: 1) EBIC: LIST POINT †

POINTS LIST	X	Y	Z
1	000	000	000

2) EBIC: LIST STD †

STD	X	Y	Z
B	000	000	000
CDTE	000	000	000

etc.

EBIC:

LOAD

Function: Brings previously stored values of the stage position coordinates (point or Standard Table) from the specified disk into memory. The file number desired is specified.

Form: LO(AD) type file #
 where type = P(OINT) or S(TD)

Example: EBIC: LOAD POINT 999 †
 OP#? 1 †
 EBIC:

MANUAL

Function: Allows manual control of stage stepping motors via Cameca standard controls. The stage can always be moved via the joystick when the computer is not busy.

POSITION

Function: Positions the stage to specified

coordinates or moves the stage by specified number of units.

Form: P(OSITION) axis mode value
 where axis = X,Y, or Z axis
 mode = TO or BY. TO means move specified stage axis to the given value and BY means move the specified stage axis by + or - the given value.
 value = the absolute stage position or the + delta the axis is to be moved by (in millimeters)

Example: EBIC: Position X TO 35.3, Y BY -10, Z TO 0.1 +
 EBIC: (note that one, two or all three axes can be positioned simultaneously.)

SET

Function: To store present stage coordinates as a point number in the points table or as a standard in the standards table by pressing either the white or red button on the joystick. The white button causes a backlash correction for the first time and stores the point the second time. If after backlash correction one needs to fine adjust, the red button will reset for

another backlash correction. The red button pressed first stores the coordinates as they set. (See DEL and GET commands also).

SHIFT

Function: Corrects for image shift between a slow and fast CRT scan. This is done by positioning the cursor on a point on an image first for a fast scan. When set, the white button on the scanning joystick is pressed. This is repeated for a slow scan. The CRT coordinates for each point is printed and the X and Y shift between the two is displayed.

Form: SH(IFT)

Example: EBIC: SHIFT ↓

CALIBRATE CURSOR

(fast scan, align cursor, hit JS#1)

X = 000 Y = 000

(slow scan, realign, hit JS#)

X = 000 Y = 000

X SHIFT = 000 Y SHIFT = 000

EBIC:

SAVE

Function: Causes one of the choice of three items to be stored on disk; point table, standard table, or EBIC itself.

Form: EBIC: SA(VE) type file #
 where type = P(OINT), S(TD), or E(BIC)
 file # = file # to store Point or STD table under. No file # is specified for EBIC.

Example: EBIC: SAVE Point 999 †
 or SAVE STD 999 †
 or SAVE EBIC †

EBIC:

TIME

Function: Prints the date and time onto the monitor. If CLOCK has not been run since the last system boot, it will print 1/0/0 12:00 AM.

Form: T(IME)

UNBLANK

Function: Simply removes the movable Faraday cup from the beam's path.

Form: U(NBLANK)

APPENDIX III
FUNCTIONS OF PROGRAM BLOCKS (EBIC)

Block #	Function	Call Block
98	Initializes and allocations variable memory space. Accepts and interprets command string. A Flex (>) or Flextran (# and *) command is overlaid into line 98,90. An EBIC command is overlaid into line 98,99 and then matched with a command in block 99. Also gives an error message (??) if a command is not recognized.	
99	Contains the list of valid commands to which block 98 makes matches to.	98
100	Called by the "INIT" command. List the current values of all the line scan and measuring parameters: step size, microns per pixel, magnification current amplifier range, time beam remains at each data point, and null offset. Any of these parameters may be changed during the INIT command.	99,6

105	Positions beam at coordinates X=0 & Y=4095 or X=0 & Y=0 as initializations in defining linescan and in calibrating the digital beam amplifier (TN-1310)	115,20 130,10
109	Sets the space bar address on the TN 4000 and the TTY to zero. Initializes hold in block 110 until space bar is pushed.	110,10 130,10
110	Starts an infinite loop until the space bar is pushed. Provides a hold until equipment is adjusted properly.	190,5
115	Allows the operator to define a start and end point of a desired linescan (steps only in the X direction) by positioning the cursor and pressing the white button on the joystick at the two desired positions. These coordinates can be used successively until a new line is defined.	190,5

- 125 Loads libraries, allocates variables, 98
and turns on the first half of memory
display.
- 130 Sets up the box raster on the CRT to 99,1
allow adjustments of the X & Y gain
and X & Y position controls on the
digital beam 1310.
- 135 Runs the beam through a box and cross 130,10
pattern each time it runs. Block 130
runs block 135 until the space bar is
pushed.
- 140 Measures any shift in the CRT image 99,9
between a slow and a fast raster.
The shift is used to position the
beam accurately for the linescan.
- 145 This block performs the linescan and 190,10
the acquisition of the EBIC current.
The beam is positioned by the pre-
calculated step size from the INIT
command and the current is measured
at each data point and displayed in
the first half memory instantaneously.

The beam remains at a point for the "time-per-point" specified during the last INIT command. The beam is stepped two step-size units before the start point and continues to the end point. The first two data points will not be counted to allow for system stabilizers.

150	Selection is made as to how the data is to be acquired, either live or from a stored file on disk and then what will be done with the data, either plotted or stored as a file on disk and then plotted or just plotted without storing.	39,5 115,30 185,10
155	Stores the data in array YL under a given file # and name. YL(0) is the value of the step size in microns and YL(1) is the number of data points. YL(2) is the first real datum. All data is stored in units of Amps.	165,1
160	Retrieves data from a specified file number from disk.	150,20
165	Initially the choice of no plot, linear plot or log plot is made. The plot scales are	190,20

calculated from the data and the axes are drawn with a specified pen number. The appropriate axes labels are selected, a plot label can be typed in and printed at the top of the paper, and the current date is printed.

- | | | |
|-----|--|-----|
| 170 | Checks for data that may be off the current axes range and the plots data connecting each point with a continuous line using a specified pen number. | 165 |
| 175 | Performs a least square fit between the two given points X value and displays the slope and inverse slope of the corrected line between the two points. One then has the option of plotting the end points of the corrected line or not and printing either of the slopes on the plot. | 170 |
| 180 | Routine for printing any label anywhere on the plot with any desired pen number. | 175 |
| 185 | Provides the option of either plotting another set of data on the same axes or not. 185,40 returns and positions the | 180 |

pen holder to the upper right.

190	Lets one define a new linescan or use the previous line. Lists beam current monitor settings. Checks for any data <0; if such data is plotted, $2n (data)$ is plotted.	185
229	Reads the time and date for plotting.	99,11 165,120

APPENDIX IV
MIS DEVICE FABRICATION DETAILS

1. Clean and polish wafer (see Appendix V)
2. Heat treat (if desired);
 - A. Heat in annealing furnace,
 - B. Strip of oxide in 10% HF.
3. Grow oxide:
 - A. Beaker oxide - boil in deionized water for 20 minutes,
or
 - B. Dry oxide - heat in annealing furnace at 200°C for 10 minutes.
4. Etch back oxide off using cotton swab dipped in HF.
5. Evaporate back contact. (Al)
6. Evaporate front contact (Al)

APPENDIX V

STANDARD WAFER CLEANING AND POLISHING PROCEDURES

Standard Wafer Cleaning Procedure

1. Scrub with cotton swab soaked with trichloroethylene (TCE).
2. Boil in TCE for 5 minutes.
3. Boil in fresh TCE for 5 minutes.
4. Boil in acetone for 5 minutes.
5. Boil in methanol for 5 minutes.
6. Rinse in deionized water ($\rho \geq 10 \text{ M}\Omega\text{-cm}$) for 5 minutes.
7. Dip in 1 H_2SO_4 : 1 H_2O_2 solution, v/v, for 10 minutes.
8. Remove oxide by dipping in 1 HF : 9 H_2O solution, v/v, for 10 seconds.
9. Rinse in deionized water for 5 minutes.
10. Blow dry with N_2 gas gun.

Standard Wafer Polishing Procedure

1. Clean and degrease by following steps 1-6 above.
2. Swirl wafers in a solution of 2 HF : 15 HNO_3 : 5 CH_3COOH , v/v for 10 minutes.
3. Rinse in deionized water for 5 minutes.
4. Blow dry with N_2 gas gun.

BIOGRAPHICAL SKETCH

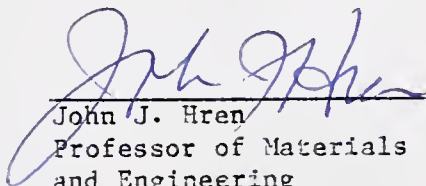
Phillip Eugene Russell was born in Winston-Salem, North Carolina, on January 15, 1955. He received the B.S. degree in physics/education from Appalachian State University, Boone, North Carolina, in 1975 and the M.S. degree in physics from West Virginia University, Morgantown, West Virginia, in 1977. Since 1978 he has been working toward the Ph.D. degree in materials science and engineering at the University of Florida, Gainesville, Florida. Since September, 1980, he has been employed by the Solar Energy Research Institute, Golden, Colorado.

I certify that I have read this study and that in my opinion it conforms to acceptable standards of scholarly presentation and is fully adequate, in scope and quality, as a dissertation for the degree of Doctor of Philosophy.



Paul H. Holloway, Chairman
Professor of Materials Science
and Engineering

I certify that I have read this study and that in my opinion it conforms to acceptable standards of scholarly presentation and is fully adequate, in scope and quality, as a dissertation for the degree of Doctor of Philosophy.



John J. Hren
Professor of Materials Science
and Engineering

I certify that I have read this study and that in my opinion it conforms to acceptable standards of scholarly presentation and is fully adequate, in scope and quality, as a dissertation for the degree of Doctor of Philosophy.



Rolf Hummel
Professor of Materials Science
and Engineering.

I certify that I have read this study and that in my opinion it conforms to acceptable standards of scholarly presentation and is fully adequate, in scope and quality, as a dissertation for the degree of Doctor of Philosophy.

Frederik A. Lindholm

Frederik A. Lindholm
Professor of Electrical Engineering

This dissertation was submitted to the Graduate Faculty of the College of Engineering and to the Graduate Council, and was accepted as partial fulfillment of the requirements for the degree of Doctor of Philosophy.

December 1982.

Hubert A. Bavis

Hubert A. Bavis
Dean, College of Engineering

Dean for Graduate Studies
and Research

